UNIVERSITA' DEGLI STUDI DELLA CALABRIA
Facoltà di Scienze Matematiche Fisiche e Naturali

Dottorato di ricerca in Fisica - XX ciclo
Settore scientifico-disciplinare Fis/04

Intensive irradiation studies, monitoring and commissioning data analysis on the ATLAS MDT chambers

Tesi di
Daniela Salvatore

Supervisore
Prof. Giancarlo Susinno

Coordinatore
Prof. Giovanni Falcone

Contents

Introduction

The **Large Hadron Collider** (LHC) is the proton-proton collider that will operate at a center of mass energy of 14 TeV and at a maximum luminosity of L=10^{34}cm^{-2}s^{-1}. The LHC will reproduce interactions similar to the ones which existed when the universe was only $\sim 10^{-12}$s old, conditions which have never been achieved in any previous collider. The primary goal of the LHC project is the discovery of the Higgs boson, the particle of a "mysterious" field responsible for giving different masses to different particles. The Standard Model foresees such a particle, but it has never been observed yet.

The **ATLAS** (A Toroidal LHC ApparatuS) experiment has been designed to maximize the discovery potential for New Physics such as Higgs bosons and supersymmetric particles, while keeping the capability of high precision measurements of known objects such as heavy quarks and gauge bosons.

High-momentum final-state muons are amongst the most promising and robust signatures of physics at the LHC. To exploit this potential, the ATLAS Collaboration has designed a high-resolution muon spectrometer with stand-alone triggering and momentum measurement capability over a wide range of transverse momentum, pseudorapidity and azimuthal angle. The **Monitored Drift Tube Chambers** (MDT) represent the precision tracking detector for such a spectrometer, both in the barrel region and in the end-cap.

During my PhD I have been part of the ATLAS Collaboration within the Cosenza group. I was strongly involved in different activities concerning the MDTs, as I report in this thesis.

- In **Chapter 1** I give a description of the Standard Model and the spontaneous symmetry breaking mechanism, where the Higgs boson plays a fundamental role. Some decay channels are also described, together with an introduction to supersimmetry.

- **Chapter 2** focuses on the LHC project and, in particular, the ATLAS experiment. A description of the various subdetectors is given, with special attention to the Monitored Drift Tube chambers of the muon spectrometer.
- **Chapter 3** describes the high rate and high background tests carried out on a small ATLAS-like MDT chamber, by the Cosenza and Roma TRE groups. The precision tracking chambers of the muon spectrometer, in fact, have to operate for more than 10 years in the harsh LHC background, due mainly to low energy neutrons and photons. Aging effects, such as the deterioration of the tube themselves can appear and difficulties in pattern recognition and tracking may occur. Moreover an upgrade to Super-LHC is foreseen.

  I gave my personal contribute by monitoring the drift parameters and the tracking performances of the test MDT chamber, both in the photon irradiation test and in the neutron one. This work has already been published and presented to the international community.
- In **Chapter 4** I give an accurate description of the **MDTGnam** package, the software I co-developed for the on-line monitoring of MDT performances. When dealing with a complex apparatus, such as the ATLAS experiment, an on-line monitoring system is a fundamental tool. The GNAM project, developed by Cosenza, Pavia, Pisa and Napoli groups, is a monitoring framework to be used by all the ATLAS detectors. My work consisted in writing the GNAM C++ code for the MDT detector specific part. Designing and implementing the MDTGnam package has been my most important task during my PhD, since it is the official ATLAS software for the ongoing MDT commissioning.
- Last chapter, **Chapter 5**, is devoted to the analysis of the commissioning data from barrel sector 13. Sector 13 was used as a pilot system to test different detector data taking in their final conditions. Up to November 2006, 13 MDT chambers were installed and their performance monitored both by means of usual noise tests and by cosmic rays penetrating the ATLAS cavern. In addition, the barrel toroid was switched on for the first time at the nominal current. Results from the magnet test are also reported.

Chapter 1

The Standard Model and the LHC

About one century ago, the first elementary particle, the electron, was discovered. Since then, physics of fundamental interactions has been constantly evolving. The so called Standard Model proved to be efficient first of all in organizing elementary particles in a consistent schema, and then in unifying the description of three of the four fundamental interactions in nature. Furthermore, the Standard Model successfully predicted the existence of the gauge bosons W and Z.

However, the Standard Model has a weak point: it requires the existence of a further scalar particle, the Higgs boson, which has not been observed yet. This particle plays a fundamental role: its presence would determine the mass of all the other particles, through the so-called spontaneous symmetry breaking mechanism. Currently the Large Hadron Collider (LHC) is being assembled at CERN, and a new research program has been established to search for the Higgs boson. If it can be observed, than the correctness of electro-weak unification, by Glashow, Weinberg and Salam, will be confirmed. Otherwise, totally new theoretical concepts will be needed.

In this chapter, after a brief summary of the Standard Model and of the mechanism through which elementary particles acquire their mass, present experimental and theoretical limits on the Higgs boson mass will be illustrated. Later, the most important decay channels in the LHC context, together with the expected background, will be discussed.

1.1 The Standard Model

1.1.1 Consequences of gauge invariance

The Standard Model is presently acknowledged as the most appropriate theory to describe the fundamental components of matter and its mutual interactions. The model is based on the requirement of gauge invariance under the symmetry group $U(1)_Y \otimes SU(2)_L$, concerning the electromagnetic and weak interactions; in the strong interaction sector, the required invariance is $SU(3)_C$. $U(1)_Y$ is the symmetry group whose generator is the weak hyper-charge operator, while $SU(2)_L$ and $SU(3)_C$ are, respectively, the weak isospin and color symmetry groups.

Fundamental fermions are classified through the color charge, relative to the strong interaction symmetry group: particles carrying a non void color charge are called *quarks*, while the other ones are called *leptons*.

A further classification for fermions is based on chirality. The leptonic sector includes three isospin doublets with chirality -1 (indicated with L, from *Left*) and three isospin singlets (indicated with R, from *Right*): the asymmetry between right and left chirality is due to the fact that right neutrinos have never been observed. Similarly, quarks are divided into three left doublets and six right isospin singlets. Table 1.1 shows the classification of the fermions and the associated quantum numbers. In the Standard Model, weak interactions couple only on those states carrying a non null weak isospin.

In order to describe the lepton fields in a simple way, let's introduce a symbol α that will assume the values $\alpha = 1, 2, 3$; this index will distinguish the three lepton families. L spinor doublets and R spinor singlets will be denoted with $\psi_L^\alpha(x)$ and $\chi_R^\alpha(x)$, where x represents a point in space-time. Quantum numbers of $U(1)_Y \otimes SU(2)_L$ for leptons are shown in Tab. 1.2, where Q is the electric charge, Y the hyper-charge and T_3 the third component of the weak isospin.

The free fermion Lagrangian is required to be invariant under any local transformation of the $U(1)_Y \otimes SU(2)_L$; thus the general expression

$$\mathcal{L} = i \sum_\alpha \left[\psi_L^{\dagger\alpha}(x) \bar{\sigma}^\mu \partial_\mu \psi_L^\alpha(x) + \chi_R^{\dagger\alpha}(x) \sigma^\mu \partial_\mu \chi_R^\alpha(x) \right] \tag{1.1}$$

	$SU(2)_L$ **doublets**	$SU(2)_R$ **singlets**
Leptons	$\binom{\nu_{e_L}}{e_L}$ $\binom{\nu_{\mu_L}}{\mu_L}$ $\binom{\nu_{\tau_L}}{\tau_L}$ $T = \frac{1}{2}$ $Y = -1$	$e_R\, \mu_R\, \tau_R$ $T = 0$ $Y = -2$
Quarks	$\binom{u_L}{d_L}$ $\binom{c_L}{s_L}$ $\binom{t_L}{b_L}$ $T = \frac{1}{2}$ $Y = \frac{1}{3}$	$u_R\, d_R\, c_R\, s_R\, t_R\, b_R$ $T = 0$ $Y(u_R, c_R, t_r) = \frac{4}{3}$ $Y(d_R, s_R, b_r) = -\frac{2}{3}$

Table 1.1: Isospin doublets and singlets for leptons and quarks. Weak isospin and hypercharge quantum number are quoted too.

	$SU(2)_L$	Y	$Q = Y/2 + T_3$
$\psi_L^\alpha(x) = \binom{\nu_L^\alpha(x)}{\chi_L^\alpha(x)}$	2	-1	$\binom{0}{-1}$
$\chi_R^\alpha(x)$	1	-2	-1

Table 1.2: Lepton quantum numbers.

assumes the following form [1]:

$$\begin{aligned} \mathcal{L} = & -\frac{1}{4} B_{\mu\nu}(x) B^{\mu\nu}(x) - \frac{1}{4} F^a_{\mu\nu}(x) F^{a\mu\nu}(x) \\ & + i \sum_\alpha \left[\psi_L^{\dagger\alpha}(x) \bar{\sigma}^\mu D_\mu \psi_L^\alpha(x) + \chi_R^{\dagger\alpha}(x) \sigma^\mu D_\mu \chi_R^\alpha(x) \right] \end{aligned} \tag{1.2}$$

where

$$B_{\mu\nu}(x) = \partial_\mu B_\nu(x) - \partial_\nu B_\mu(x) \tag{1.3}$$

$$F^a_{\mu\nu}(x) = \partial_\mu W^a_\nu(x) - \partial_\nu W^a_\mu(x) - g\epsilon^{abc} W^b_\mu(x) W^c_\nu(x) \tag{1.4}$$

$$D_\mu \psi_L^\alpha(x) = \left[\partial_\mu + \frac{i}{2} g W^a_\mu(x) \sigma^a - \frac{i}{2} g' B_\mu(x) \right] \psi_L^\alpha(x) \tag{1.5}$$

$$D_\mu \chi_R^\alpha(x) = \left[\partial_\mu - i g' B_\mu(x) \right] \chi_R^\alpha(x). \tag{1.6}$$

B_μ is the gauge field introduced for the symmetry under $U(1)_Y$ and the three fields $W^a_\mu(x)$, $a = 1, 2, 3$, are required for the invariance under $SU(2)_L$ (one field for each generator of this gauge group). σ^a operators are a base of the $SU(2)_L$ algebra (Pauli matrices), g and g' are the coupling constants of gauge fields to the leptons. The hyper-charge of gauge bosons is 0. The terms $B_{\mu\nu}(x)B^{\mu\nu}(x)$ and $W^a_{\mu\nu}(x)W^{a\mu\nu}(x)$ simply describe the free evolution of the gauge fields.

Up to now, the theory includes four massless gauge bosons, one with electric charge[1] +1 (W^1), two with charge 0 (B and W^0) and one with charge -1 (W^{-1}) . Possible mass terms for the fermions in the Lagrangian (1.2) would take the form $\chi_L^{\dagger a}\chi_R^a + \chi_R^{\dagger a}\chi_L^a$, so they would not be invariant under the symmetry group because the terms χ_L and χ_R carry different isospin and hyper-charge quantum numbers. Potential mass terms for the W^a_μ or for the B_μ would violate gauge invariance too. Therefore all the particles (leptons and bosons) in the Lagrangian (1.2) are massless, and this is in sharp contrast with the experimental evidence.

1.1.2 Higgs mechanism and spontaneous symmetry breaking

The proposed mechanism, in order to let leptons and intermediate bosons acquire mass, requires the introduction of a new doublet of complex scalar fields

$$\varphi = \begin{pmatrix} \varphi_+ \\ \varphi_0 \end{pmatrix} \tag{1.7}$$

whose quantum numbers are shown in Tab. 1.3.

	$SU(2)_L$	Y	$Q = Y/2 + T_3$
$\varphi(x) = \binom{\varphi_+(x)}{\varphi_0(x)}$	2	+1	$\binom{1}{0}$

Table 1.3: Higgs doublet quantum numbers.

Introducing the most general gauge invariant and renormalizable coupling of the the Higgs doublet to the leptons, the following Lagrangian terms are obtained:

$$\begin{aligned} \mathcal{L}_H = {} & D_\mu\varphi^\dagger(x)D^\mu\varphi(x) - V\left(\varphi^\dagger(x)\varphi(x)\right) \\ & - \sum_\alpha \lambda_\alpha \left[\psi_L^{\dagger\alpha}(x)\varphi(x)\chi_R^\alpha(x) + \chi_L^{\dagger\alpha}(x)\varphi(x)\psi_R^\alpha(x)\right] \end{aligned} \tag{1.8}$$

where

$$D_\mu\varphi(x) = \left[\partial_\mu + \frac{i}{2}gW^a_\mu(x)\sigma^a + \frac{i}{2}g'B_\mu(x)\right]\varphi(x) \tag{1.9}$$

and

$$V(\varphi^\dagger\varphi) = \mu^2\varphi^\dagger\varphi - \lambda(\varphi^\dagger\varphi)^2 \tag{1.10}$$

Figure 1.1 shows a section of the potential V, for the two cases $\mu^2 > 0$ and $\mu^2 < 0$.

---

[1] Electric charge, hyper-charge and the third component of the weak isospin are not independent: $Q = T_3 + \frac{Y}{2}$

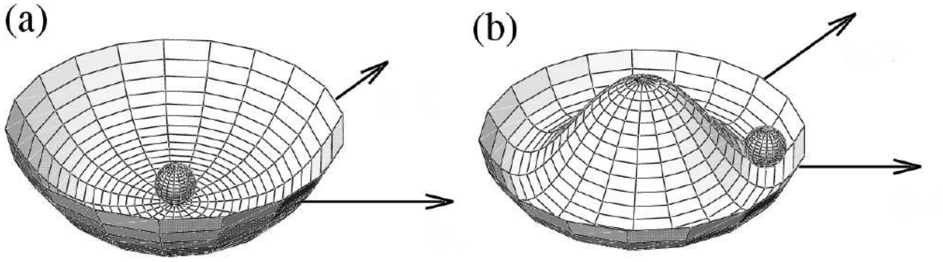

Figure 1.1: Graph of the potential $V(\varphi^\dagger\varphi)$ for $\mu^2 > 0$ and $\mu^2 < 0$.

If $\mu^2 < 0$, the potential reaches its minimum value when

$$\varphi^\dagger\varphi = -\frac{\mu^2}{2\lambda} = v^2 \tag{1.11}$$

Therefore, in this case, the vacuum expectation value is not void for at least one component of φ. We can assume:

$$\langle 0 \,|\varphi(x)|\, 0\rangle = \begin{pmatrix} 0 \\ v \end{pmatrix}. \tag{1.12}$$

One consequence is that the fundamental state is not invariant under the symmetry transformation of the Lagrangian. Such a situation is called “Spontaneous Symmetry Breaking”.

In order to determine the particle content of the model, we need to expand the potential around a minimum point. A convenient parametrization for the Higgs field is the following:

$$\varphi(x) = e^{-i\theta^a(x)\sigma^a/2}\begin{pmatrix} 0 \\ v + \frac{H(x)}{\sqrt{2}} \end{pmatrix}. \tag{1.13}$$

If we substitute (1.13) in the Lagrangian (1.8), we can exploit the gauge invariance of the action to discard the multiplicative factor. The resulting Lagrangian is the same as (1.8), just with the generic Higgs field substituted by the following expression:

$$\varphi(x) \to h(x) = \begin{pmatrix} 0 \\ v + \frac{H(x)}{\sqrt{2}} \end{pmatrix}. \tag{1.14}$$

The particle described by $H(x)$ is the physical Higgs boson. With this substitution, the complete Lagrangian is:

$$\begin{aligned}\mathcal{L} = & -\frac{1}{4}B_{\mu\nu}(x)B^{\mu\nu}(x) - \frac{1}{4}\sum_{a} F^{a}_{\mu\nu}(x)F^{a\mu\nu}(x) \\ & + i\sum_{\alpha}\left[\psi_L^{\dagger\alpha}(x)\bar{\sigma}^{\mu}D_{\mu}\psi_L^{\alpha}(x) + \chi_R^{\dagger\alpha}(x)\sigma^{\mu}D_{\mu}\chi_R^{\alpha}(x)\right] \\ & + D_{\mu}H^{\dagger}(x)D^{\mu}H(x) - V\left(\left(v + \frac{H(x)}{\sqrt{2}}\right)^2\right) \\ & - \sum_{\alpha} m_{\alpha}\left[\chi_L^{\dagger\alpha}(x)\chi_R^{\alpha}(x) + \chi_R^{\dagger\alpha}(x)\chi_L^{\alpha}(x)\right] \\ & - \sum_{\alpha}\frac{m_{\alpha}}{v\sqrt{2}}H(x)\left[\chi_L^{\dagger\alpha}(x)\chi_R^{\alpha}(x) + \chi_R^{\dagger\alpha}(x)\chi_L^{\alpha}(x)\right].\end{aligned} \tag{1.15}$$

The Lagrangian (1.15) shows immediately how the charged leptons acquire mass as a consequence of spontaneous symmetry breaking. Their mass is determined by the dimension-less coupling constant λ_{α} and to the vacuum expectation value v:

$$\lambda_{\alpha} = \frac{m_{\alpha}}{v}. \tag{1.16}$$

Similarly one obtains the coupling of the charged leptons to the physical Higgs boson, whose coupling constant is proportional to their respective masses:

$$g_{HLR} = \frac{m_{\alpha}}{v\sqrt{2}}. \tag{1.17}$$

Intermediate boson mass terms can be obtained by expanding the quadratic term $D_{\mu}H^{\dagger}(x)D^{\mu}H(x)$; the mass matrix in the base W^{+}, W^{-}, W^{0}, B is

$$\frac{M^2}{2} = \frac{v^2}{4}\begin{pmatrix} g^2 & 0 & 0 & 0 \\ 0 & g^2 & 0 & 0 \\ 0 & 0 & g^2 & -gg' \\ 0 & 0 & -gg' & g'^2 \end{pmatrix}. \tag{1.18}$$

In order to find the mass eigenstates, we have to diagonalize through a rotation of angle θ_W (Weinberg angle) in the space of W^0 and B. The Weinberg angle is defined by the relations:

$$\sin\theta_W = \frac{g'}{\sqrt{g^2 + g'^2}} \qquad \cos\theta_W = \frac{g}{\sqrt{g^2 + g'^2}}. \tag{1.19}$$

The particles that diagonalize the mass matrix are: $W^{\pm}$ with mass $M_W^2 = g^2/2 \cdot v^2$; Z with mass $M_Z^2 = (g^2 + g'^2)/2 \cdot v^2 = M_W^2/\cos^2\theta_W$; A with mass 0.

Finally, if we rewrite the Lagrangian (1.15) in terms of the new vector bosons, we can verify directly the couplings among the particles. In particular, we find that the electric coupling constant, e, and the weak one, g, between the leptonic doublets and the bosons W, are linked by the relation:

$$e = \frac{gg'}{\sqrt{g^2 + g'^2}} = g \sin\theta_W . \tag{1.20}$$

The Weinberg angle cannot be predicted by the theory. Its determination is a pure experimental task.

1.1.3 Higgs boson couplings

Higgs boson couplings, to the fermions and to the intermediate bosons, are predicted with good precision. If the Higgs is found at the LHC, an accurate study of the branching ratios[2] in the different channels will be enough to discriminate between the (Minimal, that is, with only one scalar doublet for the symmetry breaking) Standard Model and other theories.

The coupling constant for the Higgs boson to the fermionic couples is directly proportional to the mass of the fermion involved:

$$g_{ffH} = \left[\sqrt{2}G_F\right]^{1/2} m_f \tag{1.21}$$

where G_F is the Fermi constant. The Higgs decay width into fermions is [2]

$$\Gamma\left(H \to f\bar{f}\right) = N_c \frac{G_F}{4\sqrt{2}\pi} m_f^2 m_H \tag{1.22}$$

with N_c (the color factor) equal to 1 for the leptons and 3 for the quarks.

The coupling of the Higgs to the weak bosons is proportional to the square of their mass:

$$g_{VVH} = 2\left[\sqrt{2}G_F\right]^{1/2} m_V^2 . \tag{1.23}$$

The decay widths, at the first order in the expansion of the scattering matrix, are:

$$\Gamma\left(H \to ZZ\right) = \frac{G_F m_H^3}{16\sqrt{2}\pi}\sqrt{1 - x_Z}\left(1 - x_Z + \frac{3}{4}x_Z^2\right) \tag{1.24}$$

$$\Gamma\left(H \to W^+W^-\right) = \frac{G_F m_H^3}{8\sqrt{2}\pi}\sqrt{1 - x_W}\left(1 - x_W + \frac{3}{4}x_W^2\right) \tag{1.25}$$

---

[2] The Branching Ratio (BR) of an initial state $|i\rangle$ into a final state $|f\rangle$ is defined as the ratio between the decay width $|i\rangle \to |f\rangle$ and the total decay width if $|i\rangle$

$$BR(|i\rangle \to |f\rangle) = \frac{\Gamma\left(|i\rangle \to |f\rangle\right)}{\Gamma_{tot}} .$$

with $x_Z = 4m_Z^2/m_H^2$ and $x_W = 4m_W^2/m_H^2$.

The decays into gluons and photons, instead, are described by higher order terms, involving the quarks t and b and, only for the photons, the weak bosons W. Such decays have a significant fraction only at energies lower than the production threshold for the W and the t. Therefore, the corresponding widths are parameterized with an approximate formula, valid until $m_H \ll 4m_W^2, 4m_t^2$:

$$\Gamma\left(H \to gg\right) = \frac{G_F \alpha_s^2}{36\sqrt{2}\pi^3} m_H^3 \left[1 + \left(\frac{95}{4} - \frac{7N_f}{6}\right)\frac{\alpha_s}{\pi}\right] \tag{1.26}$$

$$\Gamma\left(H \to \gamma\gamma\right) = \frac{G_F \alpha^2}{128\sqrt{2}\pi^3} m_H^3 \left|\frac{4}{3}N_c e_t^2 - 7\right| \tag{1.27}$$

where $\alpha_s(q^2)$ and α are the strong and electromagnetic coupling constants, N_f is the number of lepton families, e_t is the electric charge of the top and N_c the usual color factor.

Summing up all the possible decay channels, we obtain the total width, shown in Fig. 1.2. For Higgs masses up to 140 GeV the width is quite small, $\Gamma(H) \leq 10$ MeV. When the channels involving gauge bosons are possible, the state becomes rapidly wider, reaching a width of nearly 1 GeV at the ZZ threshold.

The branching ratios for the main decay channels of the Higgs boson are shown in Fig. 1.2 too. For low Higgs masses ($m_H < 120$ GeV), the highly dominating channel is the decay into $b\bar{b}$, with BR $\simeq 100\%$. Such decay fraction gets abruptly lower near the WW mass shell (nearly 160 GeV). For the same reason, the BR into ZZ has a valley around 170 GeV. The same mechanism appears again, not as stressed as before, at the opening of the channel $t\bar{t}$, with a slight decrease of the BR into WW and ZZ.

1.2 The search for Higgs boson at LHC

One of the main reasons that led to the construction of the LHC, and in particular the ATLAS detector, is the search of the Higgs boson. If such a particle exists, it will be surely highlighted at the LHC.

The Standard Model puts some limits on the Higgs mass. The upper limit, near 1 TeV, comes from unitarity arguments applied the scattering operator of the electroweak theory [3]. Lower limits were obtained both from direct searches, held at the

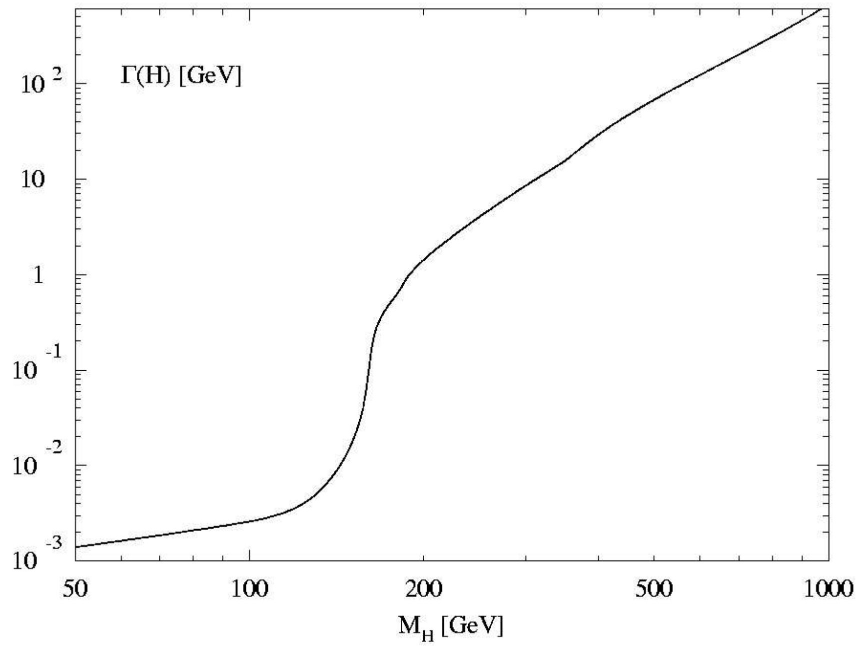

(a) decay width

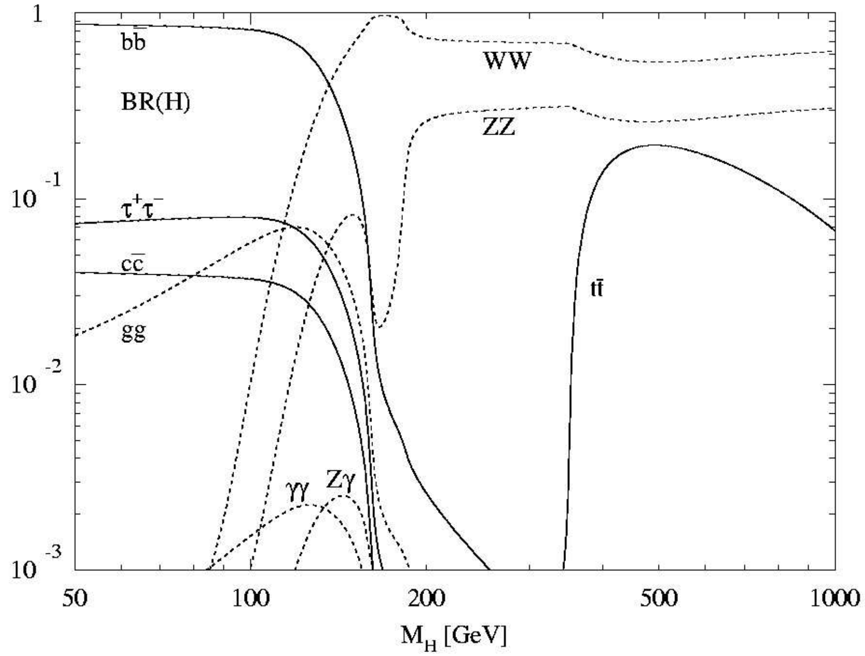

(b) branching ratios

Figure 1.2: (a): Decay width (in GeV) of the Higgs boson as a function of its mass. (b): branching ratios for the main decay channels of the Higgs boson[2].

four LEP experiments, and with a global fit of the electro-weak variables, that depend on the Higgs mass through the radiative corrections. Direct searches exclude all the values of the Higgs mass up to 114.4 GeV [4]. The electro-weak fit indicates a lower limit between 50 and 200 GeV[5]. The convergence of the electro-weak fits towards small values for the Higgs mass lead to an effort in studying the decay channels that could be used in a mass range up to 200 GeV. Nevertheless, the LHC research program is not limited to low mass Higgs, but is oriented towards the investigation of the whole theoretically achievable interval.

Figure 1.3 shows the significativity[3] of the signal for the detection of the Higgs through different decay channels. The plots are calculated for an integrated luminosity[4] of 30 and 100 fb^{-1}.

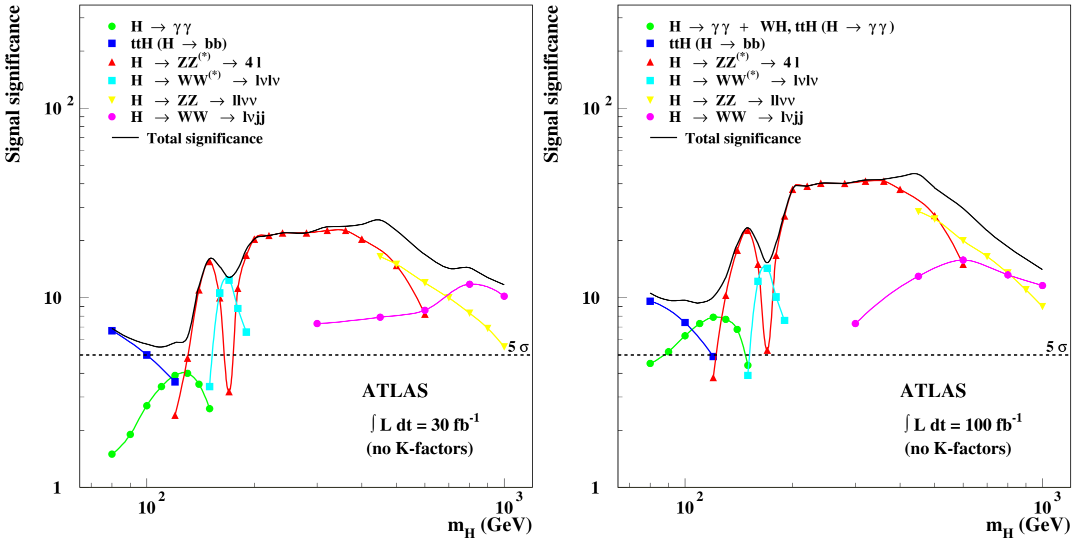

Figure 1.3: ATLAS sensitivity for the discovery of a Standard Model Higgs boson as a function of the Higgs mass, through different decay channels. [6]

The two plots reveal that 30 fb^{-1} of integrated luminosity should be enough to highlight whether the Higgs exists or no, on the whole mass range. In order to understand which are the most relevant channels, according to the mass, and thus explain the significativity curve, we will discuss briefly the production mechanisms and, later on, the Higgs decay channels.

The cross sections of the Higgs production mechanisms depend on its mass. Such

---

[3] The significativity is defined as $S = N_S/\sqrt{N_B}$, where N_S is the number of signal events and N_B the number of background events.

[4] The barn b is a non SI area unit, commonly used in particle physics to calculate cross sections. 1 b=10^{-24}cm^2.

cross sections, for proton-proton (pp) interactions with an energy of 14 GeV in the center of mass, are presented in Fig. 1.4.

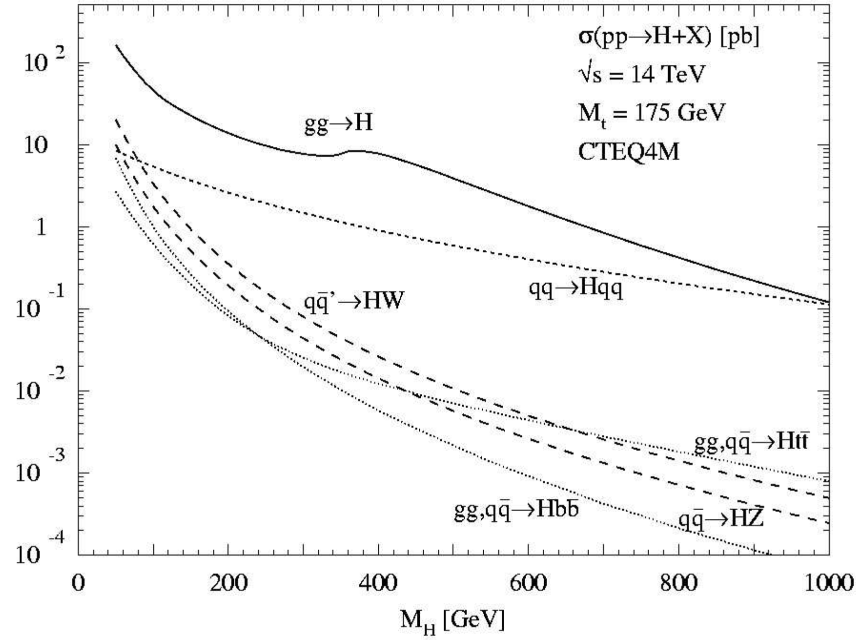

Figure 1.4: Higgs production cross section (in pb), as a function of its mass, in pp interactions with a center mass energy of 14 TeV. All the main contributes are shown. [2]

As shown in the picture, the main production mechanism, all over the mass range (100 GeV< m_H <1 TeV), is the gluon fusion $gg \rightarrow H$, with a cross section of order tens of pb for $m_H \simeq 120$ GeV. As the Higgs boson does not couple directly to the gluons, this is a second order process in the perturbative expansion (Fig. 1.5). The cross section decreases with the Higgs mass getting higher, but it has a small bump near the tt mass shell, $m_H \sim 350$ GeV.

The second production mechanism, $qq \rightarrow Hqq$, consists of boson vector fusion, as shown in Fig. 1.5. The cross section is lower over the whole mass range.

Figure 1.4 presents also the cross section for some states characterized by the presence of additional particles, produced with the Higgs, whose diagrams are shown in Fig. 1.5: such processes often offer particular cinematic characteristics that help in separating the signal from the background.

Now we will go over different Higgs decay channels, discussing the expected background as a function of m_H. As the work of the present thesis was held within the ATLAS Collaboration, the results shown here refer to this experiment. The dis-

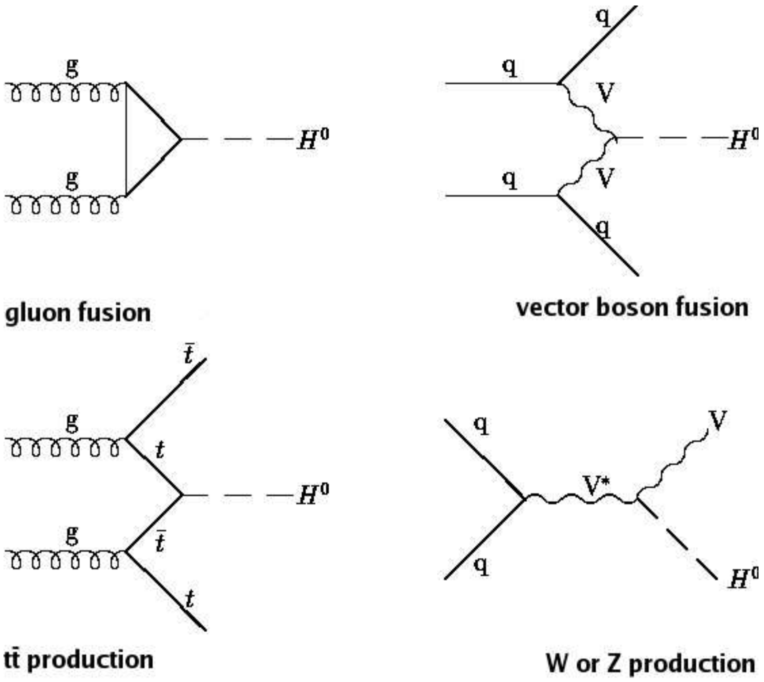

gluon fusion

vector boson fusion

tt̄ production

W or Z production

Figure 1.5: Feynman diagrams for the main Higgs production mechanism in pp collisions. V suggests a weak vector boson, W or Z.

cussed analysis are entirely reported in [6], and were conducted with a full and detailed simulation of the apparatus [7].

1.2.1 $H \rightarrow \gamma\gamma$

The decay channel $H \rightarrow \gamma\gamma$ was one of the first channel studied in ATLAS. Despite its sensitivity is not the highest, in every mass range, we will describe it in details because it has been used as a test-bed for many studies performed by the ATLAS Collaboration.

The decay of a Higgs boson into two photons is extremely rare (Fig. 1.2) because the coupling $H\gamma\gamma$ is forbidden at the first order, and so the decay is possible only through higher order diagrams (Fig. 1.6). Therefore, this channel can be observed only in a mass range, such that both the production cross section and the branching ratio are relevant: this condition is verified for 100 GeV<m$_H$<150 GeV.

The final state consists of two photons with high transverse momentum (~50 GeV) and with an invariant mass that is compatible with the Higgs mass. Despite such a simple signature, this channel is affected by two important background sources. First, the production of $\gamma\gamma$ couples through the diagrams shown in Fig. 1.6. This

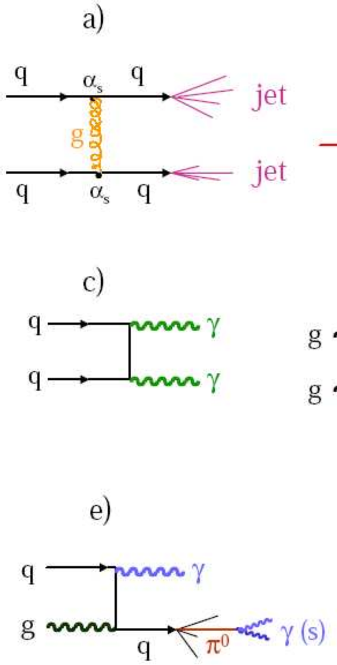

Figure 1.6: Feynman diagrams for various processes: a) production of two QCD jets; b) Higgs decay onto two photons; c) and d) production of a couple $\gamma\gamma$ with tree and box order diagrams; e) production of a couple γq with following fragmentation into a hard isolated π^0.

background is irreducible (it produces exactly the same final state as the signal); it does not have any resonant structure and decreases slowly with the two photon invariant mass. Its cross section is nearly 60 times the one of the process $H \to \gamma\gamma$ in the region of $m_{\gamma\gamma}$ around 100 GeV. Therefore the detector needs an excellent angular and energy resolution in order to permit the recognition of the narrow resonant peak over the dominating continuum background.

The second background source is the production of γj and jj, with one or both the jets mistaken as photons. Normally a jet consists of many particles, so it can be easily distinguished from a photon, for example by the presence of tracks in the inner detector, associated to the shower in the calorimeter, or by the width of the shower. Nevertheless, in some rare cases a jet can mime a single photon, as illustrated in Fig. 1.6. This happens when a quark hadronizes into a very energetic π^0, with the other particles having too little momenta to be detected. The two photons, produced in the subsequent π^0 decay, are spatially very near because of the high π^0 momentum. The probability of a jet producing such a final state is quite low, but the production cross section for γj and jj is nearly 10^6 times higher than the $\gamma\gamma$ continuum. This means that a rejection factor of at least 1000 is required in order to reduce the background from jets to less that the $\gamma\gamma$ continuum. Simulation studies showed that it is possible to obtain a rejection factor for jets of 3000, while keeping a detection efficiency for photons of 80%, for $E_t > 50$ GeV ([5]).

The irreducible background cannot be reduced, just by definition. Anyway, a resonant signal can be observed over the $\gamma\gamma$ continuum if the reconstructed mass peak is enough narrow. The significativity of the signal, S, is defined as

$$S = \frac{N_S}{\sqrt{N_B}} \tag{1.29}$$

where N_S and N_B are the signal and background event number in the peak region. S depends on the reconstructed mass peak resolution as

$$S \sim \frac{1}{\sqrt{\sigma_m}} \tag{1.30}$$

Since the Higgs resonance is very narrow (few tens of MeV) in the mass region relevant for this channel, the width of the reconstructed peak is totally determined by the resolution of the involved detector, that is the electromagnetic calorimeter:

$$\frac{\sigma_m}{m} = \frac{1}{\sqrt{2}} \left(\frac{\sigma(E_1)}{E_1} \oplus \frac{\sigma(E_2)}{E_2} \oplus \frac{\sigma(\psi)}{\tan\psi/2} \right) \tag{1.31}$$

The first two terms in parenthesis come from the resolution on the energy measure for the two photons, and the third from the measure of the angle between their direction. A high integrated luminosity (100 fb^{-1} at least) and a good mass resolution (nearly 1–2%) are needed in order to observe the resonant peak over the $\gamma\gamma$ background.

In conclusion, we can observe in Fig. 1.7 the two photon invariant mass, for a 120 GeV Higgs, before (on the left) and after (on the right) subtracting the irreducible background. The mass peak is enough clear.

Summing up all the contributions to the signal, from direct and associated production, and all the kinds of background in a region centered on the peak and large 2.8σ ($\sigma \sim 1.3$ GeV), we obtain Tab. 1.4. The event numbers correspond to an integrated luminosity of 100 fb^{-1}. The significativity is quoted in the last line. If we choose 5σ as the limit to declare the Higgs discovery, the $H \to \gamma\gamma$ channel is useful in the mass range 110 GeV $\leq m_H \leq$ 140 GeV.

---

[5] The "transverse energy" E_t is a commonly used concept in High Energy Physics; given a particle

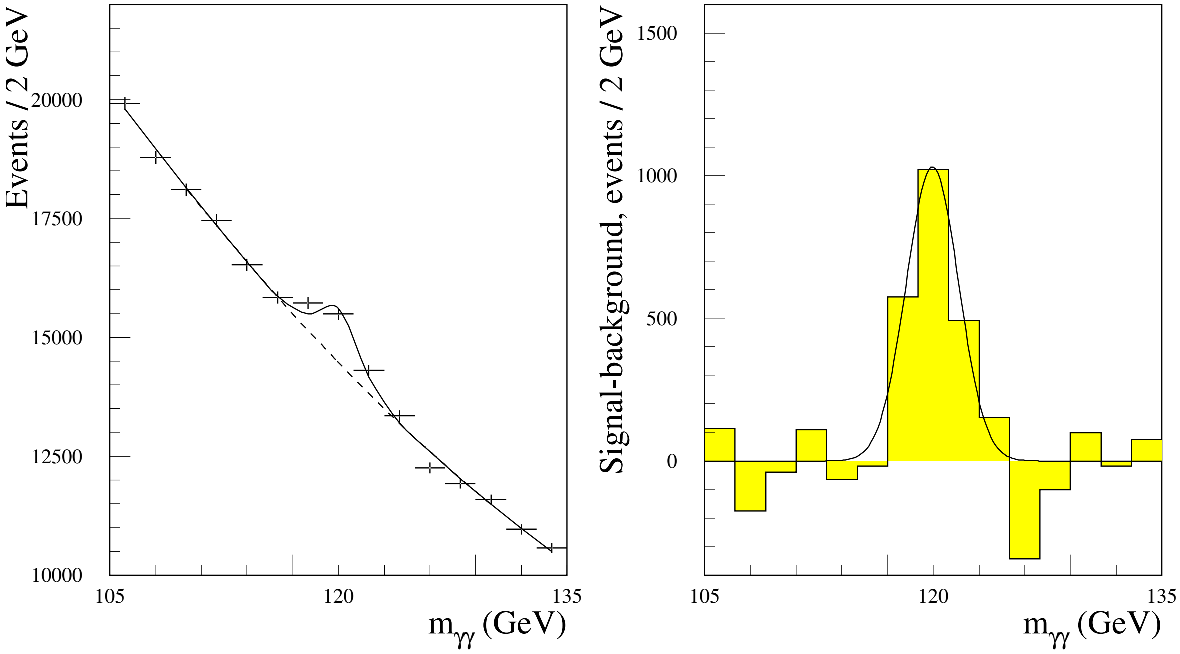

Figure 1.7: $\gamma\gamma$ invariant mass for a 120 GeV Higgs, with 100 fb^{-1} of data, before (on the left) and after (on the right) subtracting the continuum $\gamma\gamma$ background. [6]

m_H (GeV)	110	120	130	140	150
Signal	1207	1283	1186	973	652
Total background	47300	39400	33700	28300	23400
$S/\sqrt{B}$	5.6	6.5	6.5	5.8	4.3

Table 1.4: Signal, total background and significativity, as functions of the Higgs mass, for an integrated luminosity of 100 fb^{-1}.

1.2.2 $H \to b\bar{b}$

If the Higgs mass is lower than 120 GeV, the dominating decay is the one into $b\bar{b}$, with a branching ratio of nearly 90% (Fig. 1.2).

Using this channel to identify the Higgs signal, or any other resonance that may be interesting in this mass region, is practically impossible due to the background from direct production of $b\bar{b}$ couples, via QCD processes. In order to observe the Higgs using this channel, therefore, we have to select those events in which the Higgs is produced with another particle, that may provide a characteristic signature, useful to discriminate the signal from the background. Here we discuss the channels $q\bar{q} \to HW(Z)$ and $gg \to t\bar{t}H$. In both cases, the Higgs mass is calculated using the total 4-momenta of the jets recognized as b jets.

In both channels a W appears, either produced directly with the H, or in the decay of a t quark. If we require the W to decay into leptons, we can use the high p_t lepton to reject some background. The study of the channel HW put in evidence, anyway, that it is very difficult to select the signal from the decay $H \to b\bar{b}$ out of the very big QCD background.

The associated production $t\bar{t}H$ looks more promising. The complexity of the final state ($l\nu jjb\bar{b}b\bar{b}$, from $t \to bW \to bl\nu$, $\bar{t} \to \bar{b}W \to bjj$ and $H \to b\bar{b}$) permits to reduce strongly the main backgrounds, that are $t\bar{t}b\bar{b}$ and $t\bar{t}Z$. The W bosons can be completely reconstructed and the b quarks coming from the t decays are identified as those that minimize the quantity $\chi^2 = (m_{jjb} - m_t)^2 + (m_{l\nu b} - m_t)^2$. The remaining b jets are used to reconstruct the Higgs mass.

Figure 1.8 reports the expected $b\bar{b}$ invariant mass distribution: the signal peak is separated from the background. This is mainly due to $t\bar{b}jj$ events and combinatory mismatch. One of the fundamental experimental requisites to distinguish this channel is the energy and angular resolution for the jets (Sect. 1.2.1).

This channels is relevant in the difficult mass region 110 – 130 GeV. The significativity for $m_H = 120$ GeV and 30 fb^{-1} of integrated luminosity is expected to be 3.2 (Fig. 1.3).

---

with mass m and transverse momentum p_t, the following relation defines E_t:

$$E_t = \sqrt{m^2 + p_t^2} \tag{1.28}$$

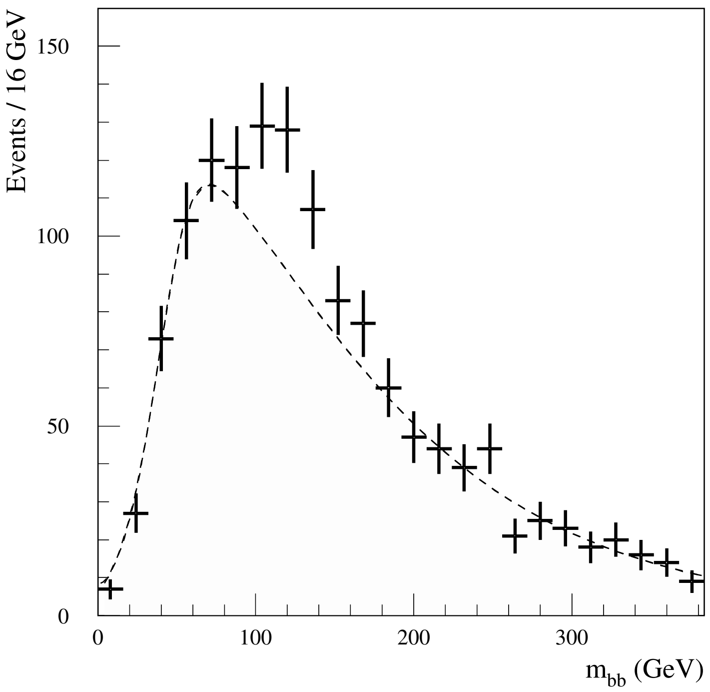

Figure 1.8: Invariant mass of the b quarks coming from the Higgs, after reconstructing the t quarks. The distribution was obtained for a 120 GeV Higgs mass and an integrated luminosity of 100 fb^{-1} [6].

1.2.3 $H \to ZZ$

The branching ratio of the channel $H \to ZZ$ can be neglected up to a $m_H \simeq 120$ GeV, as shown in Fig. 1.2, while the probability becomes quite higher for masses over this threshold, showing a significant valley only around 160 GeV, that is, when the decay $H \to WW$, with both the W on the mass shell, becomes possible.

The channel $H \to ZZ$ has quite a clear signature all over the mass range $m_H > 120$ GeV, where there are many different possible final states. The studies about the detection with the ATLAS detector concentrated on a final state with four charged leptons, potentially very efficient, reaching a signal to background ratio of 8 with 30 fb^{-1} of data, over the mass interval 200 GeV $< m_H <$ 500 GeV. Other Z decays channels where considered as well; for high values of the Higgs mass, the channels $H \to ZZ \to ll\nu\nu$ and $H \to ZZ \to lljj$ were studied, but the channels with $H \to WW$ provide better results.

The channel $H \to ZZ \to 4l$ can be observed in the mass range 120 – 600 GeV with a clear signature, that is four charged leptons[6] whose invariant mass distribution

---

[6] Actually we speak only of electrons or muons; final states with tauons don't permit a clear recon-

has a peak around the Higgs mass.

The expected background and, as a consequence, the research criteria, depend on the Higgs mass. If $m_H > 2m_Z$, then both the Z bosons are real and two couples of leptons, with same flavor and opposite charge, should have an invariant mass compatible with the Z mass. In this region the background is poor as, for example, the irreducible channel $pp \to ZZ \to 4l$. Furthermore, the intrinsic Higgs width is larger that the experimental resolution, so the detector performances are not critical. Figure 1.9 reports the expected signal for this channel.

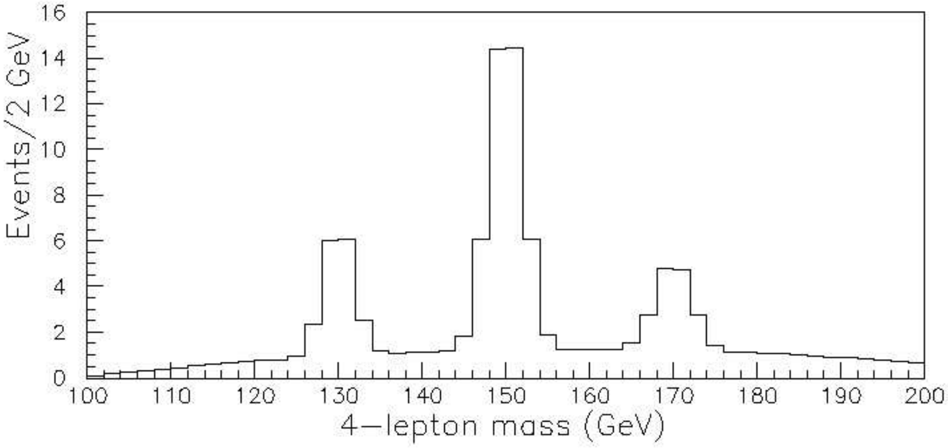

Figure 1.9: Invariant mass distribution of four charged leptons, for an integrated luminosity of 30 fb^{-1} and different values of the Higgs mass. The graph shows the mean expected event number [8].

For $m_H < 2m_Z$, on the contrary, the background becomes important. Beyond the above-mentioned irreducible continuum $pp \to ZZ \to 4l$, there are two reducible, but potentially dangerous, processes: $t\bar{t} \to 4l + X$ and $Zb\bar{b} \to 4l + X$. In the first case, two leptons come from the decay of the t quarks and two from the semileptonic b decays. In the second process, the Z originates a couple of leptons and the other two come, again, from the b quarks. Such kind of background car be rejected by imposing some requirements:

- the invariant mass of at least one couple of leptons must be compatible with the Z mass, thus eliminating the background from $t\bar{t}$;
- all the leptons must be isolated, in order to decrease the contamination form the decays $b \to lX$;

---

struction of the Higgs mass peak and, furthermore, are largely contaminated by QCD background.

- all the leptons must come from the interaction vertex; given the long mean time of the B mesons, the leptons from the b decay will originate at nearly 1 mm from the main vertex.

Figure 1.10 shows the expected signal for the Higgs boson in this mass range. In this case, the width of the peak is determined by the momentum and energy resolution of the detector, since the intrinsic H width is small in this mass region.

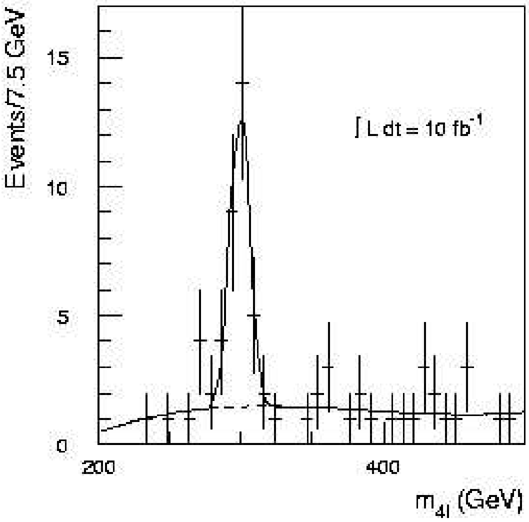

Figure 1.10: Expected signal in the channel $H \rightarrow ZZ \rightarrow 4l$, for a 300 GeV Higgs and an integrated luminosity of 10 fb^{-1} [6].

The results in Tab. 1.5, calculated for 30 fb^{-1} of integrated luminosity, show clearly the great discovery potential all over the mass range 200 GeV<m$_H$<600 GeV. They are not satisfactory for Higgs masses lower than 130 GeV and in the valley near the opening of the channel $H \rightarrow WW$. In the range 150-180 GeV we still need a channel able to provide a significativity greater than 5σ.

m_H (GeV)	130	150	170	180	200	240
Signal	11.4	26.8	7.6	19.7	54	88
Total background	2.61	2.98	3.10	3.1	7	15
$S/\sqrt{B}$	7.0	15.5	3.2	11.2	20.4	7.0
m_H (GeV)	280	320	360	400	500	600
Signal	90	90	91	79	39	19
Total background	17	16	13	14	7	6
$S/\sqrt{B}$	21.8	22.5	25.2	20.3	14.7	7.8

Table 1.5: Signal, total backgrounds and significativity for the channel $H \rightarrow ZZ \rightarrow 4l$, as a function of the Higgs mass, with 30 fb^{-1} of data.

For masses over 600 GeV, since the inclusive Higgs production cross section becomes smaller, the counting rate for this channel becomes too little and so it is necessary to look for other detection methods. For large values of the Higgs mass, between 500 and 700 GeV, the channel $H \rightarrow ZZ \rightarrow ll\nu\nu$ was studied, as it has a branching ratio six time bigger than the decay into four charged leptons. With 30 fb^{-1} of integrated luminosity, the significativity of this channel is 25.6 at $m_H = 500$ GeV.

1.2.4 $H \rightarrow WW$

For Higgs mass in the range 130 – 200 GeV, the reaction with the highest significativity is $qq \rightarrow qqH \rightarrow qqWW$ (Fig. 1.3), where the Higgs boson is produced through the boson vector fusion mechanism.

This process consists in two electro-weak boson being irradiated by two quarks and colliding to form a Higgs boson. The production mechanism offers some kinematical characteristics that make its signature very peculiar. Indeed, the quarks that emitted the vector boson are found in the final state with a fly direction that is typically very close to the beam, and, as there is no color exchange between the two protons, the hadronic activity in the central part of the detector is very low.

Therefore, two forward jets are required, quite close to the beam, with opposite signs for the pseudo-rapidity; a veto is posed on the central jets, thus rejecting those events that present hadrons with discrete transverse momenta. The last cut is particularly incisive against background events from $t\bar{t}$ interactions, characterized by a big number of jets.

Despite the low cross section of this channel ($\sigma \sim 4$ pb at $m_H \sim 130$ GeV), its peculiar signature makes good results achievable. Indeed, the study of the Higgs production through vector boson fusion has greatly enhanced the discovery potential in the intermediate mass range (120-200 GeV, Fig. 1.3).

For Higgs masses heavier that 160 GeV, the main decay process is $H \rightarrow WW$. The analysis of this channel is particularly interesting where the $H \rightarrow ZZ \rightarrow 4l$ process cannot give an exhaustive answer about the existence of the Higgs boson. Therefore, its natural to concentrate the study for those values of the Higgs mass around 180 GeV, where the BR ($H \rightarrow ZZ$) has a valley, and for very large masses, $m_H > 600$GeV, where the expected rate of ZZ is too low.

The favorite channel in the intermediate mass range is $H \to WW \to l\nu l\nu$. Despite this channel does not permit to reconstruct the Higgs mass, but only the "transverse mass"[7], it is a good candidate to provide a clear signal about the existence of the Higgs, as its decay fraction is nearly 100 times bigger than the ZZ one around $m_H = 170$ GeV.

Only final states with muons or electrons were examined. The main irreducible backgrounds are due to the continuum of $WW \to l\nu l\nu$ and $ZZ \to ll\nu\nu$. The reducible backgrounds come from $t\bar{t}$ events, Wt, $Wb\bar{b}$, $b\bar{b}$ and $W + j$, with a jet identified as an electron. The final state is characterized by two charged leptons and some missing transverse energy. The Higgs boson is scalar, thus some angular correlations are imposed between the leptons, and they can be used during the analysis. In order to reject those events where the leptons are created by a Z, we require that the ll invariant mass be lower than 80 GeV; moreover, a veto is imposed on the jets in the central region. Finally, the significativity is calculated requiring that the transverse mass of the lepton–lepton system fall in the range $(m_H - 30)$ GeV $< m_T < m_H$.

Table 1.6 shows the results obtained with this channel, as a function of the Higgs mass, with an integrated luminosity of 30 fb^{-1}. The significativity is greater than 5σ in the region that is critical for the ZZ channel.

m_H (GeV)	150	160	170	180	190
$\sigma \cdot BR$ (fb)	610	790	800	705	550
Signal	240	400	337	276	124
Total background	844	656	484	529	301
$S/\sqrt{B}$	4.7	9.6	10.3	7.8	5.4

Table 1.6: Signal, total background and significativity for the channel $H \to WW \to l\nu l\nu$, as a function of the Higgs mass, with 30 fb^{-1} of integrated luminosity.

As the Higgs mass grows ($m_H > 600$ GeV) it becomes important to consider the process $H \to WW \to l\nu jj$, because its probability is four times higher than the channel with two charged leptons. The only difference with respect to the analysis described so far, is that we require two jets in the central regions, energetic and

---

[7] The "transverse mass" is defined by the following relation:

$$m_T = \sqrt{(\sum_i E_{ti})^2 - (\sum_i \vec{p_{ti}})^2} \quad (1.32)$$

where E_{ti} and p_{ti} are the transverse energy (see footnote at page 18) and momentum of the i-th particle.

with a little angle between them, coming from the hadronic decay of the W. The main backgrounds are the production of $W + j$, with the W decaying into leptons, $t\bar{t}$ and the continuum WW. The noise from $t\bar{t}$ is highly reduced by the restrictions on the jets. In conclusion, the result of the analysis are shown in Tab. 1.7, while the signal expected for ATLAS is reported in Fig. 1.11.

m_H (GeV)	600	1000
Signal	187	73
Total background	615	150
$S/\sqrt{B}$	7.0	6.0

Table 1.7: Signal, total background and significativity for the channel $H \rightarrow WW \rightarrow l\nu jj$, as functions of the Higgs mass, with 30 fb^{-1} of integrated luminosity.

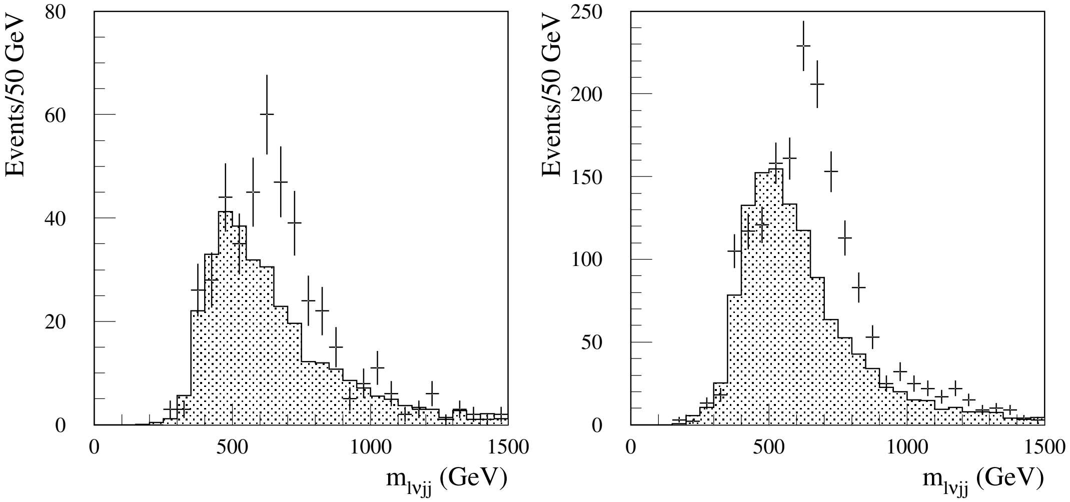

Figure 1.11: Expected signal in the channel $H \rightarrow WW \rightarrow l\nu jj$, for a 600 GeV mass Higgs boson, with an integrated luminosity of 30 fb^{-1} (on the left) and 100 fb^{-1} (on the right). The full histograms represent the background distribution; the points with the error bars include the signal, too [6].

1.2.5 $H \rightarrow \tau\tau$

In the last years, another process was studied: a Higgs, produced through the boson vector fusion mechanism, decays into a couple of tauons. This decay channel is particularly important for the discovery of the Higgs around 120-130 GeV, where it contributes to take the significativity (at 30 fb^{-1}) beyond the 5σ threshold, that is necessary before we can state the discovery of the Higgs boson (Fig. 1.3).

This channel can be identified through two different final states: both tauons de-

caying into leptons, $qql^+\nu\bar{\nu}l^-\bar{\nu}\nu$, or one τ producing lepton and the other creating hadrons, $qql^\pm\nu\nu h\nu$ [9].
For both the channels, the background is the same as for the process $H \rightarrow WW$: the main source of noise is the production $Z + j$, followed by the decay $Z \rightarrow \tau\tau$. The signal events are characterized by two forward jets, so a good reconstruction of these jets is fundamental to obtain an efficient selection of the signal.

1.3 The search for Supersymmetry

The supersymmetry, also known as SUSY, is one of the most theoretically motivated scenarios for physics beyond the Standard Model. The least robust part of the present electro-weak theory is the Higgs mechanism: radiative corrections to its mass can be very large, unless we apply further not so natural corrections. Moreover, the interactions may unify at high energies, but the Standard Model does not foresee any intersection point for the coupling constants.
No experimental evidence of the SUSY has been found up to now: this means that the supersymmetry does not exist, or the supersymmetric particles are too heavy ($m \gg 100$ GeV) to be accessed with the present particle accelerators. Since low energy supersymmetry predicts a complete spectrum of new particles with masses of the order of 1 TeV or less, the LHC collider should be able to give the last word about this class of theories.
Here we will discuss briefly the discovery potential of LHC for the most popular supersymmetric model: the Minimal Supersymmetric Standard Model (MSSM) with conservation of the R-parity.
The MSSM requires the existence of a minimum number of additional particles: five Higgs bosons (h, H, A, H^+, H^-) and a supersymmetric partner for each ordinary elementary particle. Such partners have a spin that differs of half a unit from the corresponding ordinary particle's spin. These SUSY particles are listed in Tab. 1.8. The mass of these particles are not known, anyway chargino and neutralino should be lighter than squark and gluino. Present lower limits for the mass of chargino and sleptons are about 100 GeV (from LEP experiments), while the limits for squark and chargino are around 250 GeV (from Tevatron). The R-parity is a multiplicative quantum number that takes the value $+1$ for the ordinary particles and -1 for the

SM particles	SUSY partners	Example of physical state
quark	squark	ũ, s̃, etc.
leptons	sleptons	ẽ, $\tilde{\mu}$, etc.
gluon	gluino	g̃
W boson charged Higgs boson	wino charged Higgsino	mixed into two charginos $\chi^{\pm}_{1,2}$
Z boson photon neutral Higgs boson	zino photino neutral Higgsino	mix into in 4 neutralinos $\chi^{0}_{1,2,3,4}$

Table 1.8: Standard Model particles and their Supersymmetric partners.

SUSY partners. If the R-parity is conserved, then the SUSY particles are always produced in pairs, and the lightest supersymmetric particle, indicated by LSP and identified with the neutralino, is stable. The LSP is very weakly interacting, so it can be detected only by measuring events with high missing transverse energy .

If they are kinematically accessible, squarks and gluinos will be produced profusely by the LHC. The Feynman diagrams describing the production of couples $\tilde{q}\tilde{q}$, $\tilde{g}\tilde{g}$ and $\tilde{q}\tilde{g}$ are similar to those that refer to the production of quarks and gluons. Some examples are described in Fig. 1.12.

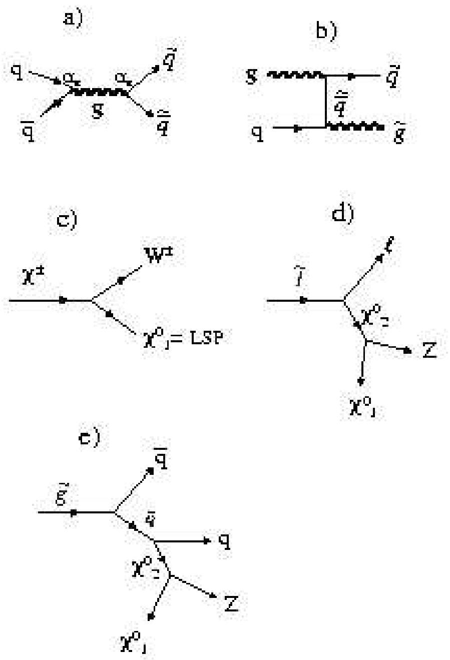

Figure 1.12: Examples of Feynman diagrams for processes that contribute to the production of q̃ and g̃ (a,b); diagrams for the decay of chargino, slepton and gluino (c, d, e).

For squark and gluino masses of 1 TeV, the production cross section is nearly 1 pb at $\sqrt{s} = 14$ TeV, thus nearly 30000 events should be produced in one year of low luminosity. For couples of charginos, neutralinos and sleptons, instead, the flux should be much smaller, as these processes are mediated by the weak interaction. According to the present experimental limits, squarks and gluinos are very heavy, so they should originate cascade decays with final states containing leptons, many jets and high missing transverse energy. Moreover, such decays will have high p_t, because they come from heavy particles. Such spectacular signatures can be easily recognized and extracted from the Standard Models background. As an example, Fig. 1.13 shows the missing transverse energy distribution expected in ATLAS, both for the SM background and for a SUSY model where $m\left(\tilde{q}\right) = 900$ GeV, $m\left(\tilde{g}\right) = 600$ GeV and $m\left(LSP\right) = 80$ GeV. The event selection requires five high p_t jets in the final state and a missing transverse energy bigger than 300 GeV.

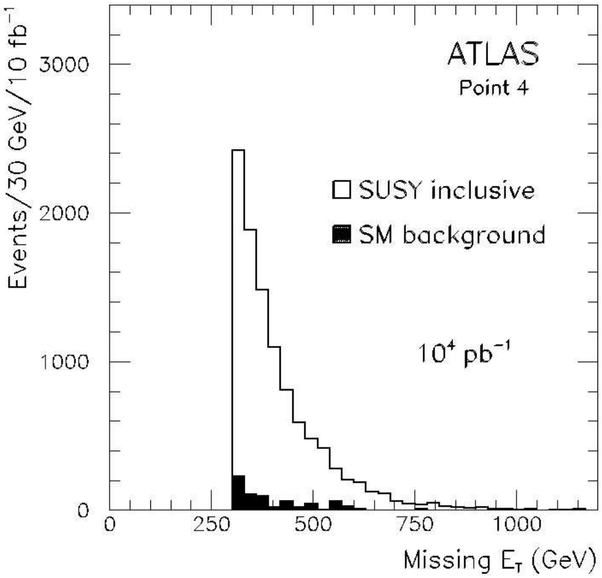

Figure 1.13: Reconstructed missing energy distribution expected in ATLAS, for an inclusive SUSY signal (white histogram) and for the SM background, at an integrated luminosity of 10 fb^{-1} [8].

After these cuts, in one year of data taking, at low luminosity, we expect nearly 12000 SUSY signal events and 600 SM background events, mainly due to $Z + j$, $W + j$ and $t\bar{t}$ events. Such an impressive significativity is not peculiar of the selected point in the parameter space, but rather a general characteristic for the observability of SUSY models, with R-parity conserved, at LHC. With similar analysis, it would be possible, in only one year at low luminosity, to find out (or exclude) squarks and gluinos with masses up to 1.5-2 TeV.

If the SUSY will be discovered at LHC, many precision measurements will be possible on the masses of the SUSY particles [6]. This should lead to restrict the parameters of the theory, for minimal models, to a precision of order 1%.

Chapter 2

Atlas Experiment at LHC

2.1 The Large Hadron Collider (LHC)

Following the recent results from LEP (Large Electron Positron collider) and trying to answer to the large number of still open questions in High-Energy Physics, a new accelerator is being built in the former LEP tunnel at CERN: the **L**arge **H**adron **C**ollider (LHC).

LHC is a proton-proton collider that will run at 14 TeV of center of mass energy ($\sqrt{s}$=14 TeV). The CERN's existing accelerators (LINAC, BOOSTER, PS and SPS shown in Fig. 2.1) will be used to accelerate protons up to 450 GeV. After the injection into the LHC, the two beams will reach the energy of 7 TeV. In addition to p-p collision, the LHC will be able to collide heavy nuclei (Pb-Pb) at the energy of $\sqrt{s}$=5.5 TeV per nucleon [10].

Along the 27 km there are eight linear sections Interaction Points (IP), each one 528 m long, and in four of these intersections, the following detectors:

- ATLAS, **A T**oroidal **L**HC **A**pparatu**S**
- CMS, **C**ompact **M**uon **S**olenoid
- ALICE, **A L**arge **I**on **C**ollider **E**xperiment
- LHCb, **L**arge **H**adron **C**ollider **b**physics.

In Fig. 2.2 the LHC ring is shown; the four experimental sections are visible together with the collimation systems, RF systems and beam dump insertions.

The two proton beams will travel in separate beam pipes (separated by 194 mm)

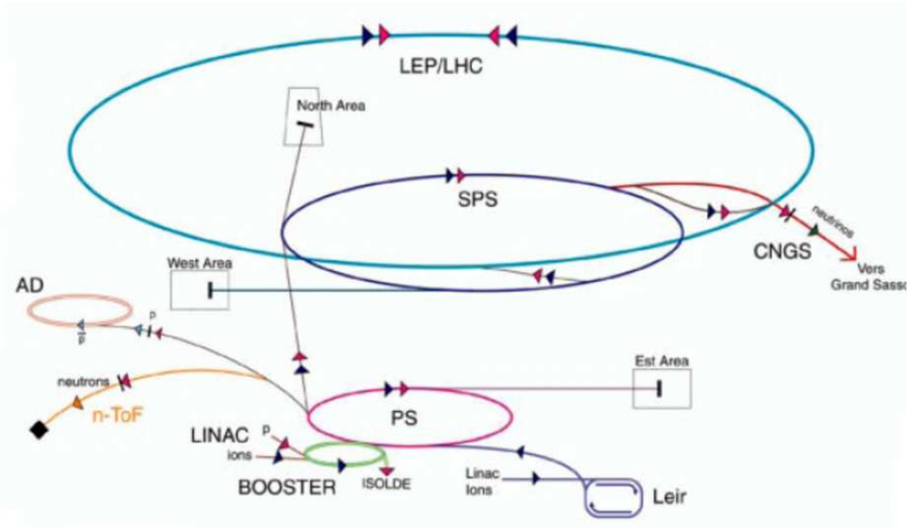

Figure 2.1: The CERN accelerator chain.

passing through oppositely directed magnetic field of 8.38 T. These fields are generated by dipole and quadrupole superconducting magnets operating at 1.9 K.
The protons will come in roughly cylindrical bunches, few centimeters long and few microns in radius. The distance between bunches is 7.5 m, in time 25 ns; they will collide in the 110 m long region, without any magnetic field. At the high luminosity ($10^{34}\ cm^{-2}\ s^{-1}$), the two beams will be made of 2835 bunches, even if, during the initial phase, LHC will run at the lower luminosity of $10^{33} cm^{-2} s^{-1}$ ([11]).
The luminosity $\mathcal{L}$ of a collider is a parameter depending on the machine; it connects the interaction cross section (σ) with the number of events per time unit (Rate):

$$\mathcal{R} = \mathcal{L}\sigma_{int} \tag{2.1}$$

The luminosity is related to the machine parameter, through:

$$\mathcal{L} = F\frac{f n_1 n_2}{4\pi\sigma_x\sigma_y} \tag{2.2}$$

where f is the (particle bunch) collision frequency, n_1 and n_2 the number of particles per bunch, σ_x and σ_y are the parameters which characterize the beam profile in the orthogonal planes, respectively, and F, equal to 0.8, depends on the angle of the beams.

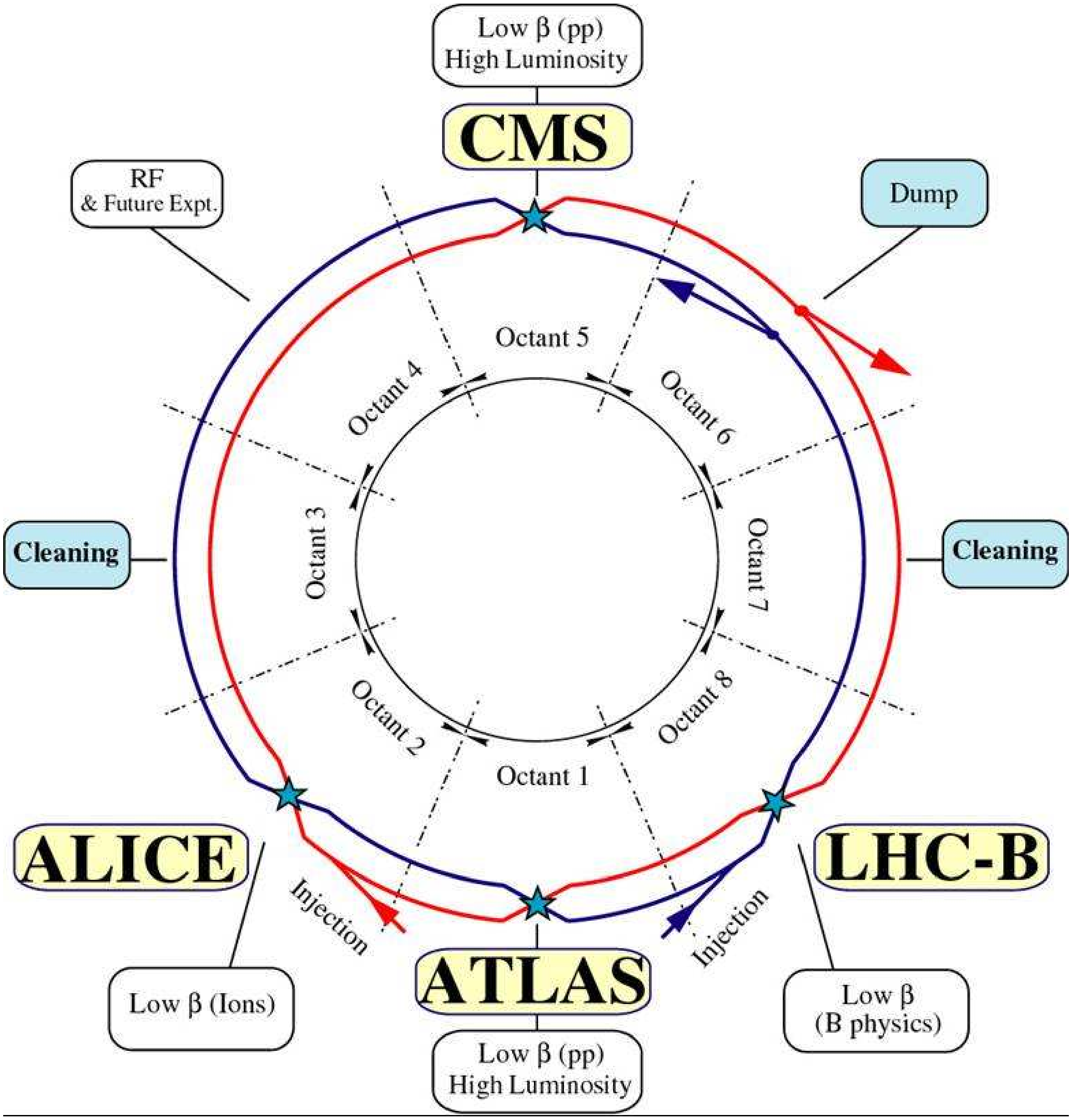

Figure 2.2: LHC view with the four experiments.

2.2 The ATLAS detector

The ATLAS detector (Fig. 2.3) has been designed to maximize the physics discovery potential offered by the LHC accelerator. The detector design is therefore guided by physics issues, such as the electroweak symmetry breaking, the search of super-symmetric particles with the possibility to study also new physics and heavy flavor physics. To meet all these physics goals, the ATLAS detector must be able to measure the energy-momentum four-vector with great precision for all particles produced, having a sufficiently long lifetime to be detected. If possible, the particle identification should be done with high efficiency ([11]).

The goal to exploit the full physics potential of LHC leads to the following basic requirements:

- a very good calorimetric system, composed of an electromagnetic calorimeter to identify and measure electrons and photons, and a hadronic calorimeter to have accurate measurements of missing energy and jets;
- an efficient tracking system for high p_T lepton momentum measurements and full event reconstruction at low luminosity;
- a high precision muon system that guarantees accurate muon momentum measurements;
- a large η and ϕ coverage.

The ATLAS coordinate system is a right-handed system with the z-axis pointing along the beam, the y-axis pointing upwards and the x-axis pointing towards the centre of the LHC ring. The transverse momentum (the momentum of the particle in the radius direction) and the pseudo-rapidity[1] $\eta = -\ln\tan\frac{\theta}{2}$ (where θ is the polar angle between the particle trajectory and the beam axis) are extensively used to describe the trajectories of the particles. The two sides of the detector upstream (+z) and downstream (-z) of the interaction point are labelled A and C, with B being used for elements around η=0. Region at $|\eta|$<1 is denoted as barrel, while the end-cap are at $|\eta|$>1. The system is also divided into 16 sectors, counted from 1 to 16. A sector is the azimuthal region definde by the barrel magnet structure. Sector 1

---

[1] The rapidity is defined as: $\ln\frac{(E+P_x)}{(E-P_y)}$, the pseudo-rapidity is the rapidity in the approximation of zero mass.

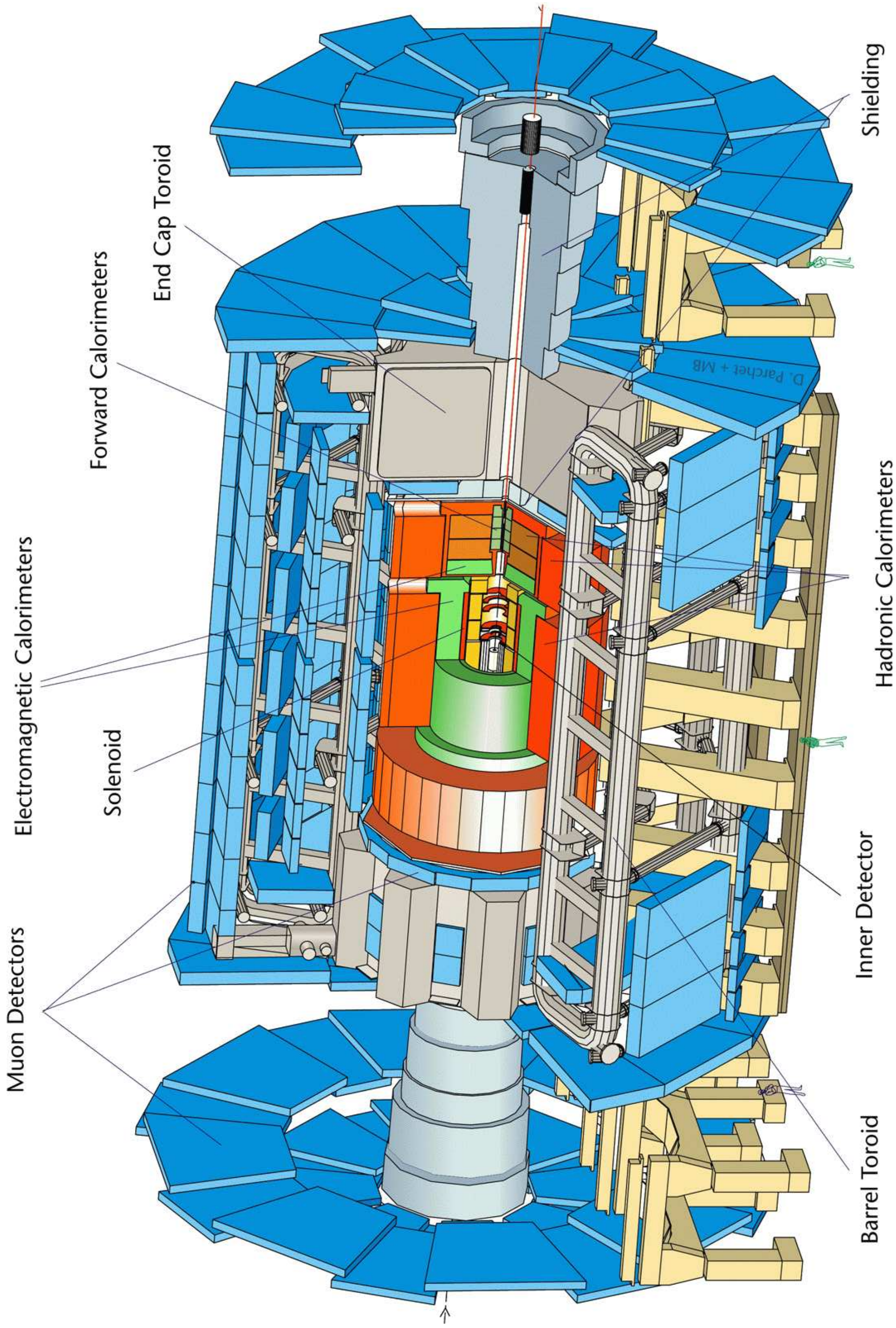

Figure 2.3: Three dimensional view of the ATLAS detector.

is the one which contains the positive x-axis (ϕ=0); then sector numbers increase in the direction of increasing ϕ, i.e., they are counted clockwise when looking from the interaction point into the positive z-axis, as shown in Fig. 2.4.

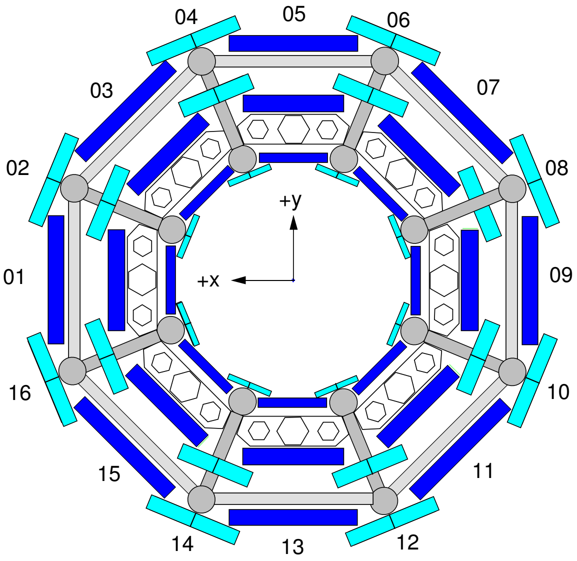

Figure 2.4: Definition of ATLAS sectors; view into the +z direction.

The innermost detector around the interaction region is the Inner Detector (ID). It is contained within a cylinder of length 7 m and radius of 1.15 m, in a solenoidal magnetic field of 2 T generated by a thin superconducting solenoid surrounding its cavity. It provides pattern recognition and precise measurements of vertex and momentum, combining the measurements of the high-resolution semiconductor pixel and strip detectors (inner part of the tracking volume) with the straw-tube tracking detectors with transition radiation capability (outer part).

The calorimeter system is located between the inner detector and the muon spectrometer. The Electromagnetic Calorimeter is a high granular liquid-argon (LAr) sampling calorimeter, that measures with great accuracy the energy of the shower produced by the photons, the electrons and the positrons crossing dense material. The Hadronic Calorimeter is a scintillator-tile calorimeter in the barrel region $|\eta| < 1.7$ and a LAr calorimeter in the end-caps ($1.7 < |\eta| < 3.2$) and in the forward region ($3.2 < |\eta| < 4.9$), providing an energy measurement for jets of particles.

The calorimeter is surrounded by a large superconducting air-core toroid consisting of independent coils arranged in an eight-fold symmetry, and generating a large magnetic field with a strong bending power within a light and open structure where the Muon Spectrometer is installed. The chambers of the Muon Spectrometer are mounted in three stations, minimizing the effect of multiple scattering and thereby achieving good momentum resolution. Muons with sufficient energy to cross all subdetectors are identified and their momentum measured.

The subdetectors and the trigger system are briefly introduced in the following sections, with special attention to the Monitored Drift Tubes chamber, which are object of this thesis.

2.3 Magnetic system

The ATLAS magnetic system consists of a central solenoid (CS) covering the Inner Detector, and three large air-core toroids, two in the end-caps (ECT) and one in the barrel (BT) that generate the magnetic field in the Spectrometer (Fig. 2.5 [12]).

The CS provides a solenoidal field of 2 T with a peak of 2.6 T in the windings. The position in front of the Electromagnetic Calorimeter requires a careful minimization of matter in order to avoid showering from particles before entering the calorimeter. Each of the three toroids, ECT and BT, consists of eight coils assembled radially and symmetrically around the beam axis in an open structure, providing a magnetic field peaked on 3.9 T (BT) and 4.1 T (ECT). Every coil in the barrel has its own cryostat, while coils in the end-cap, instead, are housed in a single large cryostat. All the magnets are indirectly cooled by helium at 4.5 K. The bending power of toroids is defined by the field integral $\int Bdl$, where B is the azimuthal field component, and the integral is taken on a straight line trajectory between the inner and the outer radius of the toroids. A scheme of the field line in the spectrometer is shown in Fig. 2.6.

2.4 Inner Detector

The Inner Detector combines high resolution detectors at the inner radii, with continuous tracking elements at the outer radii covering the range of $|\eta| < 2.5$ (Fig. 2.7) [13].

The overall layout consists of three different technologies: pixel detectors at radii between 5 and 15 cm from the interaction region, micro-strip detectors between 30 and 50 cm (SCT), then straw tube tracker at outer radii (TRT) (see Tab. 2.1).

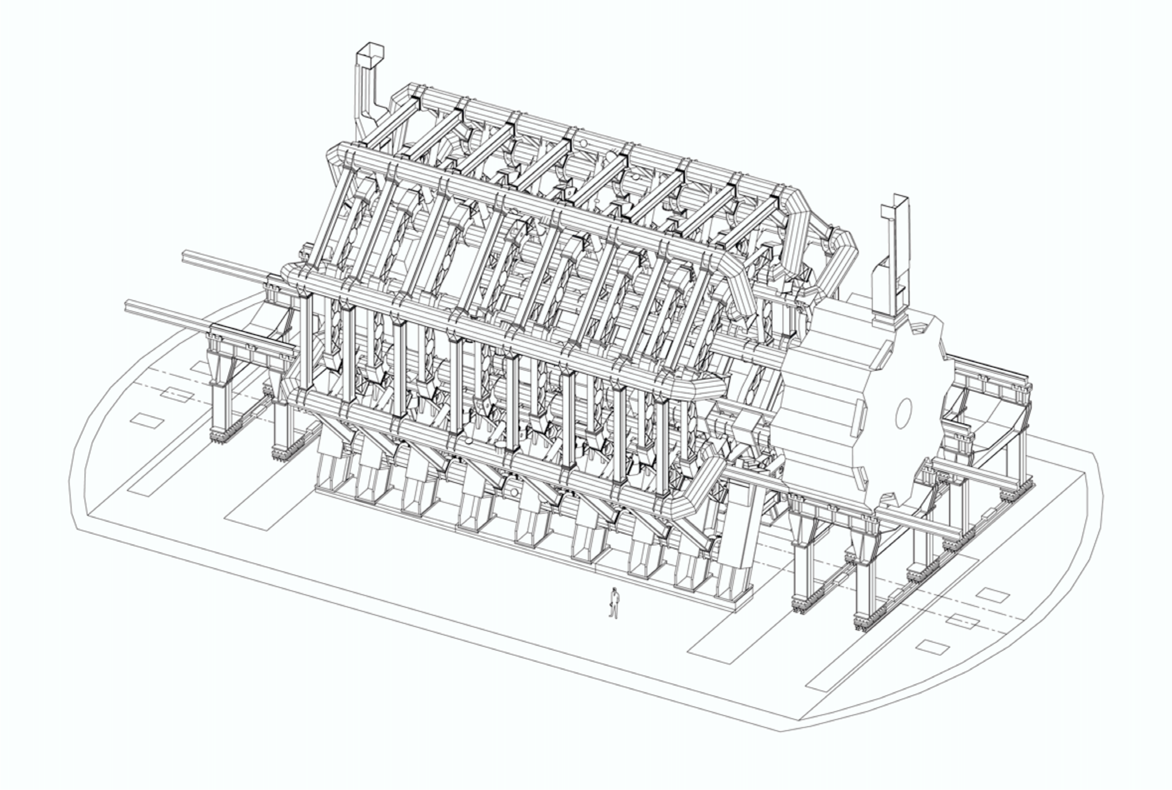

Figure 2.5: View of the superconducting air-core toroid magnet system.

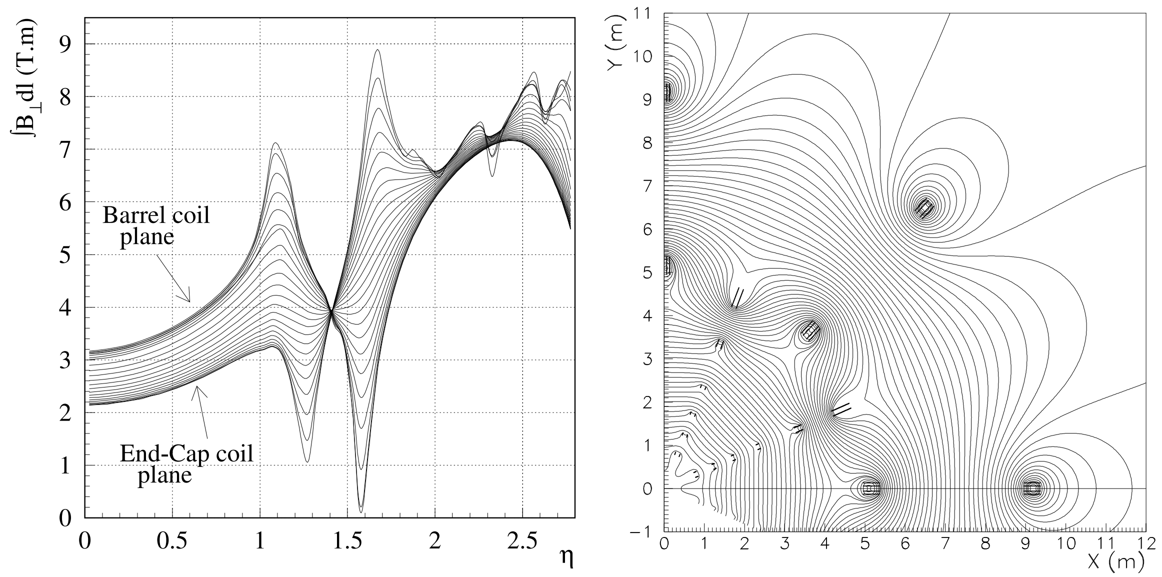

(a) field map

(b) bending power

Figure 2.6: (a): magnetic toroid field map in the transition region. Lines are drawn in a plane perpendicular to the beam axis in the middle of an end-cap toroid. (b): toroid bending power $\int Bdl$ of the azimuthal field component, integrated between the first and the last muon chamber, as a function of the pseudo-rapidity.

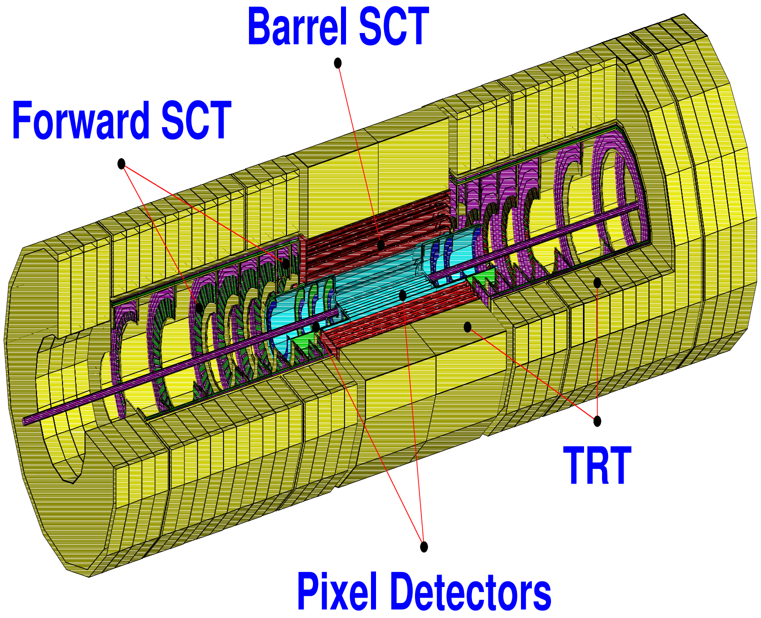

Figure 2.7: R-z view of the Inner Detector with its subdetectors.

System	η **coverage**	**Position in cm**	**Resolution in** μ**m**
Pixels	± 2.5	ΔR: 11.5-21.3	$\sigma_{R\phi}$=12 σ_z=66
	$1.5 - 2.7$	end-caps	$\sigma_{R\phi}$=12 σ_R=77
Silicon Strips(SCT)	± 1.4	R: 30, 40, 50, 60	$\sigma_{R\phi}$=16 σ_z=580
	$1.4 - 2.5$	end-caps	$\sigma_{R\phi}$=16 σ_z=580
TRT	± 2.5	ΔR: 56-107	$\sigma_{perstraw}$=170

Table 2.1: Parameters of the Inner Detector.

The first two detectors have a very high granularity, that permits to have measurements with a very good resolution in momentum and position of the vertex. The set-up of the detector was therefore carefully taken into account. The material in the inner detector, in fact, affects the resolution of the track reconstruction and adds dead material in front of the calorimeter. An excess of material causes deterioration of the detector performance via loss of low momentum particles, multiple Coulomb scattering affecting resolution, electron bremsstrahlung and photon conversion $\gamma \rightarrow ee$ (leading to a reduction of the important H$\rightarrow \gamma\gamma$ signal).

Using the space-point measurements of the different inner tracker layers, the helicoidal trajectory of the track is reconstructed. The five helix fit parameters refer to the point of closest approach to the beam axis (x=0, y=0). In the x-y plane, the fitted parameters are: $(1/p_T)$ the reciprocal of the transverse momentum; ϕ defined by $tan\,(\phi) = p_y/p_x$; d_0 the transverse distance to the beam axis. In the R-z plane, the fitted parameters are: $\cot\theta = tan\,(\lambda) \equiv p_z/p_T$; z_0 the z position of the track at this point. Simulations of the inner tracker response to minimum-ionizing-particles (muons) yield the following parametrization:$\sigma(\frac{1}{p_T}) \approx \left[0.36 \oplus \frac{13}{p_T\sqrt{\sin\theta}}\right](TeV^{-1})$;$\sigma(\phi) \approx \left[0.075 \oplus \frac{1.8}{p_T\sqrt{\sin\theta}}\right](mrad)$;$\sigma(\cot\theta) \approx 0.70{\cdot}10^{-3} \oplus \frac{2.0{\cdot}10^{-3}}{p_T\sqrt{\sin^3\theta}}$;$\sigma(d_0) \approx \left[11 \oplus \frac{73}{p_T\sqrt{\sin\theta}}\right](\mu m)$;$\sigma(z_0) \approx \left[87 \oplus \frac{115}{p_T\sqrt{\sin^3\theta}}\right](\mu m)$;

2.4.1 Pixel detector

The pixel detector is designed to achieve high precision as close to the interaction region as possible; the system provides three precise measurements over full solid angle (typically three pixel layers are crossed), with the possibility to determine the impact parameter and to identify the short-life particles.

There are three layers of pixels, 50 μm wide in Rϕ and 300 μm long. Thus the pixel detector yields good resolution in the bending plane of the solenoidal magnetic field, essential for transverse momentum measurement. The position along the beam axis is measured with slightly less precision.

The inner layer (called the B-layer because of the important role in B-physics) covers full rapidity range $|\eta| < 2.5$. The other two barrel layers cover the rapidity range $|\eta| < 1.7$. Three end-caps disks are used to provide additional space points in the forward regions $1.7 < |\eta| < 2.5$ ([13]).

2.4.2 Semi-Conductor Tracker

The Semi-Conductor Tracker (SCT) is designed to obtain eight precision measurements per track at radii from 30 to 56 cm, contributing to the measurements of momentum, impact parameter and vertex position.
It consists of four double layers of silicon strips, with each double layer composed of strips aligned in the azimuthal direction and strips rotated by 40 mrad with respect to the first set. The combination of the two measurements allows the determination of a two-dimensional space point with a resolution in $R\phi$ plane of $\approx 17\mu m$ and in the z coordinate of $\sim$ 570 μm that permits to resolve ambiguities in the pattern recognition (assigning hits to track in the dense tracking environment). The strips have 80μm pitch and are 12 cm long covering a large area (60 m^2) with a relatively small number of readout channels ($\sim$ 6 million) ([13]).

2.4.3 Transition Radion Tracker

The Transition Radiation Tracker (TRT) is based on straw detectors; they are used at large radii where the track density is relatively low giving a number of 36 points per track. This insures good pattern recognition performance for a continuous tracking. It consists of 36 layers of 4 mm diameter straw tubes with a resolutions of $\sim 200\ \mu m$, inter-spaced with a radiator to emit transition radiation (TR) from electrons. There are two thresholds for recording hits, the high threshold being used to detect TR photons. The emission of TR photons is a phenomenon with a threshold which depends on the relativistic velocity p/m, at $\beta\gamma \geq 1000$. Charged particle that cross an inhomogeneous medium, with materials of different electrical properties, emits a transition radiation in the X-rays region.
In the TRT, multiple polyethylene foils act as radiators. Interleaved with the radiator are layers of straws filled with a gas mixture. These have a dual functionality; the same straws measure the passage of charged particle through the gas ionization and the transition radiation X-rays absorbed by the gas molecules.
The number of transition radiation emissions along the track forms a powerful discriminant variable for electron/pion separation; this separation improves when the electron p_T increases from 0.5 GeV to 4-5 GeV, while for greater p_T the separation decreases, because at higher energies the relativistic rise in dE/dx causes the

pions to deposit more energy and the number of TR photons emitted to become comparable with the number of TR photons emitted by electrons ([11]).

2.5 Calorimeter system

The ATLAS calorimeter system (Fig. 2.8) measures the energy (and $\theta - \phi$ direction) of all particles and jets produced in the collision. The energy measurement is based on the shower development, a cascade of particles generated by relativistic particles through dense material ([12]). The calorimeter system consists of the electromagnetic (EM) calorimeter, covering the pseudo-rapidity region $|\eta| < 3.2$; the hadronic barrel calorimeter, covering $|\eta| < 1.7$; the hadronic end-cap calorimeters covering $1.5 < |\eta| < 3.2$; the forward calorimeters covering $3.1 < |\eta| < 4.9$. The different types of calorimeters are necessary because of the different interactions of electrons/photons and hadrons in the matter. Electrons and photons create a shower through bremsstrahlung, $e \rightarrow e\gamma$, and pair production, $\gamma \rightarrow e^+e^-$, in the electric field of the nuclei. The energy loss for a given material is characterized by the radiation length X_0. The lateral development of the shower is determined by

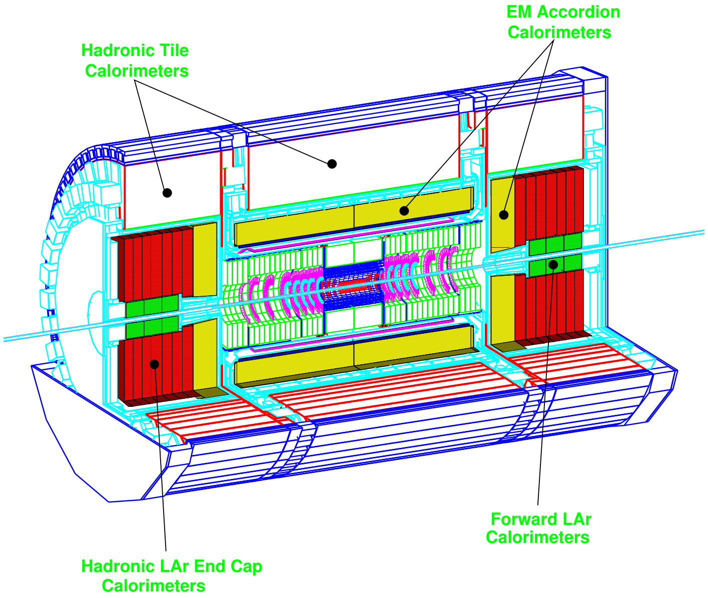

Figure 2.8: Layout of the calorimeter system.

the Moliere radius.

Hadrons produce a cascade of hadron-nucleus interactions. The longitudinal development of the shower is determined by the interaction length of the material. Hadronic showers contain a variable electromagnetic component from radiation of photons (bremsstrahlung) and π^0 decays. The shower shape of the hadronic showers is more irregular than the shape of the electromagnetic showers ([14]). The ratio between the response of the calorimeter to purely hadronic and purely electromagnetic part of the shower is called the e/h ratio. For a good energy resolution the value of e/h should be as close as possible to one. The size of hadronic showers depends on the interaction length of the material which is always longer than the radiation length. The radiation and interaction length are material dependent. Generally, for dense materials, the interaction length is up to an order of magnitude longer than the radiation length. This property is used in the ATLAS calorimeters to separate the electromagnetic and hadronic showers. Some particles do not generally create a shower. Energetic muons lose energy through ionization. The relatively small energy loss presents a challenging signal for the detector resolution and noise. The identification of electrons and photons is the most important issue for the calorimeters. Such a rejection can be achieved with a calorimeter of fine granularity in both the EM and hadronic part, to identify isolated energy depositions from electrons/photons and to veto hadronic energy behind the cluster in the EM calorimeter. The hight density of the EM calorimeter makes the difference between radiation and interaction length quite large, thus providing a good separation of the two types of showers.

The design of the electromagnetic calorimeter is driven by the requirements for energy and spatial resolution for the Higgs processes involving decays to electrons or photons. The $H \rightarrow \gamma\gamma$ decay of a standard model Higgs has a large background and a mass resolution around 1% is required. The dynamic range for the calorimeter in transverse energy extends from around 1 GeV for electrons from B-meson decays to a few TeV for the decay of a heavy vector boson.

The measurement of missing transverse energy is a way to measure particles escaping the detector without interactions. This can either be neutrinos or stable supersymmetric particles. To identify missing transverse energy the calorimeter needs to be hermetic. This means that the rapidity coverage has to reach $|\eta| = 5$

and any crack in the detector for cables and cooling has to be minimized.

Also the hadronic calorimeter needs to be thick enough to avoid leakage of hadrons into the muon system which would both reduce the resolution in missing transverse energy and give background in the muon system. A compromise between the total size of the ATLAS detector, the stopping power for low energetic muons, an acceptable rate of punch-through to the muon system and a good resolution in missing transverse energy, requires 11 absorption lengths of material in front of the muon system.

To minimize the fluctuations in the response of the hadronic calorimeter a low Z material, with comparable interaction length and radiation length, is a good choice. However, a compromise has to be made with the total size of the calorimeter which favors high density materials.

The energy resolution in the calorimeters is given by:

$$\frac{\sigma(E)}{E} = \frac{a}{\sqrt{E}} \oplus \frac{b}{E} \oplus c \tag{2.3}$$

where a depends on the stochastic fluctuations, b on the electronic noise and c on the calibration ([15]).

2.5.1 Electromagnetic calorimeter

The EM calorimeter is a dense, high-granularity Liquid Argon calorimeter, that permits to measure the energy of the photons and electrons, see Fig. 2.9. The electromagnetic shower develops in lead absorber plates. The thickness of the absorber plates is 1.5 mm in the barrel section and 1.7 mm and 2.2 mm in the first and second end-cap wheel. The absorbers are folded into an accordion shape and oriented along R (z in the end-caps) to provide complete ϕ symmetry without azimuthal cracks, as shown in Fig. 2.10.

The energy measurements are based on the determination of the ionization energy loss by charged components of the shower (electrons and positrons) in thin (2-6 mm) gaps between absorber plates: this gaps are filled with Liquid Argon and equipped with multiple electrodes.

The total EM calorimeter presents 24 (26) radiation lengths in the barrel (end-caps) region to reduce the error in the energy resolution due to longitudinal fluctuations of high energy showers.

The particle identification is achieved by a fine longitudinal and lateral segmentation. The EM calorimeter is longitudinally segmented in three layers plus a preshower sampler that corrects the energy loss in the material in front of the EM.

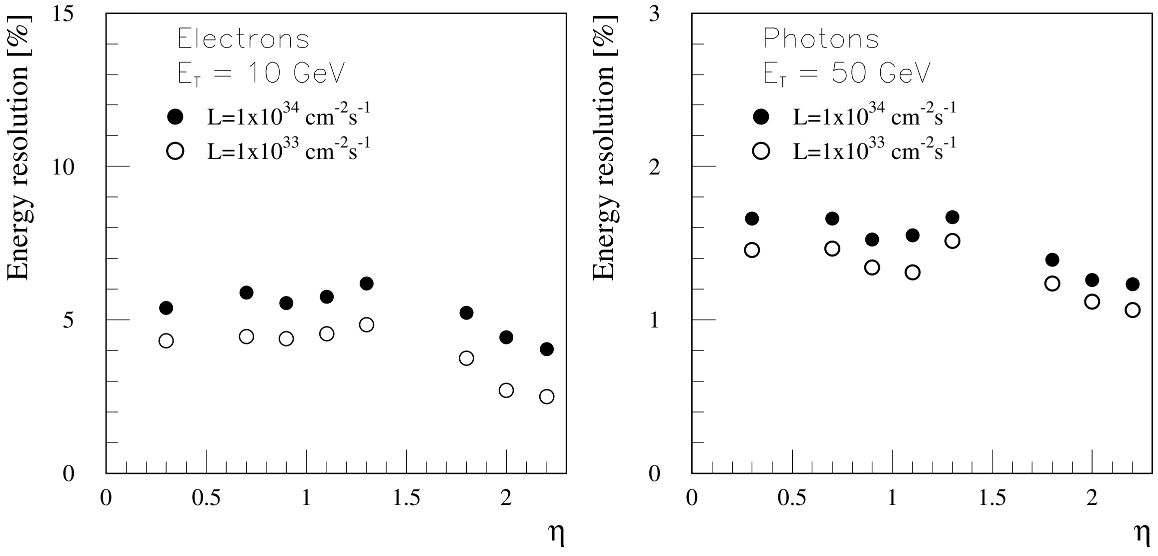

(a) electrons (b) photons

Figure 2.9: Different energy resolutions for electrons (left plot) and photons (right plot) at high (black points) and low luminosity (empty circles). The comparison is for electrons with E_T = 10 GeV and photons with E_T = 50 GeV.

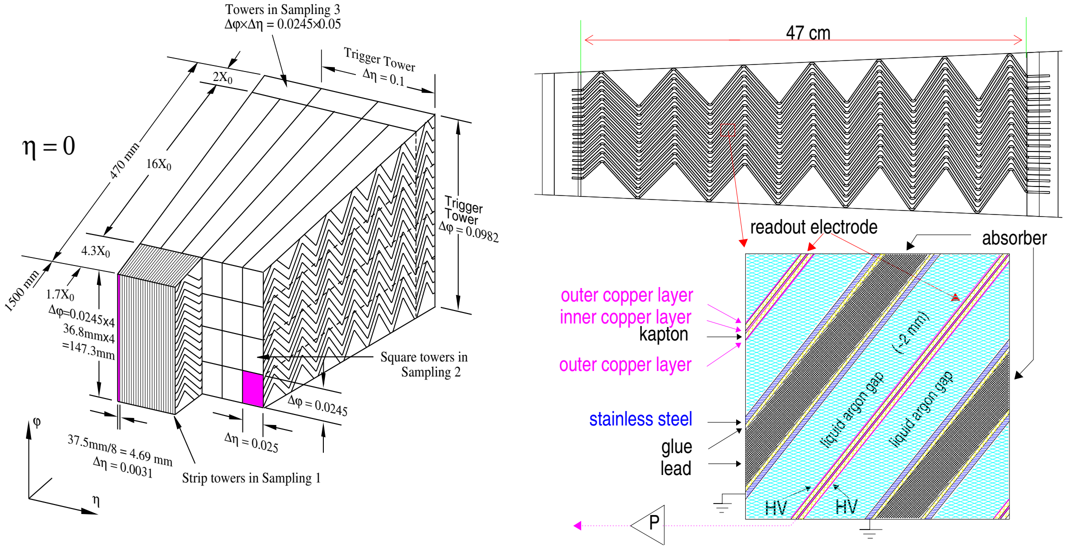

Figure 2.10: Readout scheme of the EM calorimeter, in evidence the accordion structure.

2.5.2 Hadronic calorimeter

The hadronic calorimetry in the barrel region uses iron absorbers with scintillator plates. This technique offers good performance combined with simple, low-cost construction. At larger rapidity, where higher radiation resistance is required, the hadronic calorimetry is based on the use of liquid argon.

The barrel region is composed of one central barrel and two extended barrels yielding a total pseudo-rapidity coverage of $\eta < 1.7$. Three longitudinal sections present 1.4, 3.9, and 1.8 interaction lengths to incoming hadronic particles. The total thickness, summing the $1.2\ \lambda$ in the electromagnetic calorimeter and the extra material in the support structures, reaches $11\ \lambda$. The geometry adopted consists of scintillator and iron tiles staggered in planes perpendicular to the beam axis. The readout used for a tile is a wavelength-shifting fiber for both sides coupled radially to the scintillator and two photomultiplier tubes; the cells are grouped in bundles to form readout cells of the desired segmentation($\delta\eta \times \delta\phi = 0.1 \times 0.1$), as shown in Fig. 2.11.

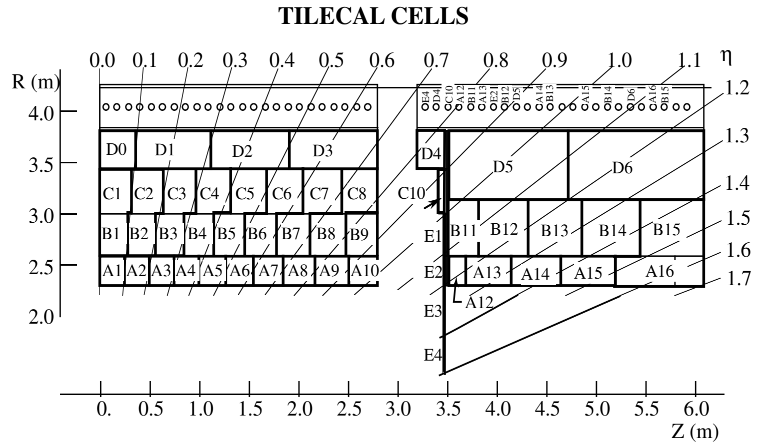

Figure 2.11: Trigger tower scheme of the Tile calorimeter.

2.6 Muon spectrometer

The Muon Spectrometer has been designed to measure transverse momentum, pseudo-rapidity and azimuthal angle of muons. Many of the physics processes of interest involve the production of muons. Therefore, the identification of muons provide an important signature for the event selection (trigger) of the experiment.

Also, the accurate determination of the momenta of the muon pairs allows the precise reconstruction of the short-lived particles that decay into muons (for example the detection of a supersymmetric Higgs boson through its muon decay channel). The possibility to have an accurate measurement of the muon momentum, independently from the inner detector, is achieved by integrating three large subsystems:

- A toroidal magnetic field generated by a large air-core barrel toroid and two air-core end-caps toroids, that minimizes the multiple scattering of the particle thanks to its air-structure.
- A muon first level trigger obtained by the fast signal of the dedicated chambers: Resistive Plate Chamber (RPC) in the barrel region and Thin Gap Chamber (TGC) in the end-cap region. These chambers determine the global reference time (bunch crossing identification) and the muon track coordinate in the non-bending direction.
- A system for precision momentum measurements via Monitored Drift Tube (MDT), and Cathode Strip Chambers (CSC) in the region $|\eta| > 2.7$.

The overall layout of the Spectrometer is reported in Fig. 2.12, which shows the different technologies employed ([17]).

The chambers are positioned at three locations (stations) along the muon trajectory. In the barrel, the three detector stations are mounted concentrically around the beam line at 5 m (inner), 7 m (middle) and 10 m (outer) radial distance. The chambers are arranged in projective towers (alignment rays monitor their position). In the end-caps, the disks are mounted perpendicularly to the beam line at 9 m (inner), 14 m (middle) and 20 m (outer) from the interaction region.

The precision measurements of the muon momentum in the barrel region are based on the sagitta of three stations in the magnetic field, where the sagitta is defined as the distance from the point measured in the middle station to the straight line connecting the points in the inner and outer stations.

In the end-caps, the situation is different; the magnetic field is present only between the inner and the middle stations, therefore the momentum is determined with a point-angle measurement: a point in the inner station and an angle in the combined middle-outer stations.

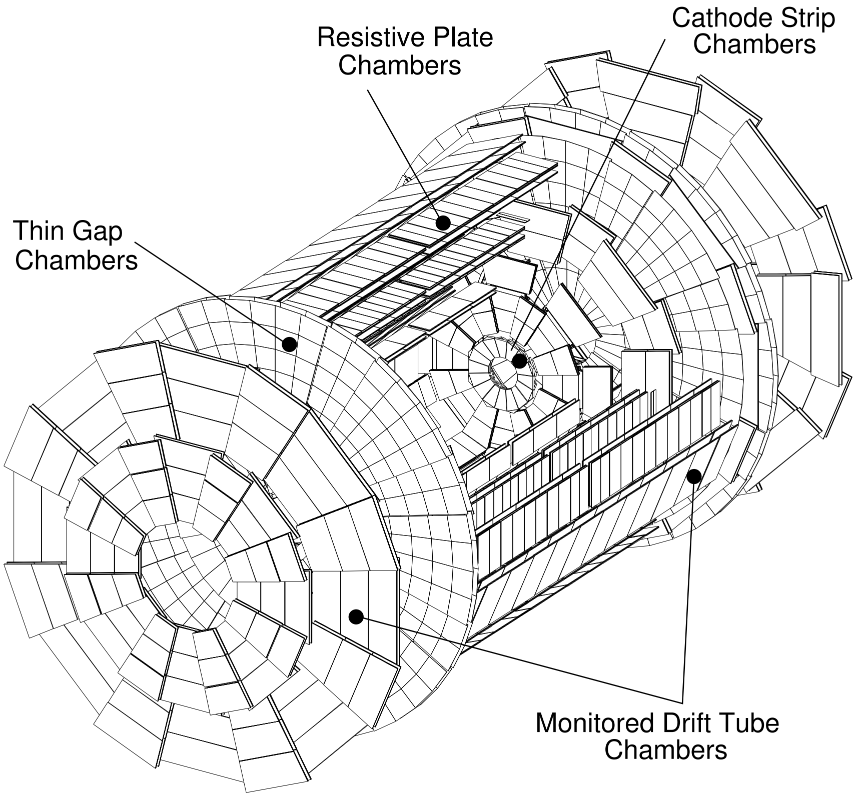

Figure 2.12: View of View of the ATLAS Muon Spectrometer.

The time difference between two consecutive collisions at LHC will be 25 ns, that corresponds to nearly 7.5 m for a particle traveling at the speed of the light. Furthermore for each bunch crossing, on average 20 simultaneous collisions take place, so that multiple events will pile up into the detector. The bunch crossing identification requires a fast trigger system with a time resolution better than 25 ns.

2.6.1 Monitored Drift Tube chambers

The MDT chambers perform the precision coordinate measurement in the bending direction of the air-core toroidal magnet and therefore provide the muon momentum measurement. They cover the barrel range of $|\eta| < 2.7$ and provide a single tube resolution of $\approx 80\ \mu m$ and a momentum resolution shown in Fig. 2.13.

Nearly 1200 chambers (~370.000 drift tubes) have been built for the barrel and the end-cap wheels. The Dipartimento di Fisica - Università della Calabria, has produced 32000 drift tubes, to assemble *Barrel Inner Large* (BIL), *Barrel Inner Medium* (BIM) and *Barrel Inner Rail* (BIR) at Rome and Pavia sites.

To improve the resolution of the chamber beyond the single-wire limit and to achieve adequate redundancy for pattern recognition, the MDT chambers are made up of two multilayers each. Every multilayer consists of 4 layers of drift tubes, for the inner stations, or 3 layers, for the middle and outer stations, as shown in Fig. 2.14 ([12]).

ATLAS drift tube operating principle

The basic detection element is a cylindrical aluminum drift tube of 30 mm diameter and 400 μm wall thickness. A central gold-plate tungsten-rhenium wire of 50 μm diameter is held under mechanical tension between two end-plugs. The tube works as a proportional counter with gas amplification. It is operated with a non flammable gas mixture 93% Ar and 7% CO_2 at 3 bar absolute pressure and a 3080 V voltage is established between the tube wall (cathode) and the wire (anode), thus resulting into a radial electrical field.

If radiation penetrates the tube, a certain number of electron-ion pairs will be created, whose average number is proportional to the energy deposited into the counter. Under the action of the electric field the electrons will be accelerated towards the anode and the ions towards the cathode, where they are collected. The basic feature of the ATLAS drift tubes is the proportional gas multiplication that occurs. Because of the 1/r dependence, the field becomes intense very close to the surface of the wire (order of 10^5 V/cm at less than 100 μm from the wire). If the field is strong enough to accelerate free electrons to an energy where they are also capable of ionizing gas molecules in the tube, an ionization cascade takes place.

This avalanche occurs very quickly and almost entirely within a few radii of the wire. The number of electron-ion pairs in the single avalanche depends on the gas composition and density and on the voltage applied to the wire. This multiplication factor can be as high as 10^6 so that the output signal is still proportional to the original ionization produced in the detector. The avalanche takes on a drop-like

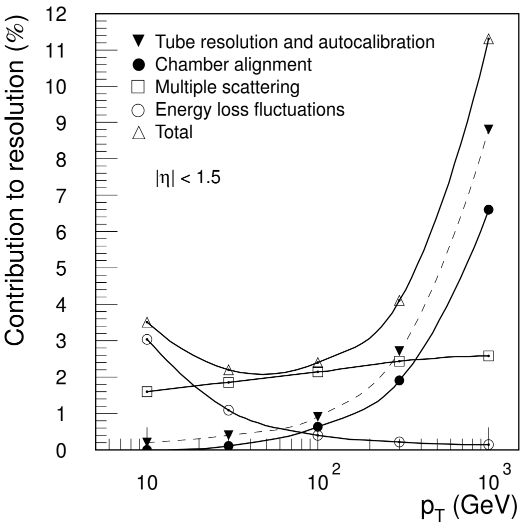

Figure 2.13: $\Delta p_T/p_T$ as a function of p_T for muons reconstructed in the barrel region $(\eta \leq 1.5)$.

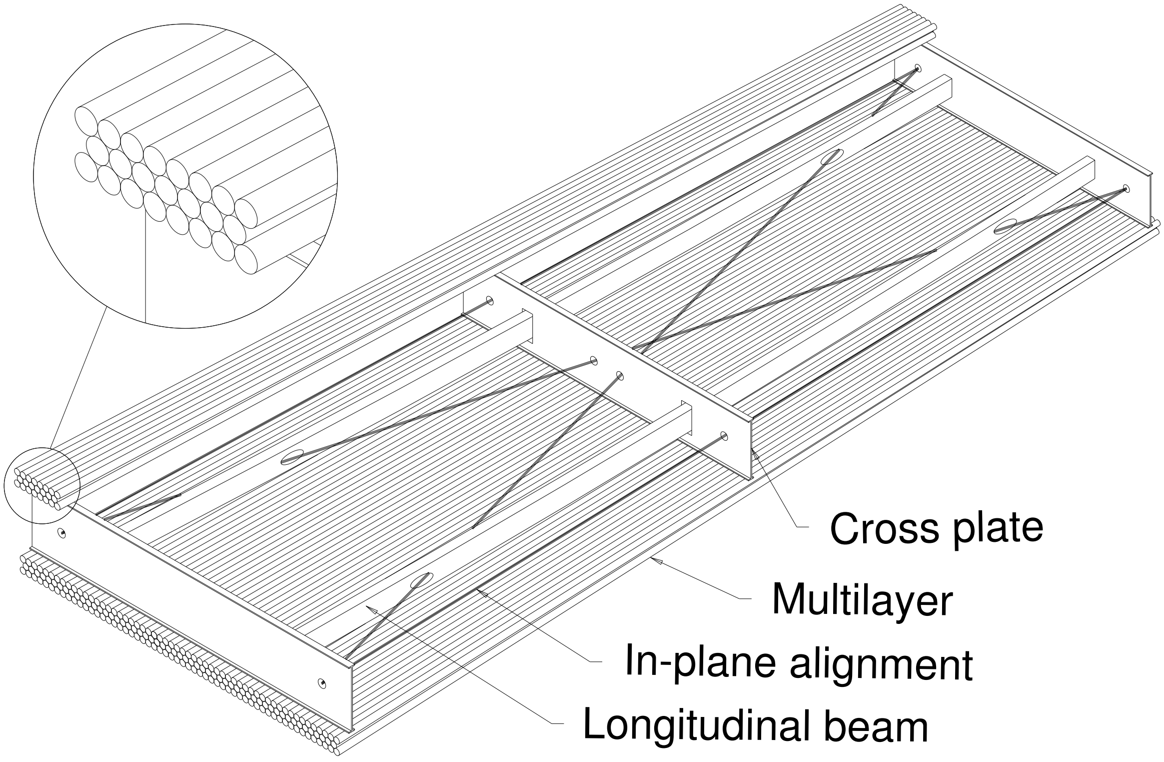

Figure 2.14: Schematic drawing of an MDT chamber. All the structural elements are shown (2×3 layers of tubes).

form with the electrons at the head and the positive ions in the rear. The avalanche remains well localized in the direction along the wire (about 0.1 mm).

The electrons are then collected very quickly (1 ns) while the positive ions begin drifting towards the cathode. This ion drift is mainly responsible for the signal seen on the electrodes. Indeed the pulse signal on the electrodes is formed by induction due to the movement of the ions and electrons as they drift towards the respective electrodes, rather than the collection of the charge itself. If the movement of the charges is fast enough, relatively to the time needed to an external power supply to react to changes in the energy of the system, the system itself can be consider closed and the contribution of electrons to the signal results small compared to that of the positive ions. Thus the faster rising part of the pulse is related with the arrival time of the electrons on the wire.

Working point

The quantity actually measured is the drift time of the primary electrons, that is the length of the time interval between the muon passing through the tube and the collection of the signal on the electrodes. Then the space-time relation is used to go back to the distance, from the wire, at which the muon crossed the tube. The chosen gas mixture Argon (93%):CO_2 (7%) provides a non linear space-time relation with a maximum drift time of about 700 ns [18], good aging properties, a single wire spatial resolution of $\sim$80 μm averaged over the whole electron drift distance (15 mm) and low drift tube occupancy. The working point for the ATLAS drift tubes has been chosen in such a way as the multiplication factor results of $2 \cdot 10^4$. The accumulated charge can be calculated from the following formula (2.4):

$$Q = \Phi \cdot d \cdot \bar{n}_e \cdot G \cdot e \cdot \Delta t, \tag{2.4}$$

being Φ the total expected rate, d the tube diameter, $\bar{n}_e$ the average number of electrons-ions pair, G the gas gain and e the electron charge. With a 500 Hz/cm^2 photon flux (taking into account the safety factor 5) and on average 1235 $\bar{n}_e$, in 10 years of ATLAS operation a 0.6 C/cm/wire will be accumulated:

$$Q = 500\ \frac{Hz}{cm^2} \cdot 3cm \cdot (2 \cdot 10^4) \cdot 1235 \cdot (1.6 \cdot 10^{-19}) \cdot 10^8 s = 0.6\ C/cm \tag{2.5}$$

The employed Ar-CO_2 mixture doesn't show any aging evidence within this limit. However, the bigger limit is the non-linear space-time relation, that, therefore, must be calculated accurately, using information from different tubes in the same chamber (autocalibration procedure [19]). Once the space-time relation is known, it is possible to reconstruct a track segment, as shown in Fig. 2.15. Finally, comparing the segments over different chambers, it is possible to calculate the bending radius of the trajectory and, hence, the momentum of the muon.

Electronics

The front-end read-out electronics consists of:

- high voltage distribution cards (called "hedgehogs");
- passive signal read-out cards (ROHH);
- active signal read-out cards (called "mezzanine" cards);
- Chamber Service Module (CSM), consisting of a "mother" and a "daughter" boards, which handle the signals from mezzanine cards;
- the Detector Control System (DCS) read-out module which reads out diagnostic information from the chamber.

A single channel consists, therefore, of the chain from the high voltage hedgehog, through the anode wire, to the ROHH card, up to the channel on the mezzanine card, and finally the CSM [20] (Fig. 2.16). The mezzanine card contains the Amplifier-Shaper-Discriminator (ASD) [21] chip, which feeds shaped signals into the ATLAS Muon TDC (AMT) [22]. The AMT chip does time digitization with a 25/32 ns least count.

Each mezzanine card houses 3 ASD chips, 8 channels each, and one AMT with 24 channels. The signals from AMT chips are passed to the CSM and then shipped out to the Read-out Drivers of the main ATLAS DAQ (Data AcQuisition) system. The ASD utilizes a built-in Wilkinson ADC to measure the integrated charge of the MDT signals. This ADC reads out as a pulse whose width is proportional to the integrated charge and is digitized by the AMT as a time. Hence, the charge measurement is sometimes referred to as "charge width".

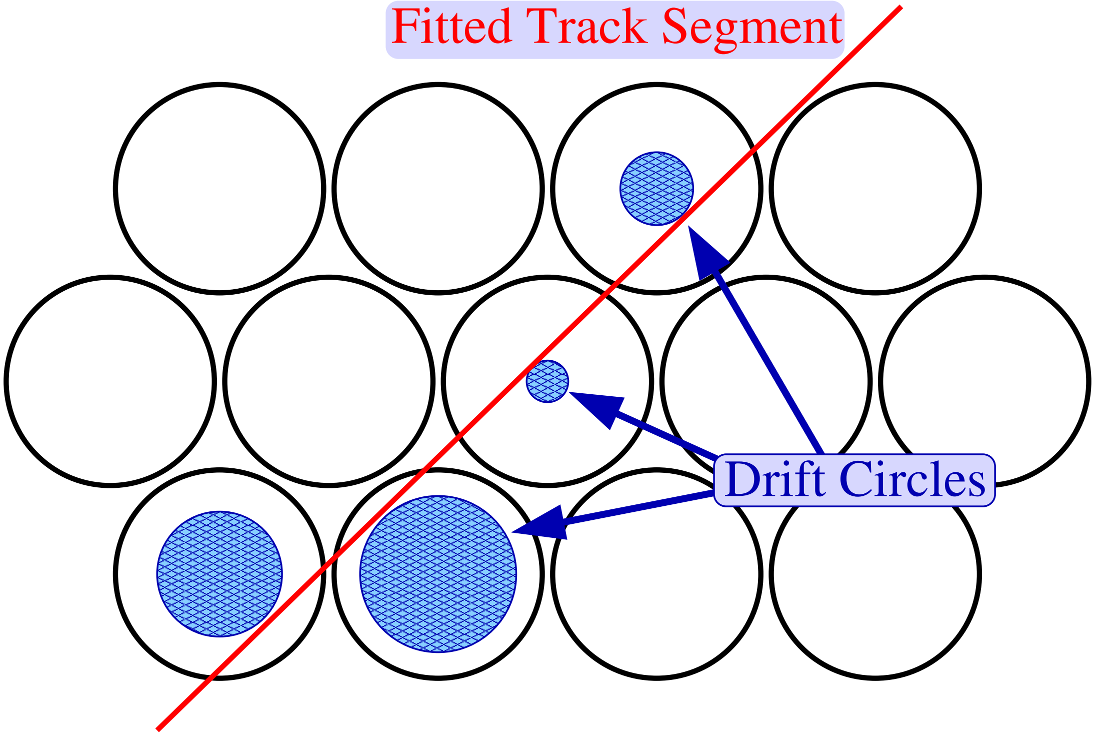

Figure 2.15: Example of a muon track segment reconstructed in an MDT multilayer of middle or outer barrel chambers.

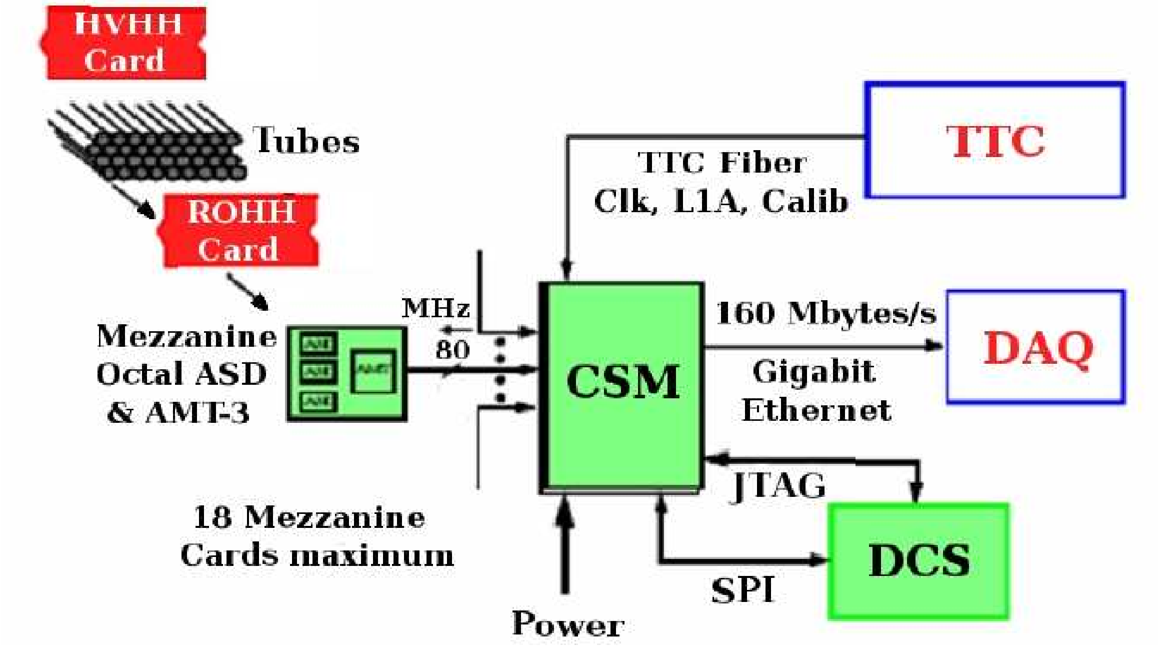

Figure 2.16: Schematic view of the front-end electronics.

Naming and conventions

Each MDT chamber is provided with a unique name (7 digits, YYYZZZZ), which contains information about the exact location in the spectrometer:

- Y, for the chamber type and global location
  - Y_1: region (B=barrel, E=endcap);
  - Y_2: station (I=inner, M=medium, L=large);
  - Y_3: L=large, S=small.
- Z, for a more detailed location
  - Z_1: number of a chamber within a station and sector (1-n);
  - Z_2: side A or C;
  - Z_3: sector number (1-16).

As an example, the names of some chambers mentioned in Chap. 5 stand for:

- BIL1A13: Barrel, Inner, Large, chamber n°1, side A, sector 13;
- BML2A13: Barrel, Medium, Large, chamber n°2, side A, sector 13;
- BOF1A12: Barrel, Inner, Feet (special chambers mounted on the ATLAS feet), chamber n°1, side A, sector 12;

2.6.2 CSC chambers

The Cathode Strip Chambers are multi-wire proportional chambers with a cathode strip readout and with a symmetric cell, where the anode-cathode spacing is equal to the anode wire pitch (see Fig. 2.17). The avalanche in the gas on the anode wire induces a signal on the segmented cathode.

The cathode strips are oriented orthogonal to the anode wire and are segmented, to obtain a position measurement with a resolution of $\approx 60\ \mu m$.

Other important characteristics are: good time resolution (7 ns), good track reconstruction and small electron drift time ([12]).

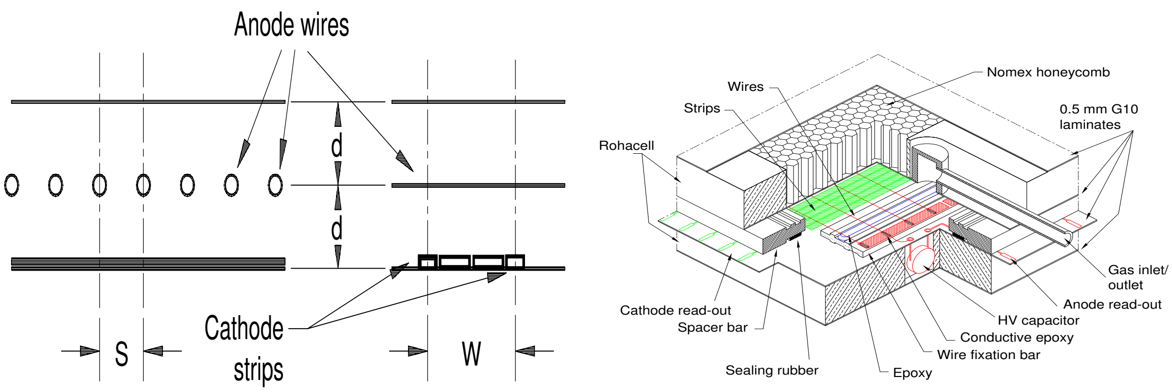

Figure 2.17: Schematic drawing of the Cathode Strip Chamber.

2.6.3 Resistive Plate Chambers

The Resistive Plate Chambers consist of a narrow gas ($C_2H_2F_4$) gap between resistive bakelite plates, covered with readout strips at the pitch of 30-39 mm (Fig. 2.18). Each chamber is composed of two rectangular detector layers, each one read out by two orthogonal series of pick-up strips: the η strips are parallel to the MDT wires and provide the bending view of the trigger detector; the ϕ strips orthogonal to the MDT wires, provide the second coordinate measurement which is also required for the offline pattern recognition.

The RPCs combine an adequate spatial resolution of 1 cm with an excellent time resolution of 1 ns.

2.6.4 Thin Gap Chambers

The Thin Gap Chambers are multi-wire proportional chambers filled with a highly quenching gas mixture of 55%CO_2 and 45% n-pentane (see Fig. 2.19).

This allows the chambers to operate in the saturated mode, with the following advantages: small sensitivity to mechanical deformations, nearly Gaussian pulses with small Landau tails and no streamer formation.

TGCs are constructed in doublets and triplets. The layers in the middle station are arranged in one triplet and two doublets, while in the inner station there is only one doublet that measures the ϕ coordinate. The anode wire, parallel to the MDT wires, provide the trigger information together with the readout strips arranged orthogonal to the wires.

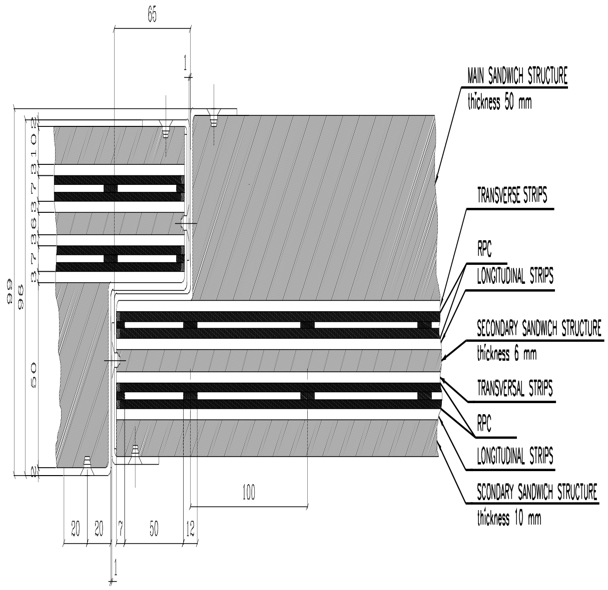

Figure 2.18: Structure of an RPC chamber.

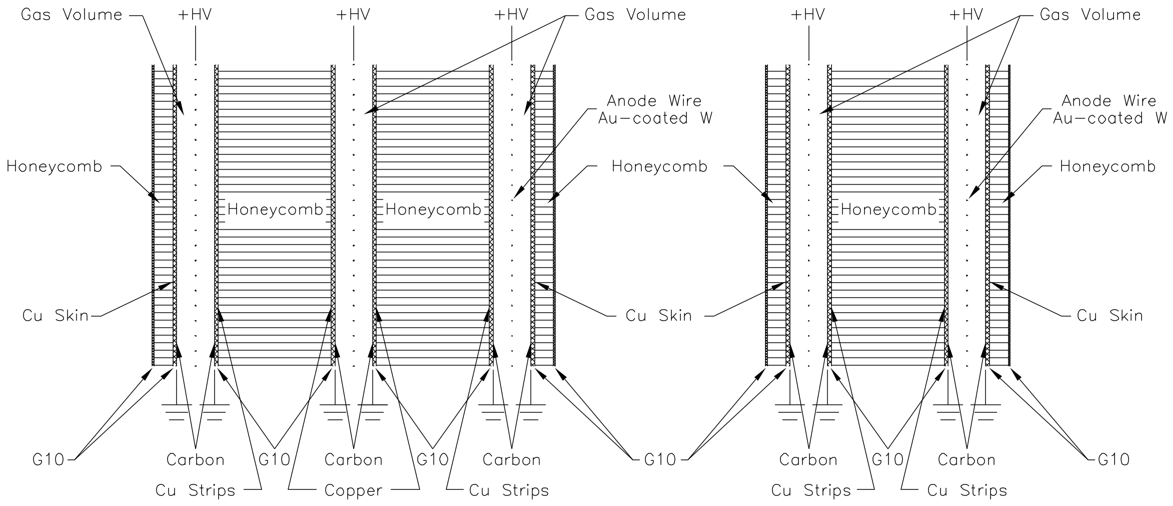

Figure 2.19: Schematic cross-section of a triplet (left) and of a double of TGCs.

2.7 The trigger system

The high LHC design luminosity (10^{34} cm^{-2} s^{-1}) will lead to nearly 10^9 interactions per second. Most of these interactions are minimum bias events of limited interest. Such a high data flux ($\approx 1.5\ MB$ every 25 ns) is far from the current data storage technology rate, that corresponds to a maximum trigger rate of ≈ 100-200 Hz ([23]). The trigger system is designed to bridge this gap, maintaining nearly all interesting physics events, while efficiently rejecting the minimum bias background. The system must be able to take a decision in a short time (latency time) without any loss of interesting physics signatures. The decision is achieved into three different steps or trigger levels (Fig. 2.20).

The first level trigger (LVL1) is designed to operate at a maximum pass rate of 75 kHz. The LVL1 latency is $2\ \mu$s ([24]). The information of all detector channels must be stored in "pipeline" memories, because the LVL1 latency extends over many of the 25 ns spaced LHC bunch crossings. The LVL1 decision is based on information with a coarse granularity of two sub-detector systems: the muon trigger chambers and the calorimeters. Quantities used in the LVL1 decision are typically: the estimated transverse momentum of muon candidates, the total energy deposited in the calorimeters, the missing (transverse) energy in the calorimeters and the occurrence of isolated energy depositions in the calorimeters. For events accepted by the LVL1, the information of all sub-detector systems is pre-processed and stored in the so-called Read-Out Buffers (ROBs).

The LVL1 trigger for muons is displayed in Fig. 2.21. In the barrel, two RPC planes sandwich middle chambers (stations S_2^{in} and S_2^{out}) to trigger low momentum muons, while only one plane is located on the inner side of outer chambers (station S_3) for high p_T particles.

The second level trigger (LVL2) uses both the LVL1 output and the data stored in the ROBs to further reduce the data rate to a maximum of 2 kHz. Even though the LVL2 has access to the full data, the selection is generally restricted to so-called Regions of Interest as flagged by the output of the LVL1. For a LVL1 muon trigger, the LVL2 will use the information from the precision MDT chambers to improve the muon momentum estimate, which allows a tighter cut on this quantity. For a LVL1 calorimeter trigger, the LVL2 has access to the full detector granularity and has, in

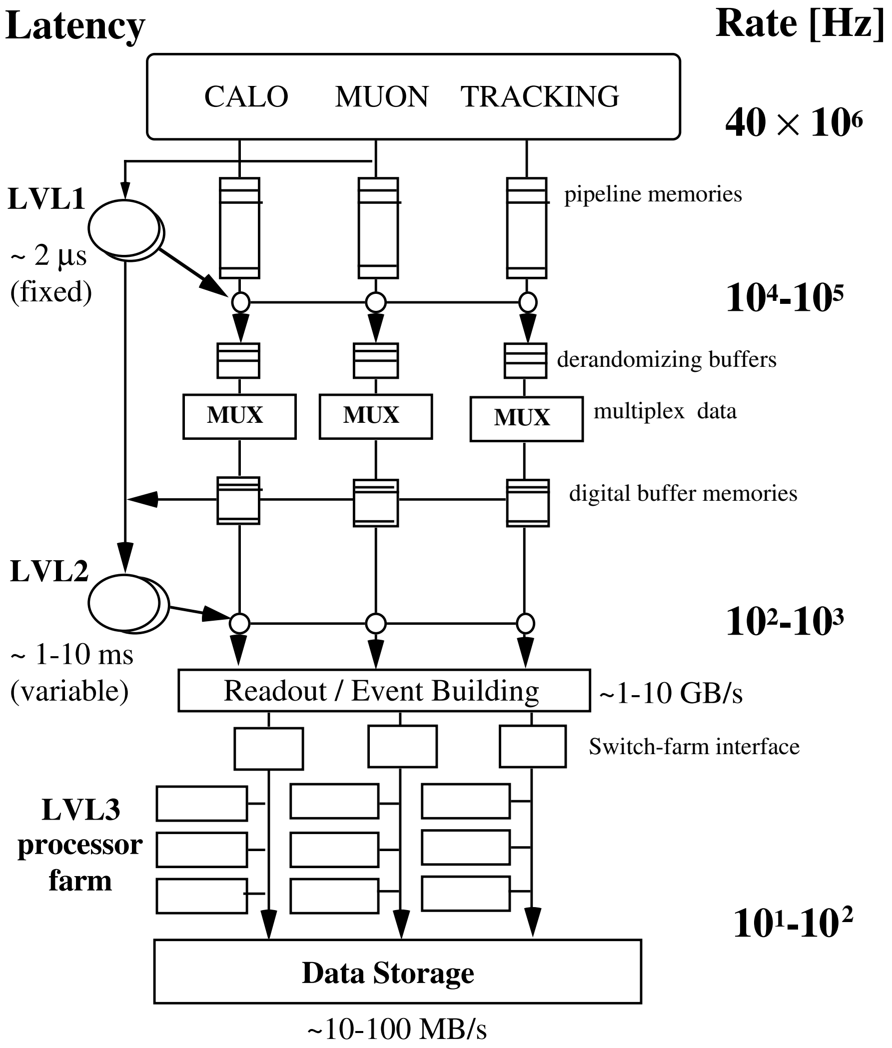

Figure 2.20: Schematic view of the ATLAS trigger system. The three levels (LVL1, LVL2, LVL3) are indicated, including the latencies for the first two.

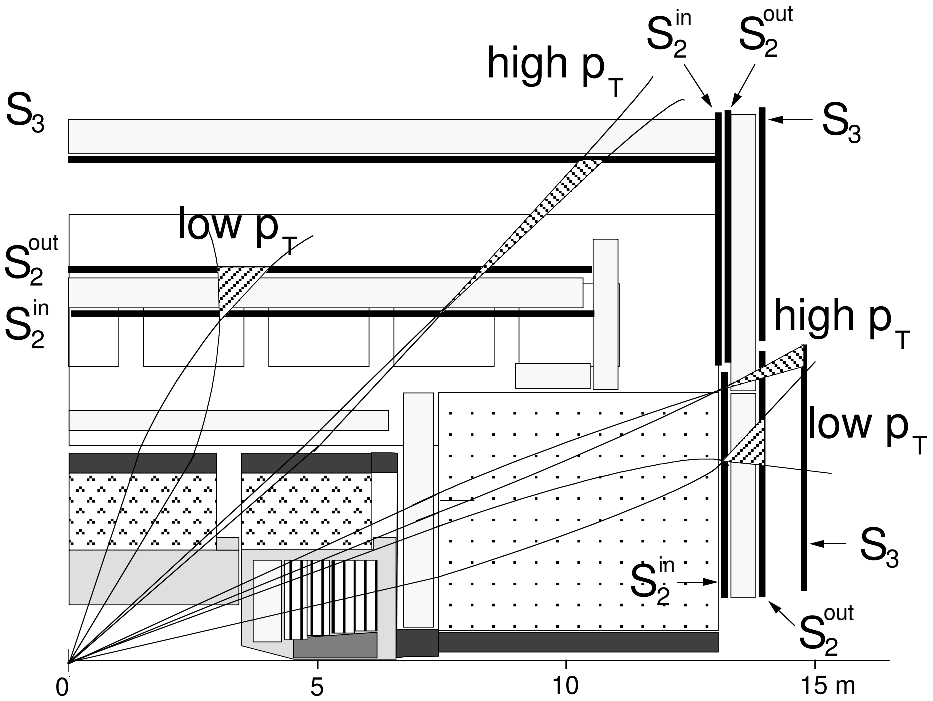

Figure 2.21: The LVL1 muon trigger scheme.

addition, the possibility to require a match with a track reconstructed in the inner detector. The LVL2 has an event dependent latency, which varies from 1 ms for simple events to about 10 ms for complicated events. For events accepted by the LVL2, the data fragments stored in the ROBs are collected by the Event Builder and written into the Full Event Buffers.

The third trigger stage is the Event Filter (EF): it uses the information stored in the event buffers to keep the rate of events sent to mass storage at a few hundreds Hertzs. The EF uses the best algorithms developed for offline reconstruction, like track reconstruction, vertex finding, etc., since it has access to the complete event. The stored data is reconstructed to yield quantities like tracks, energy clusters, jets, missing transverse energy, secondary decay vertexes, etc. These quantities are subject to various physics selection criteria in offline analysis too, for example to maximize the discovery potential for the Higgs particle. For the maximum trigger rate of 100 Hz, the data rate written to mass storage corresponds to 300 MB/s.

Chapter 3

High rate and background tests on MDTs

3.1 Motivation

In ATLAS, a large amount of particles, uncorrelated to the primary proton-proton collisions, will be produced from primary hadrons interacting with the forward calorimeter, the shielding material, the beam pipe and the other machine elements. In particular, Monitored Drift Tube chambers will experience a significant background of low energy (1 MeV region) neutrons and photons. From the simulation of background in the ATLAS hall [25], a total flux of 5 kHz/cm^2 is expected in the inner barrel MDT chambers under LHC nominal operation. This flux can be even 10 times higher for the end-cap chambers, where uncertainties in the simulation of shielding material are larger, and for the foreseen upgrade at higher luminosity (Super-LHC [26]).

High particle fluxes in the muon system influence parameters such as the rate capability of chambers, the aging of the detectors, the granularity and redundancy of the trigger instrumentation, the pattern recognition efficiency, or the momentum resolution tails induced by incorrect hit association. In particular, a high count rate in a Monitored Drift Tube, could affect the tube behavior itself, mainly for the modification of the electric field due to the accumulation of space-charge close to the wire. A high number of hits per event could also influence pattern recognition resulting in a loss of efficiency: background hits can mask the real hits belonging to a physical track, if they occur in the same tube (given the tube dead time of 700 ns).

To study MDT chamber performances under intensive photon and neutron rates at the level of LHC and Super-LHC, two tests have been performed by the INFN groups of Università della Calabria and Università di Roma TRE. Analysis results have already been published in [27], [28], [29], [30] and [31].
In this chapter, both tests will be described.

3.2 Radiation background in the muon spectrometer

The ATLAS muon instrumentation has been designed to offer the rate capability and robustness to the high fluxes required for running at nominal L=10^{34}cm^{-2}s^{-1} luminosity, including a safety factor 5 on estimated rate. The various subsystems, and in particular the MDT chambers, will have to survive 10 years of ATLAS operation at least.
The background in the Muon Spectrometer can be classified into two categories [25]:

- **primary background**: primary collision products penetrating the muon spectrometer through the calorimeter, which are correlated in time to the p-p interaction. Conventional sources of primary background are semileptonic decays of light (π,K $\rightarrow$ μ X) and heavy (c,b,t $\rightarrow$ μ X) flavors, gauge boson decays (W,Z, γ^* $\rightarrow$ μ X), shower muons and hadronic punch-through. At small p$_T$ (<10 GeV), the largest background component is given by muons from π/K decays in flight. At moderate p$_T$ (>10 GeV), the cross-section is dominated by charm and beauty decays, while at larger p$_T$ (>30 GeV), top and Z decays give a sizable contribution.

- **radiation background**: mostly neutrons and photons in the 1 MeV range, produced by secondary interactions in the forward calorimeter, shielding material, the beam pipe and machine elements. Low-energy neutrons, which are an important component of the hadronic absorption process, escape the absorber and produce a gas of low-energy photons through nuclear n-γ processes. This background penetrates the spectrometer from all directions and is no longer correlated in time to the primary p-p interaction. Despite the detection efficiencies for neutrons and photons are very low, the low-energy neutral particle background will dominate the counting rate in most areas of the spectrometer, as it will be shown in next paragraphs.

3.2.1 Response to neutrons

Neutron-induced background hits in drift tubes are due to a large variety of reactions. Neutrons mainly contribute to the photon spectrum via (n,γ) reactions. Thermal neutrons create background hits in the tubes due to β-decay, following neutron capture in the counting gas or in the tube wall. The mean energy deposition from thermal neutron reactions is close to the 14 keV deposited on average by a minimum ionizing particle. At higher energies, charged secondary particles (mainly protons from quasi-elastic neutron scattering in the chamber wall or surrounding material) are the source of the signal.

The detection efficiency for neutrons in the MDT is shown in Fig. 3.1 ([25]). All the effects taken together, out of 1000 neutrons, on average a few are expected to interact in the tubes, depositing an energy of about 14 keV. Figure 3.2 shows the total neutron flux expected in a full ATLAS quadrant, as simulated with the GCALOR-Jan03.

3.2.2 Response to photons

The main photon contribution in MDTs is due to Compton scattering on electrons, in either the counting gas or the tube walls. The mean charge deposited in the counting gas is about twice the charge deposited by a muon. Of 1000 photons, on average 5.5 interact in a single multilayer (three layers high) and 9.1 tubes fire in this multilayer (some of the Compton electrons will deposit energy in multiple tubes). The mean energy deposited in each of this 9.1 tubes is 32 keV, corresponding to about 1235 ionization electrons.

The detection efficiency for photons in the MDT chambers is shown in Fig. 3.3 ([25]). The efficiency below 100 keV is due to photo-electric effect in the gas, while the raising curve in the 1 MeV region is due to Compton scattering. Around 10 MeV, pair production becomes important and interactions in the material surrounding the chamber play an important role. Figure 3.4 shows the total photon flux expected in a full ATLAS quadrant, as simulated with the GCALOR-Jan03.

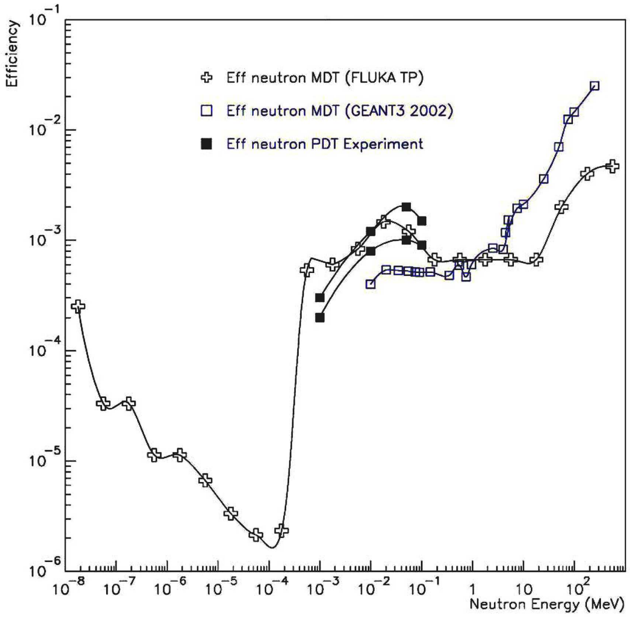

Figure 3.1: MDT detection efficiency for neutrons.

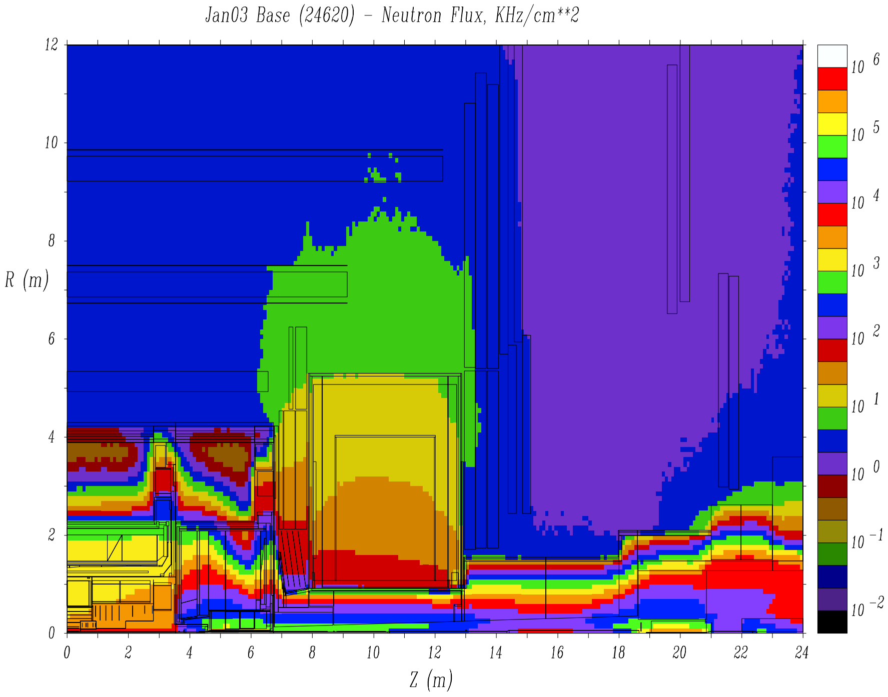

Figure 3.2: Total neutron flux in a full ATLAS quadrant (GCALOR-Jan03).

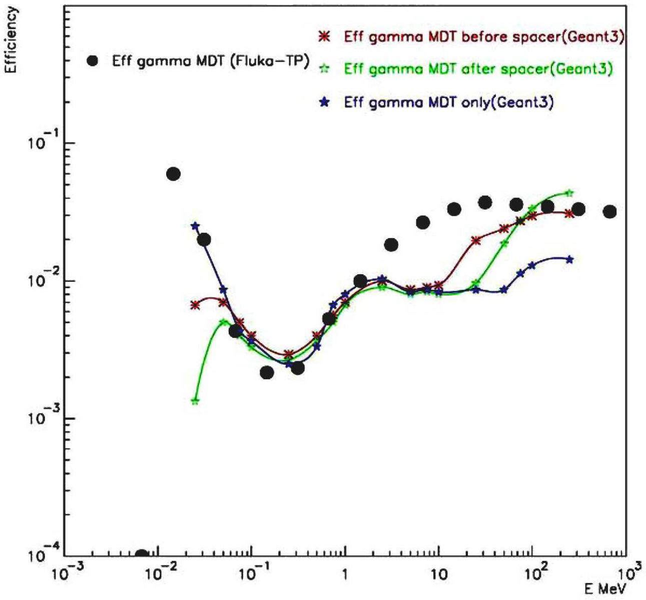

Figure 3.3: MDT detection efficiency for photons.

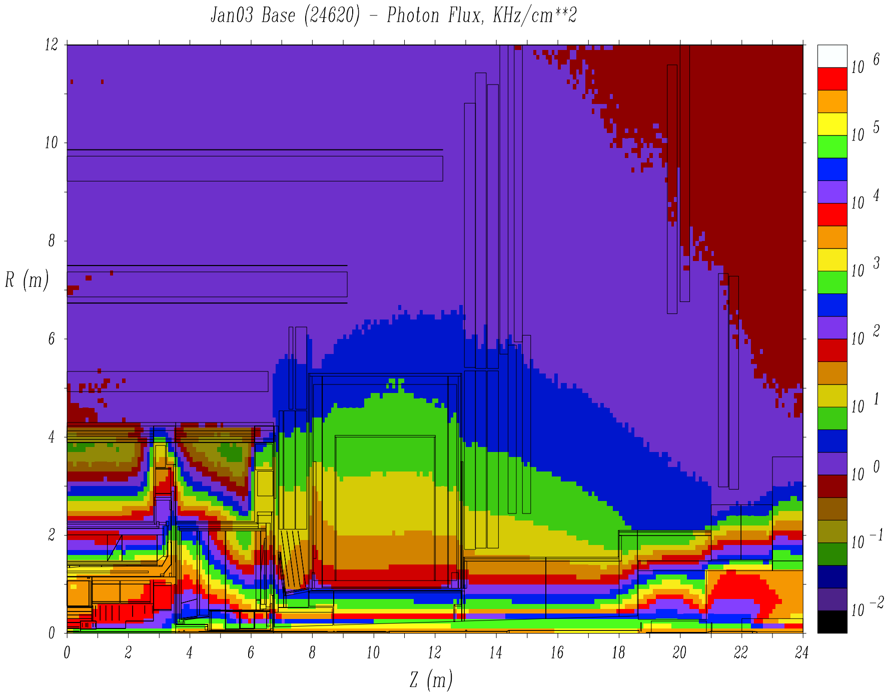

Figure 3.4: Total photon flux in a full ATLAS quadrant (GCALOR-Jan03).

3.3 Test strategy

The high photon and neutron irradiation campaign has started in July 2005. Two small MDT chambers have been exposed to photon irradiation at the *Calliope* gamma facility, in ENEA - Casaccia (Rome) laboratories for two weeks. At the end of the irradiation campaign, a total accumulated charge of 4.8 C/cm, corresponding to the accumulated charge expected in 80 years of ATLAS operation (see Sect. 2.5), was collected on each tube. In September 2005, one of the bundle was moved to the *TAPIRO* neutron reactor area, to complete the high exposure test with neutrons: in particular, two different neutron data set were acquired. First the TAPIRO reactor was operated at low power (50-100 mW), to make drift tubes work at ATLAS-like neutron rates (see Sect. 3.6.2); the week after, TAPIRO was operated at high power, ranging from 100 W to 400 W, to integrate high neutron fluxes (see Sect. 3.6.3).
From the analysis results shown, our Monitored Drift Tubes come out as a very robust detector, capable to “survive” for many years at LHC.

3.4 Experimental set-up

The test detector is composed of two final ATLAS-like MDT chambers (later on called bundles), which were expressly assembled for these high photon and neutron exposure tests at Dipartimento di Fisica - Università della Calabria, in respect of the standard ATLAS wiring and quality control procedure [32]. Each bundle is composed of twenty-four 47 cm long drift tubes, to shape a small standard multilayer [17]; the two multilayers were placed one above the other, as in Fig. 3.5.

3.4.1 The gas system

The test detector was equipped with the ATLAS on-chamber gas distribution system components. The gas inlet and outlet of each bundle were provided by two aluminum manifolds connected to the tubes by stainless steel capillaries of different length. Each capillary supplied gas to three tubes in the same layer connected in series with plastic rings. The employed gas mixture Ar-CO_2 (93%-7%) was supplied from a certified premixed gas bottle at a rate of 3.5 l/h per bundle, corresponding to about 10 complete volume exchanges per day. Pressure and flux were regulated and measured by a pressure controller and a mass flow meter, respectively. The gas tightness was estimated by the pressure drop rate both before and after the irradiation period. The gas leak of both bundles was found to be below the ATLAS standard limit ($2{\cdot}10^{-8}$ bar·l/s per tube).

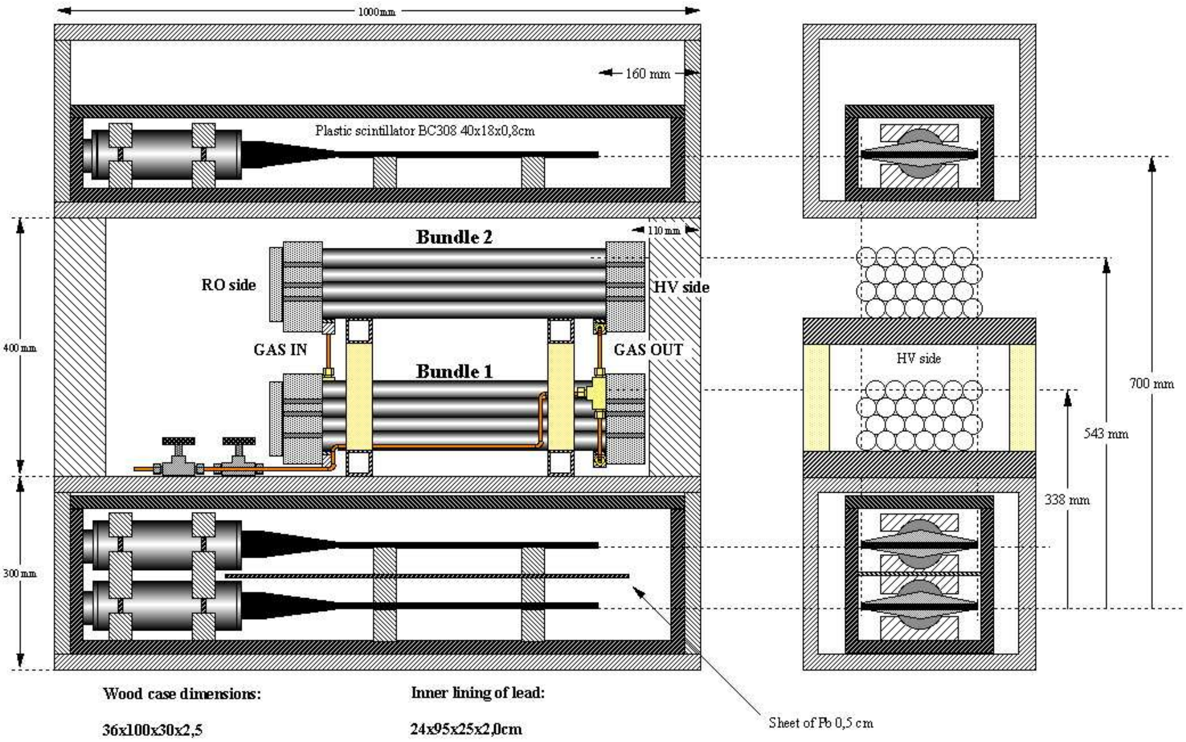

Figure 3.5: "Calliope" test set-up. Side and front view of the set-up showing the two bundles and the scintillator counters in the shielded boxes.

3.4.2 Trigger and data acquisition

In Dipartimento di Fisica - Università Roma TRE, each bundle was provided with the standard ATLAS front-end electronics (see Sect. 2.6.1): an on-chamber mezzanine card connected, in turn, to a CSM0 VME board driven by a crate controller CPU. TDC spectra have been extensively studied, to monitor the drift parameters and the tracking performances; the ADC information, in addition, has been used in the following analysis as a diagnostics for monitoring chamber gas gain.

A coincidence of three scintillator counters was used as a trigger for cosmic rays. The counters were placed into two boxes and completely wrapped with a 2 cm thick layer of lead, two in the box below the test chambers and the other in the one above.

3.5 Test at the *Calliope* gamma facility

3.5.1 The gamma facility

Calliope is a ^{60}Co gamma source. The radioisotope emits two photons of 1.17 MeV and 1.32 MeV; the activity of the source is $6.7{\cdot}10^{14}$ Bq. The Calliope plant offers the possibility to choose the dose rate for sample irradiation and the maximum dose rate is about $5.4{\cdot}10^{3}$ Gy/h. The test detectors were placed at about 3.8 m far from the center of the source, where the measured dose in air resulted to be of 15.3 Gy/h, corresponding to about $7.2{\cdot}10^{8}$ photons/cm^2/s.

3.5.2 Slow control

During the experiment, gas temperature, flow and absolute pressure were continuously recorded. The absolute values of temperature and pressure were known within $\pm$0.2 K and $\pm$3 mbar respectively. Data were corrected off-line for both temperature and atmospheric pressure variations. Figure 3.6 shows temperature distribution for the overall data taking at Calliope. For the last cosmic run at ENEA laboratories, the experimental set-up was moved from the irradiation cell, where temperature was almost constant, to another room. This explains temperature instability in the very last part of the plot. The accumulated charge as a function of the time is shown in Fig. 3.7: source-on and source-off (plateau) runs are clearly visible.

3.5.3 Data taking

The purpose of this experiment was to test both bundles under high photon fluxes, to look for any damages on the drift tubes or any degradation in their tracking performances as the accumulated charge increases (i.e. as the aging process goes on). A first cosmic run was taken in the Dipartimento di Fisica - Università Roma TRE, before moving the experimental set-up to the ENEA laboratories. This “clean” run was used as reference, since no charge was accumulated yet.

Once at the Calliope gamma facility, several runs were acquired. While the ^{60}Co source was switched on, the full trigger system was turned off and no data were acquired. The chambers were operated at 3800 V with standard gas mixture at 1.1 bar, since in standard ATLAS conditions (3080 V and 3 bar), the gas gain

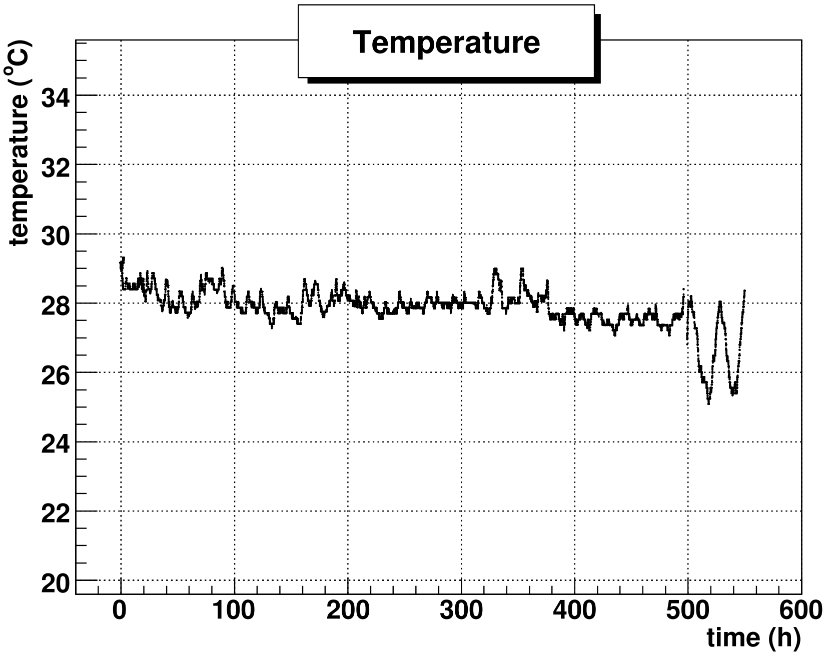

Figure 3.6: Temperature during the whole period.

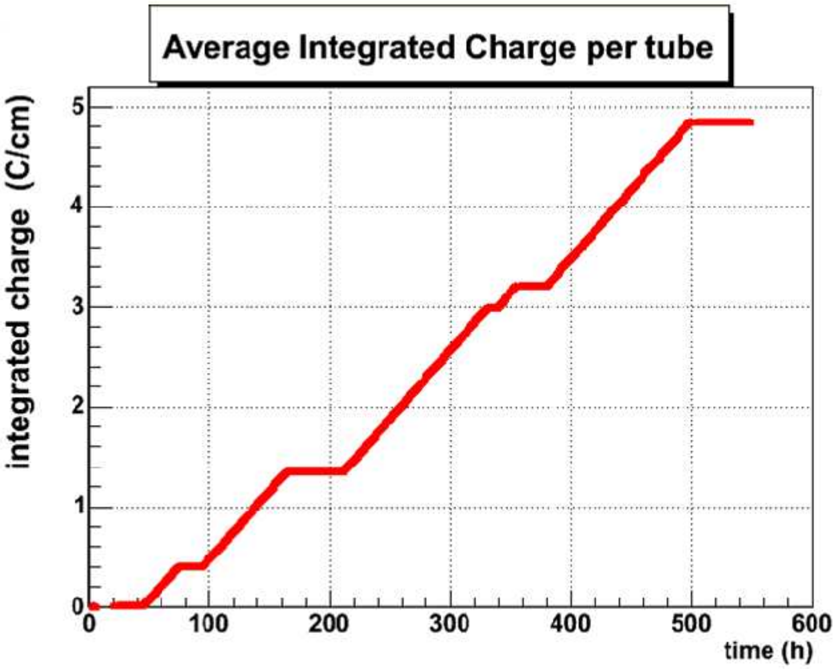

Figure 3.7: Accumulated charge during the whole experiment.

would have been about $2 \cdot 10^2$, a factor one hundred lower that the nominal $2 \cdot 10^4$ (see Sect. 2.6.1). The current drawn by each tube under irradiation could not increase above the measured value of 15 μA because of space-charge accumulation, as described in [34]. By rising the voltage and lowering the pressure, the current drawn by each tube reached 180 μA, resulting in an accumulated charge of 4.8 C/cm/wire at the end of the whole irradiation period.

Between two subsequent irradiations, when the source was off, cosmic ray trigger data were acquired for performance monitoring with MDTs operating in the standard conditions. Two final runs in addition were acquired in Roma TRE, where the read-out electronics was changed. From now on, data taken at the gamma plant and data taken in Rome, will be referred to as *Calliope* and *Roma3* samples respectively. The full run list can be found in Tab. 3.1.

run number		**accumulated charge**	**note**
Roma3 sample	61	0 C/cm	
	168	4.8 C/cm	
	182	4.8 C/cm	changed read-out electronics
Calliope sample	68+69	0 C/cm	
	71	0.8 C/cm	
	74	1.3 C/cm	
	78	3.2 C/cm	
	79	4.8 C/cm	

Table 3.1: List of the runs used in the analysis.

3.5.4 Drift time spectra analysis

In this section the analysis of single tube behavior is presented focusing on noise level and rise time distribution. These quantities are extrapolated from the single tube TDC spectrum, which represents the drift time distribution for electrons produced in the gas volume by ionizing particles crossing the tube.

A typical TDC spectrum for the Calliope test is shown in Fig. 3.8. The leading edge corresponds to hits generated by muons passing very close to the wire, where the electric field is sufficient enough (order of 10^5 V/cm at less than 100 μm from the wire) for the avalanche ion-electron pair production. The trailing edge, instead, is the distribution of drift times measured for tracks passing close to the tube wall.

The descent trend, between both the edges, reproduces the behavior of the non-constant drift velocity: the Ar-CO_2 (93:7) is, as stated in Sect. 2.6.1, a non-linear mixture.

The TDC spectrum is fitted with two ad hoc empirical functions, both for the leading and the trailing edge:

$$f(t) = a(0) + \frac{a(3)}{1 + exp\left(\frac{-t+a(1)}{a(2)}\right)} \tag{3.1}$$

$$g(t) = b(0) + \frac{b(3)}{1 + exp\left(\frac{t-b(1)}{b(2)}\right)} \tag{3.2}$$

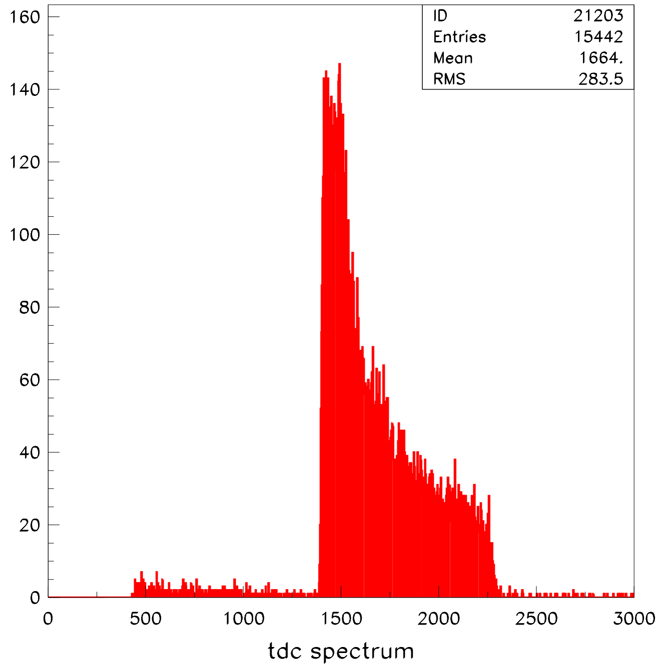

Figure 3.8: TDC spectrum for the reference run.

In particular, a(1) parameter is the so called t_0, which is not a physical quantity, but represents the offset in drift time calculation due to electronics and cabling; a(2) is the rise time (typically 4-6 ns); b(1) is the inflection point t_f of the trailing edge. The difference between t_f and t_0 represents the drift time spectrum width, that is the maximum drift time (t_{max}). It is closely related to the gas mixture and the operating conditions: for standard MDTs, it is about 700 ns.

The data analysis is based on the `CALIB` [35] software package developed for the calibration and performance evaluation of the MDT chambers. It has been extensively used to perform the TDC spectra fit, to calculate the space-time relation, the spatial resolution and the efficiency of the chambers.

Results

From the drift time spectrum, the noise level of a single tube can be directly calculated, by normalizing the number of hits outside the physical time window (from t_0 to t_{max}) to the number of events. Figure 3.9 shows the noise level for all the tubes of test chamber no. 2[1] for two runs of the *Roma3* sample; the open squares refer to the reference run, while full circles refer to last run, where a charge of 4.8 C/cm/wire was accumulated. All the tubes show a higher noise level at the end of the test, but as we have experienced several times in the past, this is simply due to minor differences in the electronics connection and grounding since the set-up has been mounted several times. Two tubes in particular (7 and 19), shows a worse behavior, also visible through the raw TDC spectra inspection in Fig. 3.10 (center) and Fig. 3.10 (right) respectively. Their spectra are completely distorted with respect to a "good" tube (namely tube 9), shown for comparison in Fig. 3.10 (left).

Aging effects can also be revealed through the rise time, since it is closely related to the space resolution. The rise time for all the tubes of test chamber no. 2 is shown in Fig. 3.11a for two runs of the *Roma3* sample. Tubes 7 and 19 do not appear in the run taken after the irradiation campaign, since any fit on their distorted drift time distribution is meaningless. No clear effect of signal degradation can be found for the other tubes. In particular, results for the different runs in the *Calliope* sample are shown in Fig. 3.11b. The rise time shows to be constant as the accumulated charge increases.

Further stability results emerge from ADC spectra study: details on ADC analysis will not be given in this thesis, but can be found in [27] and [37].

---

[1] The global behavior of both chambers is the same. Since test chamber no. 1 was also irradiated with neutrons, as described later, only results for test chamber no. 2 are given in this section.

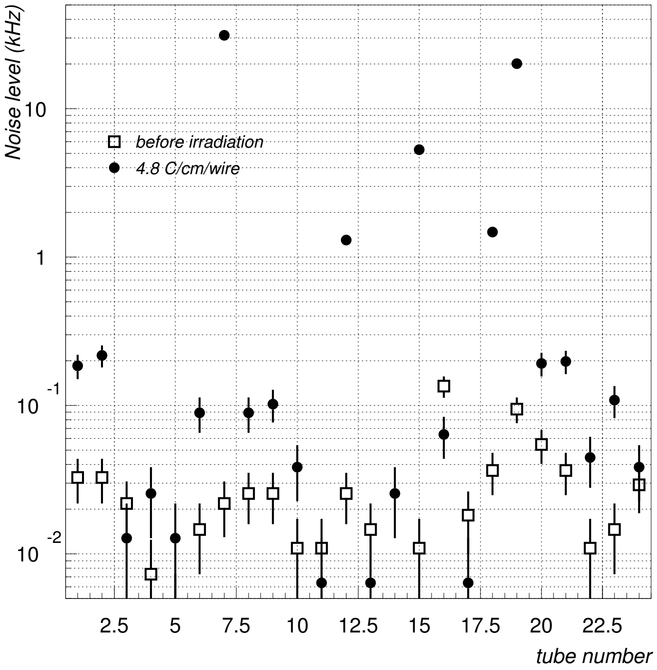

Figure 3.9: Noise level for the tubes of the test chamber no. 2 in the two runs of the *Roma3* sample.

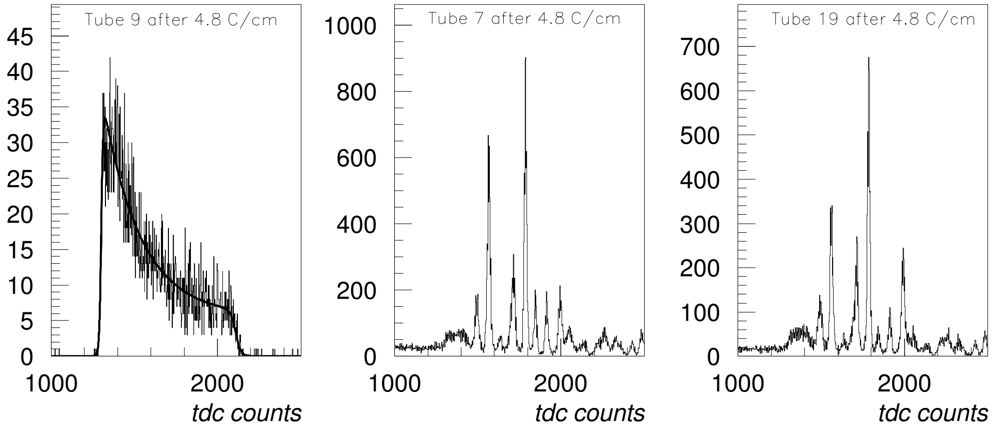

Figure 3.10: Drift time distribution for a good tube (left), and for the bad tubes no. 7 (center) and no. 19 (right).

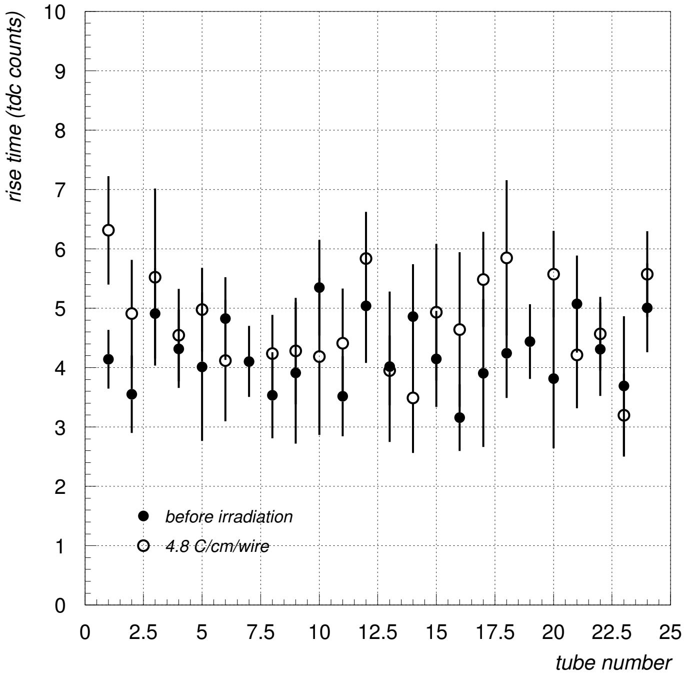

(a) *Roma3* sample

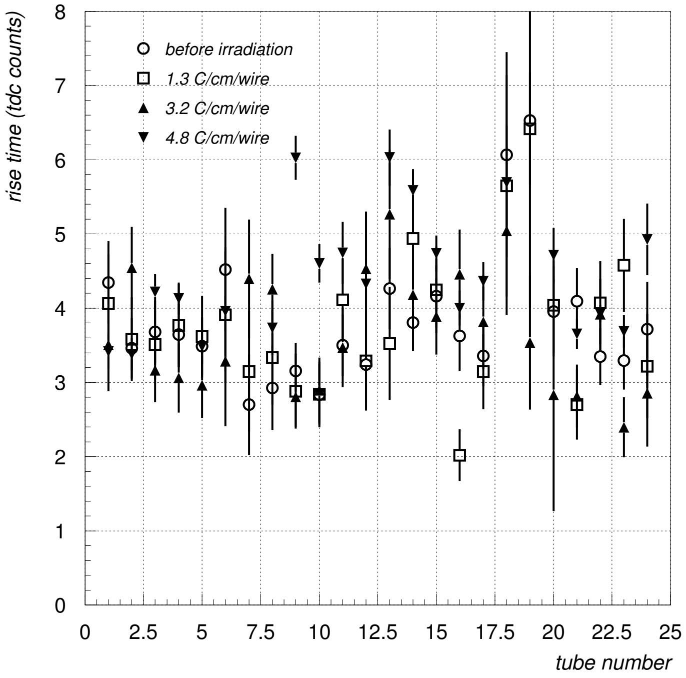

(b) *Calliope* sample

Figure 3.11: Rise time for the tubes of the test chamber no. 2 in the runs of the *Roma3* sample (a) and *Calliope* sample (b).

3.5.5 Space-time relation

An accurate knowledge of the relation between the measured drift time and the distance of the minimum approach of the particle trajectory to the wire, called drift distance, is necessary to perform the track fit. This space-time relation is referred to as *R-T*. Once measured times assign drift circles, the iterative *autocalibration* procedure [35] is responsible for extrapolating tracks through MDT chambers. If two R-T relations are different, two different drift radii are associated with the same measured drift time: of course, this directly reflects on pattern recognition and tracking. For this reason, the dependence of R-T relation on accumulated charge has been investigated. A R-T relation has been calculated for each single run of the Calliope sample; because of the R-T dependence on gas, temperature and composition, only data with temperature spread within 1.5 °C and pressure variation within few mbar have been analyzed. All the R-Ts have been normalized to the same temperature of 28 °C, applying appropriate corrections as described in [36] and [38] and then compared with reference data taken before irradiation.
Figure 3.12 shows the differences[2] between the R-T computed for the reference run and the R-T computed for each other run. A small increase of the difference between the R-Ts with increasing accumulated charge is visible. It is less than 100 μm for large radii even after the total accumulated charge of 4.8 C/cm/wire. Such a variation is corrected in the standard calibration of the R-T relations: calibrations have to be performed regularly to take into account environmental parameter variations that can give effect of the same size.

3.5.6 Tube efficiency

Some indication of MDT performance degradation can be found by measuring single tube efficiency, which can be defined as follows. *Hit efficiency* is the probability to register a hit for a muon track crossing the tube, irrespective of the measured drift time; it is expected to be close to 100%. For a four layer multilayer, *N-sigma* efficiency is calculated by reconstructing tracks with at least three hits on tubes different from the one under observation; a drift radius *r* is extrapolated on that tube and compared to the radius obtained from time measurement r_{drift}. The dif-

---

[2] Differences between two different radii, calculated for two different runs, at the same drift time.

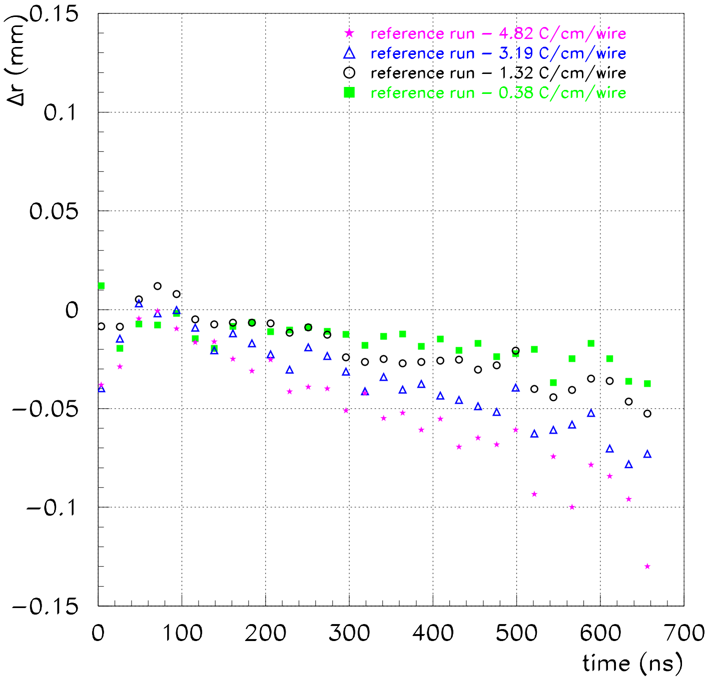

Figure 3.12: Comparison between the R-Ts for different runs with respect to reference data.

ference between them is called *residual*. “Good” hits occur when residuals are lower than *N* times the single tube resolution. *N-sigma* efficiency is then computed as the ratio between the number of good hits and the number of tracks that crossed the tube.

An optimal calculation of the *N-sigma efficiency* cannot be achieved with the present set-up: the imperfect grounding caused a slightly high noise level in some tubes. Furthermore, for some angular configurations, the determination of the track parameters with only three drift circles suffers an ambiguity that can affect the track extrapolation to the last tube. The best way to compute efficiency in the MDT chamber is to use the whole chamber, i.e. two multilayers, but this was not possible because the two bundles were not sufficiently aligned. These effects are taken into account by normalizing the efficiency to the *hit efficiency*.

The efficiency for all the tubes of the chamber no. 2 is shown in Fig. 3.13a for the five different cosmic runs. Again, the bad behavior of tubes 7 and 19 emerges after the last irradiation period, where their *hit efficiency* suddenly drops to less than

0.5. Anyway, for all the other tubes, efficiency proved to be constant with respect to the accumulated charge, as is shown in Fig. 3.13b: some tubes on each layer have been chosen as an example. Efficiency for tubes 7 and 19 has been evaluated for two runs of the *Roma3* sample after the irradiation campaign. Once the read-out electronics was changed, the *hit efficiency* rises back to the initial value of 0.98±0.01 for tube 7 and to 0.95±0.02 for tube 19. Since no damage on the wires has been observed, as it will be explained in Sect. 3.7, this suggests that part of the read-out electronics, rather than tubes, suffered a damage during irradiation.

3.6 Test at *TAPIRO* reactor

After the photon irradiation campaign, bundle no. 1 (see Fig. 3.14) was moved to the TAPIRO reactor experimental area, to continue the test with high neutron fluxes. The same read-out electronics was used, since no anomalies were found for this chamber. The trigger system neutron shielding was improved by covering scintillators with cadmium sheets and boron powder. The gas mixture was continuously flushed at a rate of 6 N l/h, corresponding to about 6 volume changes per day. The accuracy on the gas composition was estimated to be better than 0.1%. The absolute gas pressure (3 bar) and temperature were regularly measured with an accuracy of 1 mbar and 0.4 °C respectively. During the whole irradiation test, the temperature ranged between 22.8-23.7 °C; for such variation, no corrections have been applied for the evaluation of the gas gain and drift properties. The high voltage, supplied by a CAEN 2527 system, was kept constant to 3080±2 V, corresponding to a gas gain of $2 \cdot 10^4$ (ATLAS standard operating point). The current drawn by each layer of tubes was also measured with a resolution of 10 nA.

3.6.1 The neutron source

The TAPIRO source is a fast nuclear reactor at ENEA-Casaccia [39]. Its core is an U-Mo alloy (98.5%:1.5%), with fully enriched ^{235}U at 93.5%. The neutron flux at the core center is $4 \cdot 10^{12}$ Hz/cm^2 at the maximum thermal power (5 kW). The test chamber was located inside an epithermal column[3] (see Fig. 3.15) where fast neutrons produced in the fission reactions are moderated towards epithermal energies.

---

[3] During last years the reactor has been mainly used for research of interest for BNCT (Boron Neutron Capture Therapy) and for this aim both a thermal and an epithermal column were built [40].

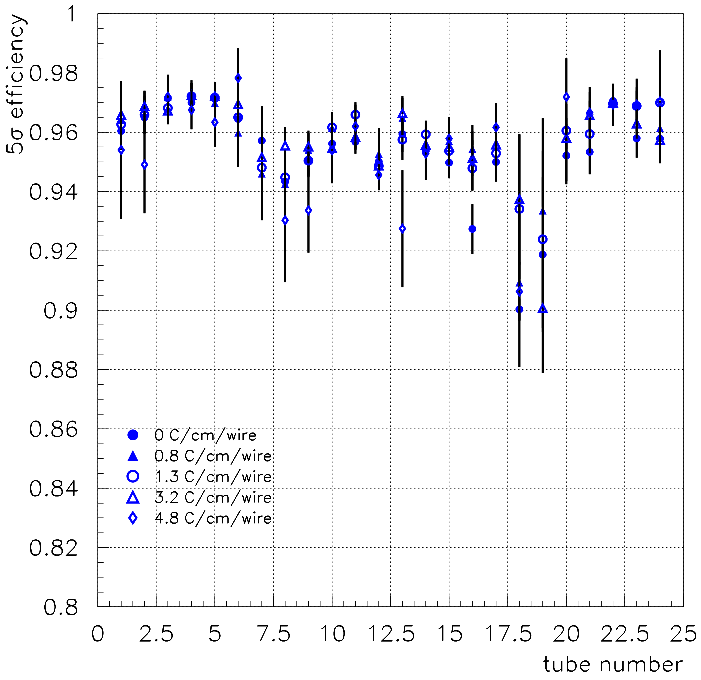

(a) all tubes

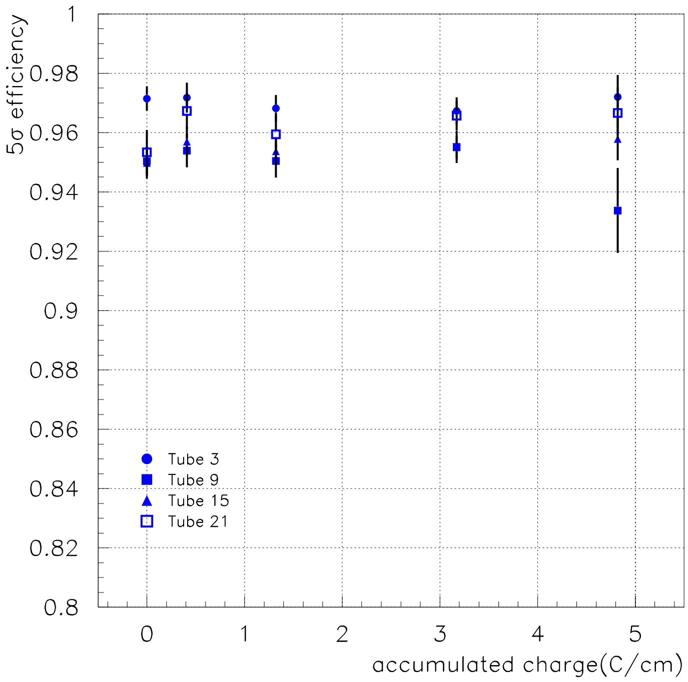

(b) versus charge

Figure 3.13: Efficiency of test chamber no. 2 for all the tubes in the five cosmic runs (a), and for four central tubes (one for each layer) versus accumulated charge (b).

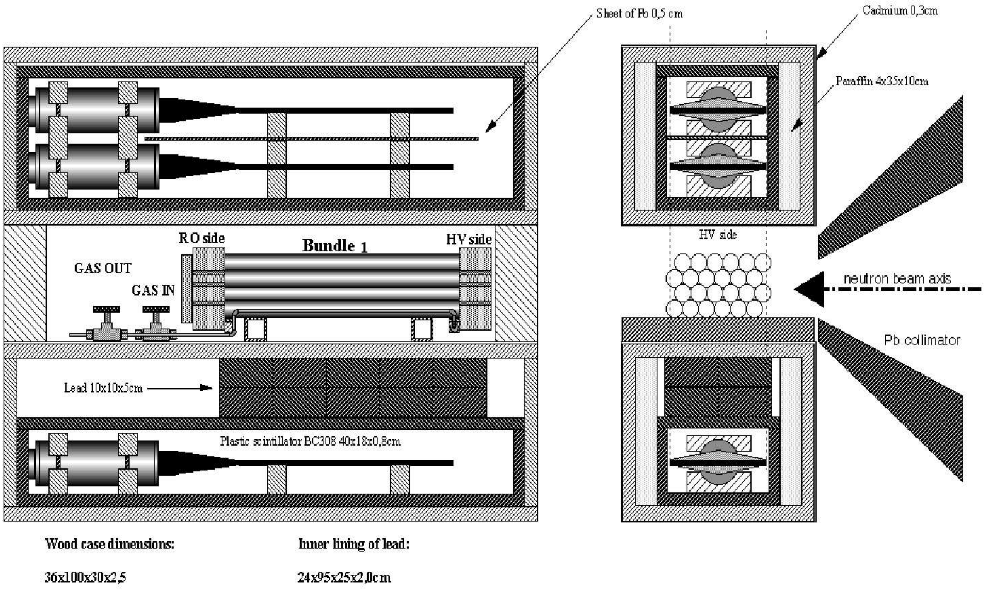

Figure 3.14: "TAPIRO" test set-up. Side and front view of the set-up showing bundle no. 1 and the scintillator counters in the shielded boxes.

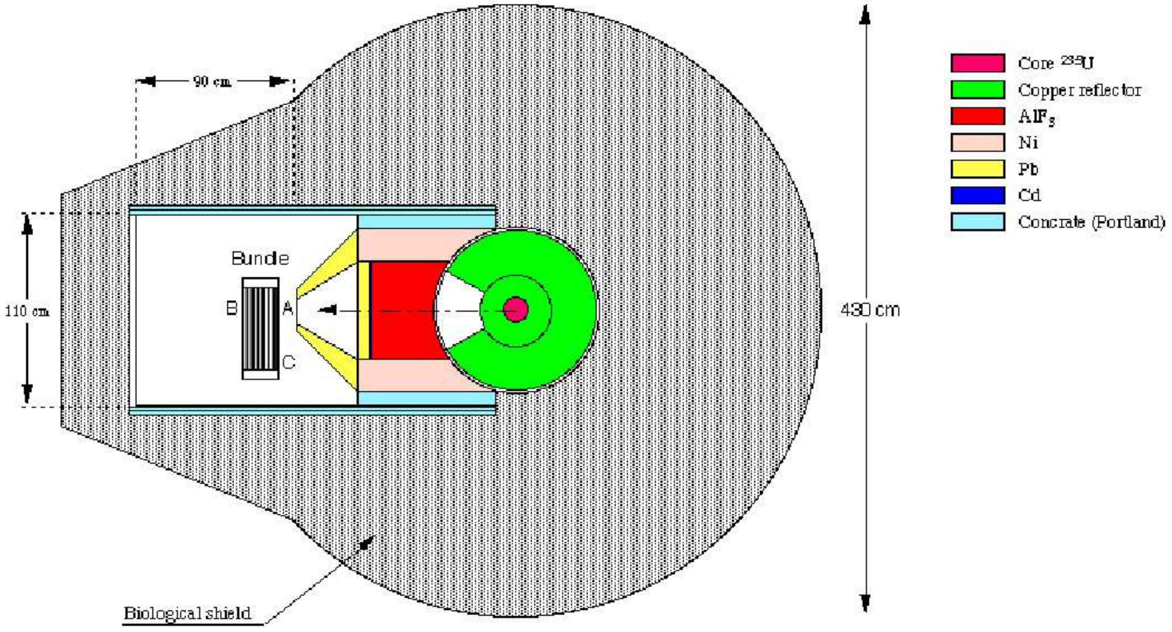

Figure 3.15: Sketch of the TAPIRO facility plant: the reactor core, the epithermal column and the test detector are visible.

The neutron energy spectrum [40] at the collimator exit is reported in Fig. 3.16, where the expected neutron energy spectrum in the ATLAS muon spectrometer barrel region is shown for comparison.

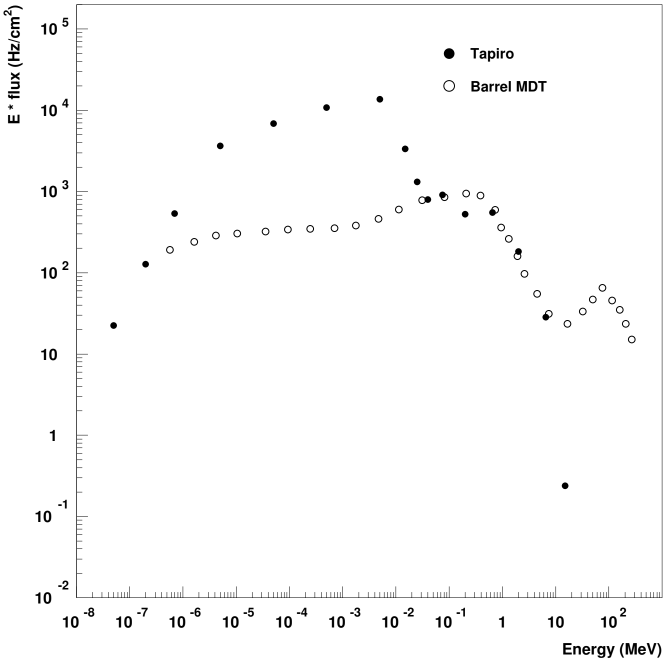

Figure 3.16: Neutron energy spectrum at the collimator exit with reactor power at 50 mW; the expected neutron spectrum in the ATLAS muon spectrometer barrel region is also shown for comparison.

Since neutron intensity decreases both with the angle spread and with the distance from collimator, measurements of the neutron flux were made in three points (A, B and C) at the external surface of the test chamber, as shown in Fig. 3.15. Both bare and cadmium shielded gold foils were put along the beam axis in front of the collimator for the first tube (A) and for the last one (B) and, facing the collimator, at the farthest end of the chamber (C). The chamber was located 10 cm far from the collimator exit with wires orthogonal to the beam direction. Neutron measured fluxes are reported in Tab. 3.2; an average value of $7.9{\cdot}10^4$ Hz/cm^2/W was estimated for the whole test.

The TAPIRO facility is also a double photon (~1 MeV) background source: gammas coming from the beam line, associated with the nuclear reactions into the core, and gammas from the surrounding material due to neutron absorption. This latter component is relevant for the cosmic ray runs, where performances of the chamber are measured, since the mean life of these excited nuclei is quite long (about 10 hours) compared with the run duration (typically 15 hours).

	neutron flux (Hz/cm^2)	
position	**Cd cover**	**no Cd cover**
A	$2.23 \cdot 10^7$	$2.57 \cdot 10^7$
B	$1.07 \cdot 10^7$	$1.10 \cdot 10^7$
C	$0.92 \cdot 10^7$	$1.06 \cdot 10^7$

Table 3.2: Measurements of the neutron flux, with reactor thermal power at 200 W, for three points on the external surface of the test chamber. Both cadmium shielded and bare gold foils were used.

3.6.2 Performance studies at ATLAS-like environment

Before starting the neutron irradiation, a run with cosmic ray trigger was taken and used as reference. Then a dedicated sample was acquired, to study tracking performances on MDTs operating at an ATLAS-like environment. Runs of about 6-8 hours with the reactor on and operating at a thermal power of 50 mW and 100 mW, were taken day by day; between two subsequent irradiations, when the reactor was off and the experimental area closed, data with cosmic rays were used as intermediate references to monitor any alteration in MDT behavior. This tracking sample will be referred to as TRA sample as summarized in Tab. 3.3.

run number		**reactor power (mW)**	**neutron flux (Hz/cm^2)**
reference	86	0	0
TRA	89	50	$4 \cdot 10^3$
	90	0	0
	91	50	$4 \cdot 10^3$
	92	0	0
	93	50	$4 \cdot 10^3$
	95	100	$8 \cdot 10^3$

Table 3.3: List of runs for the tracking sample: the reactor thermal power and the neutron flux are also reported.

Analysis results

The three sub-sets of data (reactor-off, reactor at 50 mW and 100 mW) show different distributions of hit multiplicity, defined as the number of hit per each event; these distributions are reported in Fig. 3.17. They are normalized to 1 for comparison, as the run duration was different. Fig. 3.17a shows the distribution of all recorded hits, while Fig. 3.17b and Fig. 3.17c report only hits whose drift time fall inside (between t_0 and t_{max}) and outside the physical time window respectively. Figure 3.17b shows that the peak with four hits, that is what is expected for clean tracks, is less visible as the reactor power is increased; this is also due to a relative increase of events with few hits (from 0 to 3) caused by fake triggers because of not perfect shielding, and by off-time hits occurred in the same tube, which mask the true physical ones. Figure 3.17c, where there is not contribution from cosmic tracks but only off-time hits are used, shows that the chamber occupancy (events with more than 20 hits) increases with reactor power, since the environment is of course “dirtier”.

The importance of monitoring R-T relations has already been discussed for the gamma irradiation test (see Sect. 3.5.5). Following the same strategy, a R-T has been calculated for each run and compared to the R-T of the reference run 86. As it can be seen in Fig. 3.18, no systematic effects are visible: R-T differences for ATLAS-like fluxes are within the acceptable value of $\pm 25\mu$m, where two R-Ts are considered the same.

The tracking efficiency, defined as in Sect. 3.5.6, is shown for two tubes chosen as example in Fig. 3.19. It is stable around 0.97 ± 0.01 through the whole set of low power runs.

3.6.3 Performance studies at high neutron flux

Another aim of the test was to study the MDT chamber robustness after intensive irradiation with high neutron fluxes. This goal has been achieved by exposing the detector day-time for about 6-8 hours to intensive neutron fluxes with TAPIRO reactor operating in a range of thermal power between 100 W and 400 W. At the end

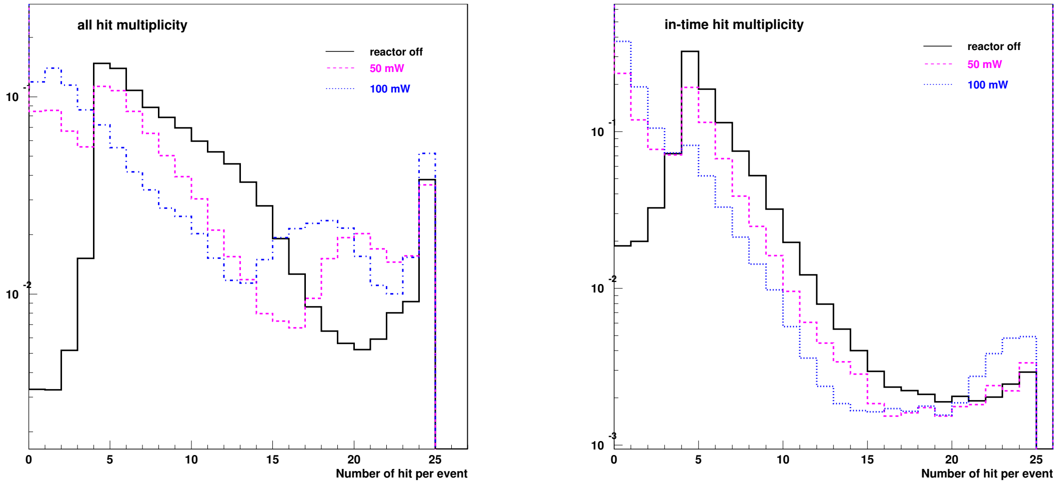

(a) all hits

(b) in-time hits

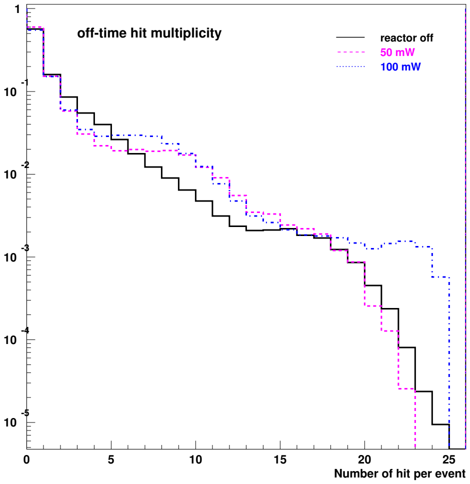

(c) off-time hits

Figure 3.17: Hit distribution per event for all the hits (a), in-time hits (b), off-time hits (c).

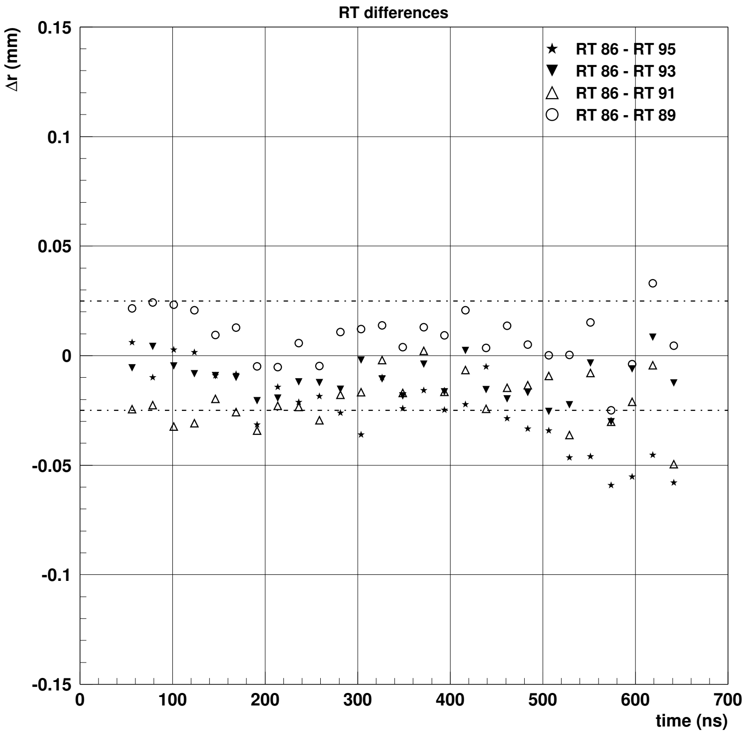

Figure 3.18: RT relations differences with respect to the reference run (86).

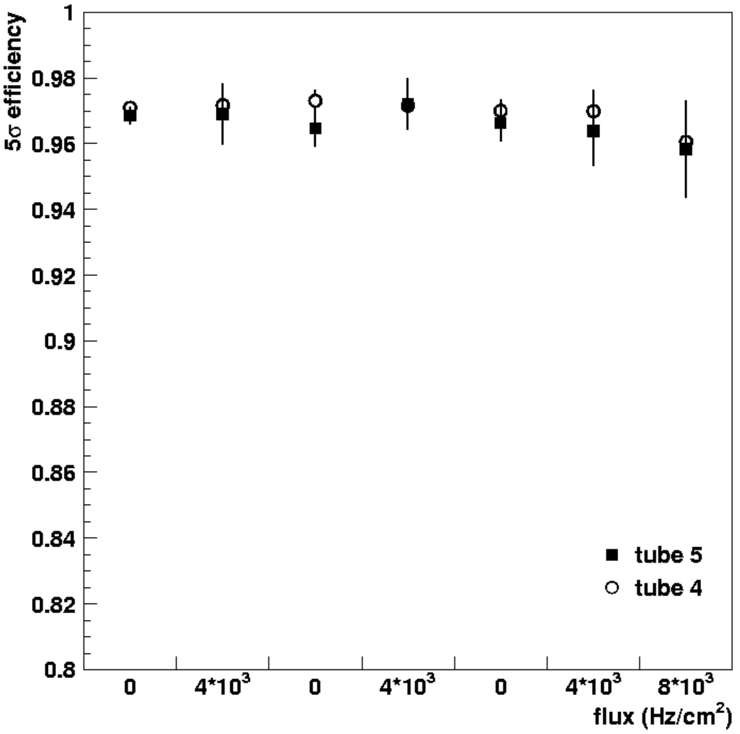

Figure 3.19: Single tube efficiency for three different flux values.

of the test an amount of $1.38 \cdot 10^{12}$ neutrons/cm^2 has been integrated. During irradiation, the trigger was switched off and no data were registered. Currents drawn by the tubes were constantly monitored: they ranged from about 5 μA to 8 μA per tube. Cosmic rays were acquired in runs of about 15 hours by switching on scintillators while the reactor was off. This tracking sample will be referred to as IRR sample as summarized in Tab. 3.4.

run number		integrated flux (neutrons/cm^2)	ATLAS years
reference	86	0	0
IRR	98	$1.39 \cdot 10^{11}$	4
	99	$4.08 \cdot 10^{11}$	12
	100	$7.66 \cdot 10^{11}$	22
	113	$1.38 \cdot 10^{12}$	40

Table 3.4: List of runs for the high irradiation sample with the integrated neutron flux and the correspondence in ATLAS years of operation.

Since it is expected tubes operating in the same conditions have the same space-time relation, R-Ts have been calculated for each run of the IRR sample. Each of them has then been compared to the R-T of the reference run (86): differences between R-Ts, shown in Fig. 3.20, range between ± 25 μm.

Efficiency has been computed following the procedure described in Sect. 3.5.6 for all the run of the IRR sample and results are shown in Fig. 3.21. Here, again, a constant value around 0.97 has been found.

3.7 Wire analysis

After the irradiation campaign, seven anode wires were extracted[4] from their drift tubes and analyzed by Scanning Electron Microscopy and Energy Dispersive X-ray techniques at CERN. The aim of the wire surface examination was to reveal some pollution and to analyze, in case, their composition. From previous aging tests ([42], [43] and [44]) it is known that pure Ar-CO$_2$ (93%:7%) doesn't show any evidence of aging up to an accumulated charge of 2 C/cm. Nevertheless some aging effects can appear if the gas is polluted with sealing material used for valves, or with chemicals that enter the drift tube by outgasing of components that are

---

[4] A detailed description of the technique to extract the anode wire is given in [41].

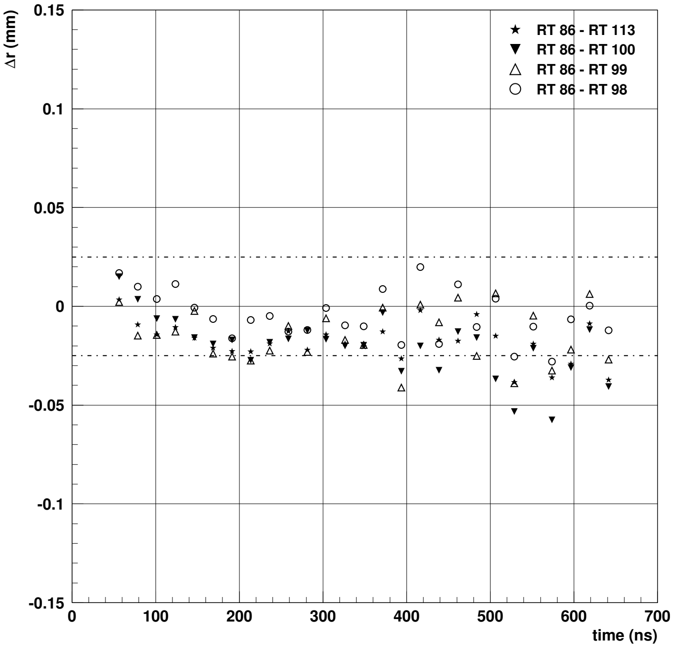

Figure 3.20: R-T relation differences with respect to reference run.

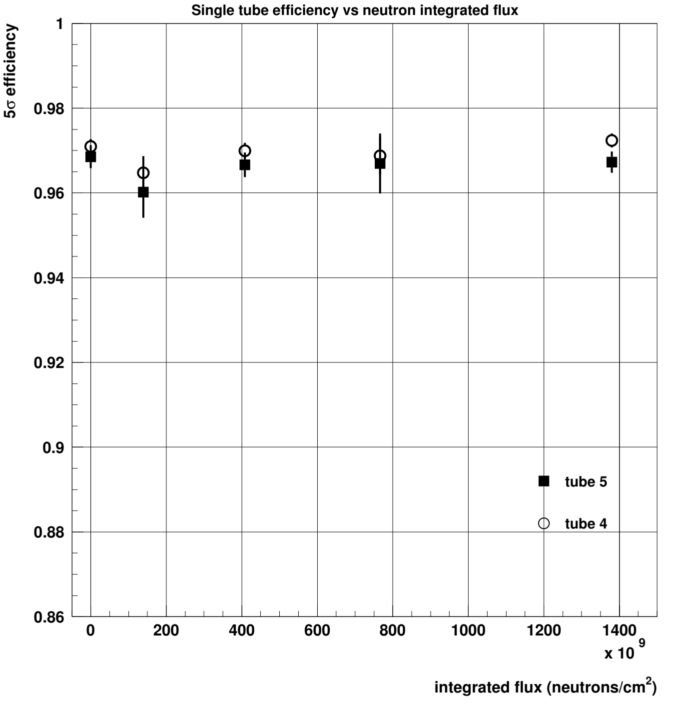

Figure 3.21: Efficiency as a function of the neutron integrated flux.

in contact with the gas system (e.g. cleaning agent). As shown in Fig. 3.22, three wires were extracted from test chamber no. 2, the one which was exposed to photon irradiation only. In particular, if tubes are numbered from right to left and from bottom to top, wires were extracted from tubes no. 3, 10 and 19 (the one that showed the worst response). Other four wires, no. 3, 9, 13 and 20 belonging to four different layers, were extracted from test chamber no. 1, which was exposed also to neutron intensive fluxes.

Since the on-chamber gas distribution is serial-parallel (three tubes series), the wires were chosen in order to have at least one tube for each position in the gas series. Each extracted wire was divided in three samples 4 cm long: one at 2 cm from the beginning of the wire (gas inlet side), one in the middle and one at 2 cm from the end of the wire (gas outlet side). Each sample was analyzed and no deposits on the wire surface have been observed. They were also compared to three reference samples, 4 cm long each, taken from the same wire spool used to assemble the test chamber tubes. The irradiated wires show no sensible variation with respect to the reference spool: the surface is everywhere clean, except some black spots (C-O-Si-Al-Ca) and white particles (Al-Cl-F). Figure 3.23 shows two micro-photos as examples of a virgin wire and an irradiated one.

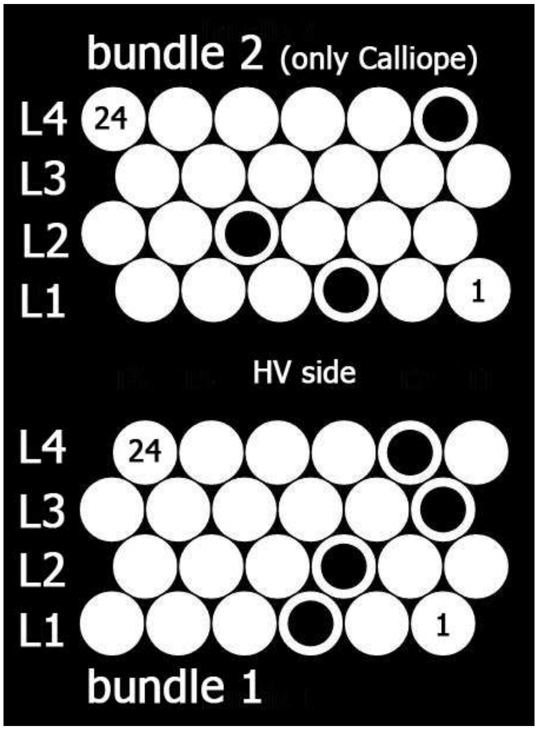

Figure 3.22: Extracted wires for SEM & EDX analysis from both bundles.

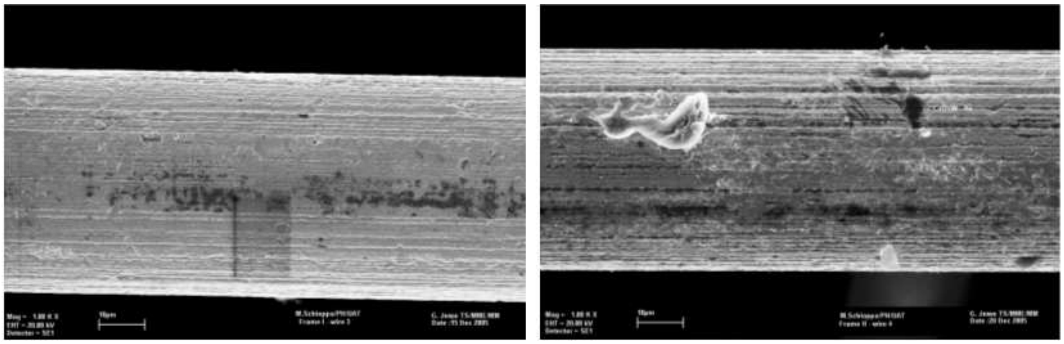

Figure 3.23: Micro-photo of a virgin wire (left) and wire 3 on test chamber no. 1 (right).

3.8 Summary

Intensive photon and neutron irradiation tests have been performed on final MDT-like test chambers. The main purpose was to test chamber robustness at ATLAS rates and after massive photon and neutron fluxes, in view of the foreseen upgrade at Super-LHC. After a full accumulated charge of 4.8 C/cm per tube, corresponding to 80 years of LHC operation, and a neutron flux of $1.38{\cdot}10^{12}$ neutrons/cm^2, corresponding to further 40 years, a good behavior of both chambers is observed.

- The pressure drop rate before and after the irradiation campaign was measured and it turned out to be constant ($1{\cdot}10^{-8}$bar·l/s, lower than ATLAS requirements). This implies a stable behavior of "o"-rings, end-plugs and all the different gas distribution elements.

- Two tubes, subject to photon irradiation only, showed a distorted drift time spectrum and a sudden drop in efficiency. The hit efficiency improved by changing the read-out electronics in Roma TRE laboratories, suggesting a damage to some electronic component. It has to be underlined here that the ASD and the TDC chip were already tested under irradiation ([45] and [46]) and proved to tolerate an irradiation equivalent to 10 years of LHC operation. However, in this test the irradiation was much higher than in earlier studies: all the other electronic components showed a stable behavior after the complete (photons+neutrons) test.

- No significant gain drop is observed looking at the measured charge deposit ([28] and [37]) and negligible variations of the drift properties result from drift time spectra and space-time relation studies for all the tubes of two bundles. The single tube efficiency remains constant with increasing accumulated charge.

- The SEM/EDX analysis shows no evidences of deposits or damages on the surfaces of the wires.

Chapter 4

The MDT libraries for the GNAM monitoring project

4.1 Introduction

During the last few years, much effort was put in carrying out test beam sessions, in order to assess the performances of each ATLAS detector. Given the complexity of the apparatus being tested, the on-line monitoring systems played an essential role. They revealed to be very helpful in setting up the correct running conditions and assessing the data quality.

On-line monitoring is fundamental now too, as the various detectors are being commissioned, and will be essential during the real data taking, especially in the initial phase, when both LHC and ATLAS will need a lot of tuning to reach a stable condition. It is well known that the whole ATLAS detector consists of about 140 million electronic channels. LHC will provide collisions at a center of mass energy of 14 TeV, with a frequency of 40 MHz and the output of the first level trigger will be less than 75 kHz. This frequency will be further reduced by higher trigger levels and finally some hundreds of events will be selected and stored every second. The challenging experimental environment and the extreme detector complexity impose the necessity of a common scalable distributed monitoring framework, which can be tuned for the optimal use by different ATLAS detectors at the various levels of the ATLAS data flow.

For these purposes, from the strong collaboration of Cosenza (MDT), Pavia (MDT), Pisa (Tile) and Napoli (RPC) groups, the GNAM project [47] is born in January 2004. I joined the group since the beginning of my PhD, in November 2004 and participated actively in the design and development of the MDT detector specific libraries, following the request of the wide ATLAS Muon Spectrometer community. In this chapter I will give an overview on the GNAM project in the TDAQ framework. Then I will focus on my activity, as developer of the MDTGnam plug-ins for the barrel and end-cap commissioning.

4.2 Data acquisition in ATLAS

The schema of data flow in ATLAS is shown in Fig. 4.1.

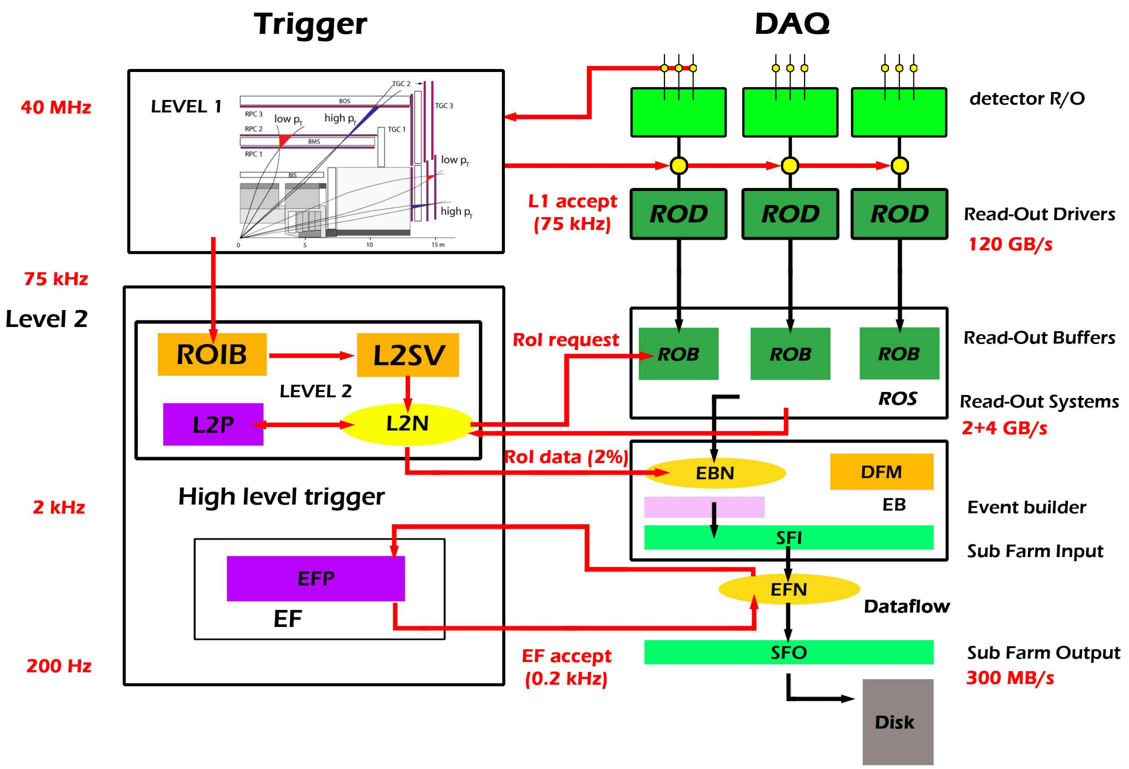

Figure 4.1: Schematic view of data flow and trigger levels in ATLAS.

The definition of the data flow levels is tightly related to the working model of the trigger system, reported in Sect. 2.7.

LHC will provide collisions with a frequency of 40 MHz. Data will be read by the front-end electronics (FE) and used for the first level trigger decision. If the event looks "interesting", the data are forwarded to the Read Out Drivers (RODs) to be put together to form a "fragment". Fragments are promptly sent to the Read Out Buffers (ROBs) via optical link. The expected rate of events passing the first selection is about 75 kHz, with an average size of 1 kB for the fragments sent by each of the 1600 RODs foreseen in ATLAS.

The ROD is the last acquisition level that depends strictly on the detector, and its deployment is responsibility of the detector communities. From the ROB level up, the data acquisition and selection is completely handled by the ATLAS Trigger and Data Acquisition group (TDAQ).

All the information stored in the ROBs is available for the second decision, but only a small fraction is actually used: the first level trigger, indeed, gives hints about the so called Region of Interest (RoI), so that only the relevant data are transported through the network. The second level trigger refines the event selection, and takes the rate down to few kHz.

Up to 18 ROBs can reside on the same PC, where a Read Out System (ROS) will run, too. If the event is accepted by the second level trigger, then the data are collected from the ROBs by the ROSes and sent to the Sub Farm Input (SFI) for the complete event to be built. Now the final event selection is performed, using the highest level algorithms from the off-line framework, and the accepted events are stored on tape.

The whole trigger system is designed to keep the final rate at about 200 events being saved every second, thus requiring a bandwidth of nearly 300 MB/s, both on the network and in the mass storage hardware system.

4.3 The GNAM project

The development and deployment of the basic monitoring services have always been responsibility of the TDAQ group. Up to the 2003 test beam, the different detectors acquired data independently of one another, and each community developed its own monitoring application, exploiting the central services.

During summer 2004, in the Combined Test Beam (CTB), an entire slice of the ATLAS detector was exposed to the beam. A unified data acquisition was experienced, with the main purpose to test the overall DAQ structure and the integration level among the software components developed by the different communities. It was for the CTB that the first request came about a low-level on-line monitoring framework, that would be general enough to be adapted to every detector, and would provide a unified interface for checking the whole experiment.

An *Athena* [48] based monitoring tool was already present, but this high-level monitoring runs off-line on the full reconstructed events. If some subdetector, or just some channel, is not working properly, it will not be identified as data are being acquired, but only at the end of the run, after some hours, for example. Some problems, instead, need to be spotted as soon as possible; as an example, if a channel is particularly noisy, it keeps the data acquisition busy and "good" data on "good" channel can be lost.

The GNAM low-level monitoring can run on-line at all the levels (starting from ROD) and is devoted to check the hardware conditions (dead/noisy channels, electronic mappings, ...) to ensure the correct functioning of the various detectors. ROD/ROS levels are the natural place for this kind of monitoring, since basic information on the detector status doesn't need correlation with the other ones.

The *Athena* monitoring is indeed an essential tool for the data assessment, since it checks physics related quantities, such as momentum spectra, invariant masses and so on. Figure 4.2 shows where both monitoring tools are foreseen in ATLAS.

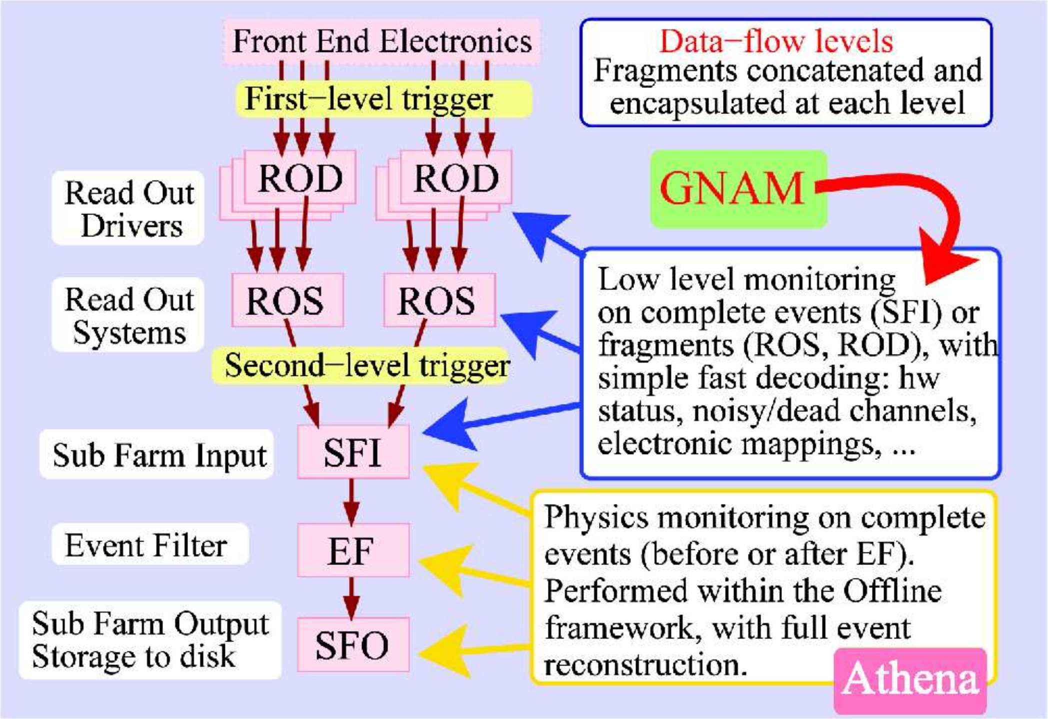

Figure 4.2: GNAM and Athena monitoring tools act at different TDAQ levels.

4.3.1 Requirements and structure

An on-line monitoring framework should fulfill the following requirements:

Detector independent. Its architecture should be detector independent: processing a fragment should rely only on its structure, and not on its content.

Modularity. It should be modular, in order to keep common actions separated from detector specific ones. Common actions are, for example, interacting with the TDAQ system, unpacking the sampled fragments (breaking them into ROD fragments) and managing the histograms (having them displayed, respond to commands). Detector specific actions include data decoding (understanding the physics contents), histogram booking and filling.

Integration with DAQ. The monitoring system should be able to run automatically, controlled by the overall DAQ system;

Archiving. Furthermore, monitoring information (mainly histograms) should be collected and stored whenever needed, whether or not there is actually anybody checking it on-line.

For these purposes two parallel independent applications have been developed by the same collaboration: GNAM (**G**NAM is **N**ot **A**tl**M**on[1]), a framework for low-level on-line monitoring, having sampled events as input and user-defined histograms as output, and OHP (**O**n-line **H**istogram **P**resenter), a general purpose presenter for on-line monitoring histogram visualization.
Later on, since my activity was devoted to the development of GNAM plug-ins for the MDTs, only details on the GNAM monitoring chain will be given. Further information on the OHP project can be found at [49].

4.3.2 GNAM monitoring chain

As shown in Fig. 4.3, GNAM is divided into two parts: the Core and the detector plug-ins. The Core handles the common actions, while detector specific code is implemented in the plug-ins.

---

[1] When this project was started, the most natural name was AtlMon; as it was already used by a completely different application, it was turned to this recursive acronym, in pure GNU-like style.

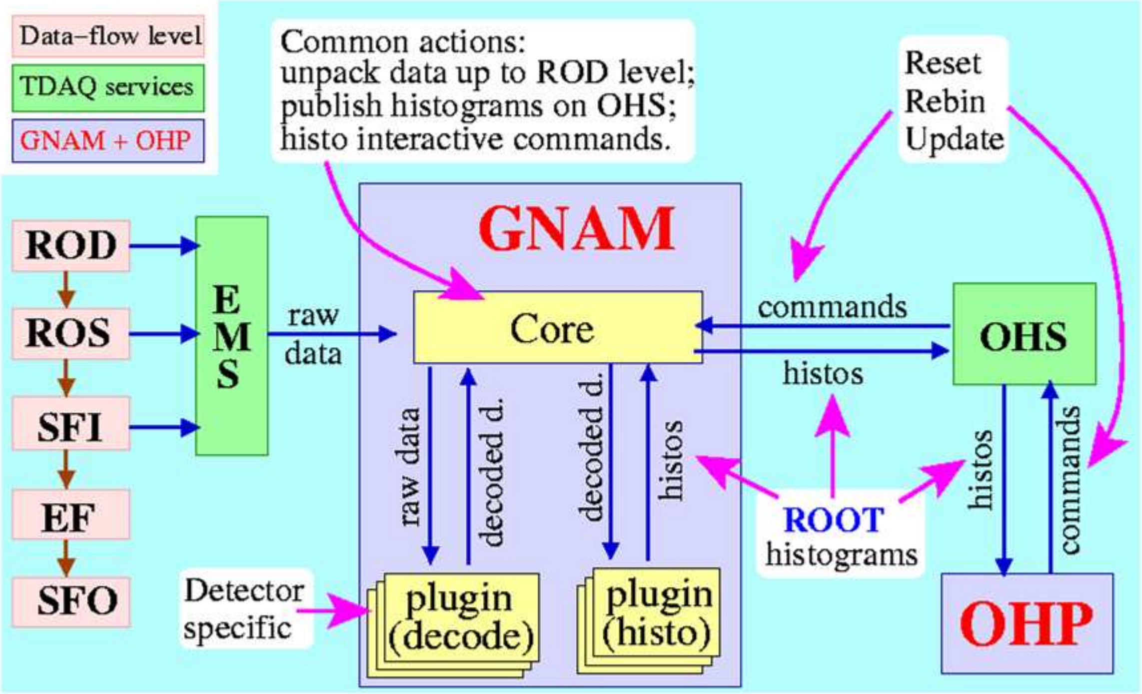

Figure 4.3: Schema of the GNAM monitoring chain.

The Core is responsible for getting events from one of the samplers, which can provide event fragments at ROD, ROS or SFI level: a ROS or SFI-level fragment is a sequence of ROD-level fragments interleaved with higher-level headers (see ATLAS raw data format structure at [50]). The Core can understand this structure and extract the single ROD fragments from the blob, but it cannot go further because there is no standard format for the data inside the ROD. It's up to each single detector expert to provide a specific decoding routine, as reported in Sect. 4.4.2.

Also histogramming routines are developed as independent plug-ins. Indeed they first need data to be decoded, but code is kept separated in another library to allow correlation studies. As an example, hits in the MDTs must be correlated to signals in the trigger chambers (RPC). The MDT and RPC communities developed their own separate code: two different decoding routines and two different histogramming libraries, responsible for filling detector specific plots. The same decoding routines has been re-used to feed a common histogram library, which can handle both the MDT and the RPC events. This allows any correlation plot, like *MDT-variable vs RPC-variable* without duplication of code (see Sect. 4.5).

4.4 Development of MDT specific libraries

Each detector plug-in must be implemented in GNAM as a standard Unix dynamic library, loaded at run time. The list of the desired plug-ins has to be written into a configuration text file, one plug-in per line, plus eventual initial parameters for the library itself. Here is an example for the MDTs:

```
libMDTGnamDecode.so mdtsetup.txt
libMDTGnamHisto.so
libMDTGnamEvtDisplay.so
```

The interface between the Core and the plug-ins consists of a set of callbacks (see Fig. 4.4) that the libraries can implement. None of the entry-points is strictly required: the Core will check which callbacks are defined and will use only them.
My work consisted in developing the C++ code for such entry-points, to provide functionalities as such as the decoding of raw data, the histogram filling and some event display.
The MDTGnam package, in fact, has been chosen to be the official on-line tool for MDT commissioning. The basic existing code, implemented for 2004 CTB, was working for the small set of chambers (10) under test. That's why the code needed to be completely renewed to fulfill the commissioning requirements. In the next sections the four libraries *MDTGnamBasic*, *MDTGnamDecode*, *MDTGnamHisto* and *MDTGnamEvtDisplay* will be described.

4.4.1 MDTGnamBasic

The *MDTGnamBasic* library is not a real plug-in for GNAM, since it does not appear in the configuration text file. Rather, all the other libraries link to it, since it collects common general actions which are needed at different steps. In particular, the list of chambers to acquire, their geometry and their electronic cabling must be known. One of the main modifications with respect to the basic package developed for CTB needs, is the possibility to manage a different list of chambers from run to run. The CTB code was developed for a fixed number of detectors, while we chose to keep MDTGnam as much flexible as possible. Although ATLAS is now commissioned per sector, and in the future real data taking all the 1200 chambers will have to acquire data simultaneously, it is crucial to have the possibility to connect/disconnect one

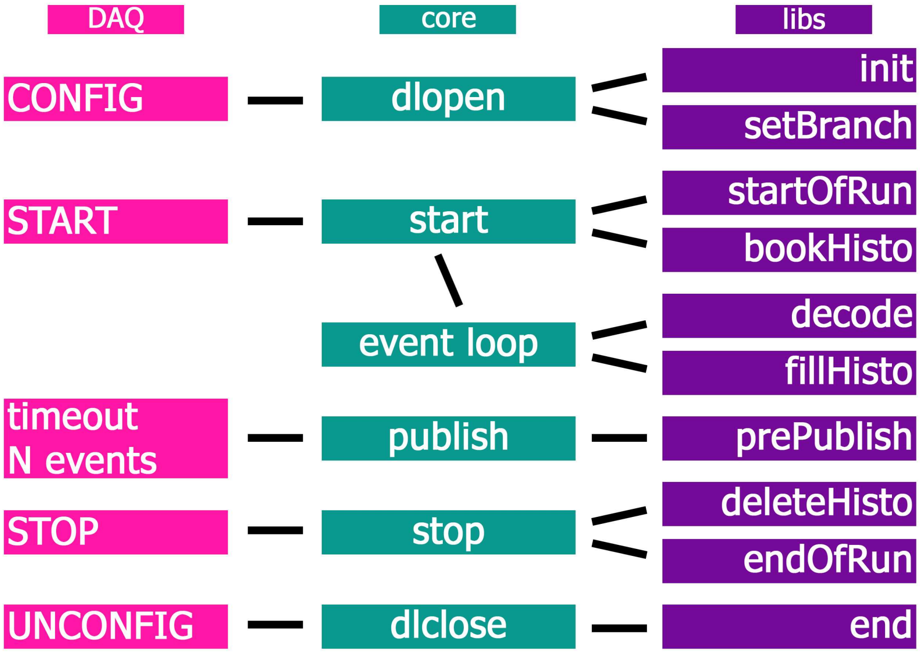

Figure 4.4: List of callbacks that can be implemented by a detector plug-in, with an indication of when they are executed.

or more chambers from the DAQ chain, for example if some channels are very noisy, keeping the event rate too high. From the GNAM point of view, the flexibility to update the effective list of acquired chambers from run to run, prevents the software from booking useless empty histograms[2] or from looping over the whole muon spectrometer to associate the electronic hit information with geometrical position. The chamber list is provided as input in the `chamberlist.txt` text file:

```
# chamber, Name, SubDetID, MrodID, CsmID,
chamber BML1A13 97 9 0
chamber BML2A13 97 9 1
chamber BML3A13 97 9 2
chamber BOL1A13 97 9 3
chamber BOL2A13 97 9 4
chamber BOL3A13 97 9 5
chamber BIL1A13 97 11 0
chamber BIL2A13 97 11 1
chamber BIL3A13 97 11 2
```

---

[2] We will see in Sect. 4.4.3 that some relevant quantities need a single plot per chamber.

Together with the name of the chamber, the Sub-detectorID, the MrodID and the CsmID are given. These electronic cabling parameters univocally identify a MDT chamber and this allows to translate unambiguously the raw data information (hit occurred on Mrod X, Csm Y, Tdc Z, channel W) into detector geometrical coordinates, such as chamber, multilayer, layer and tube. For the numbering of multilayers, layers and tubes, the standard ATLAS convention [17] has been followed.

The second requirement is the chamber geometry. MDT chambers in the muon spectrometer can have very different shapes [17]. First of all they can be composed of very different number of tubes, and tubes length[3] themselves range between 75 cm and about 6.3 m. Having the exact number of tubes and mezzanines for each single detector, allows again to save CPU and processing time, since histograms per tube/mezzanine (see Sect. 4.4.3) are booked with the minimum needed number of bins only.

Last, but not least, the correspondence between tubes and electronic channels must be provided. As shown in Fig. 4.5, four kinds of mezzanines [51] are used to acquire drift tubes. Each schema represents a different matching between the channel number (information available on raw data) and tube number, that is the actual geometrical parameter needed.

Also, the channel-tube correspondence must take into account a possible rotation of the hedgehogs. Mezzanine cards type 3 can be mounted on 6×4 chambers both the way they appear in Fig. 4.5, with the `5 3 4 2 0 1` sequence on top, and by rotating the scheme by 180°, with the `19 18 20 22 21 23` sequence on top: the **S**-shape is still preserved. The same can be done for the **Z**-shape type 4 mezzanines, while types 1 and 2 (**>**-shape), mounted on 3×8 chambers are not symmetrical with respect to 180° rotation (causing a **<**-shape).

Once the list of chambers to be read is fixed, the minimum set of geometrical parameters, such as the number of layers (*MLayers)* and the number of mezzanines per each layer (*MezzPerML*) is provided by means of the `map_file.txt`. The text file is scanned until the block corresponding to each chamber in the list is found. Here are some blocks corresponding to chambers BIL1A13 and BIL1C01 shown as an example:

---

[3] However, GNAM does not care about the tube length, since pure raw data at ROD level do not contain this information

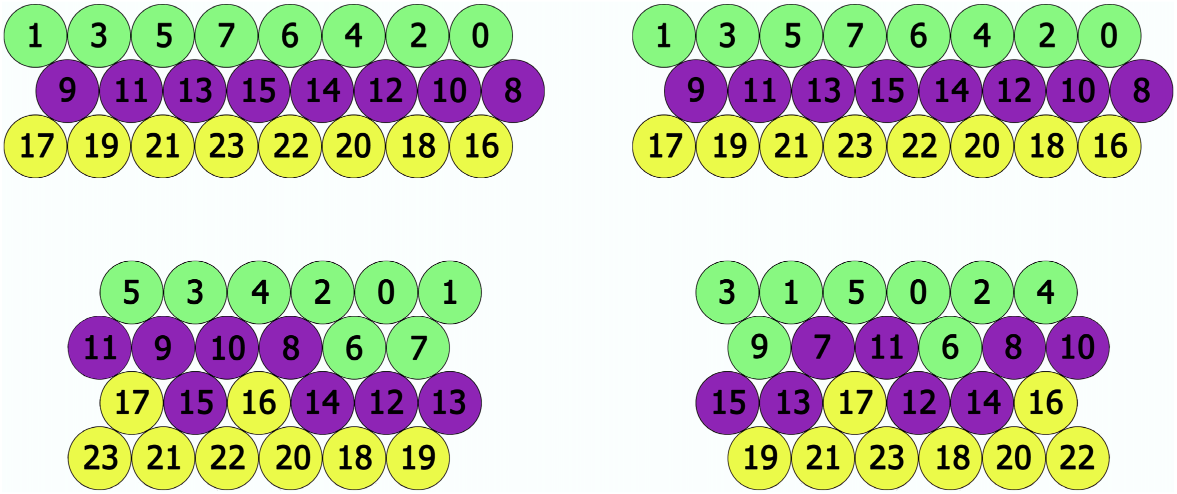

Figure 4.5: Schema of the four mezzanine types.

```
#
BEGIN_CHAMBER
   name BIL1A13
   MLayers 2
   MezzPerML 5
   MezzTypeML1 4
   MezzTypeML2 3
   IncreaseWithZ 1
   ZeroMezzML 1
END_CHAMBER
#
BEGIN_CHAMBER
   name BIL1C01
   MLayers 2
   MezzPerML 5
   MezzTypeML1 3
   MezzTypeML2 4
   IncreaseWithZ 1
   ZeroMezzML 2
END_CHAMBER
#
```

The configuration operations strictly related to chambers as separated and single objects, end with full information stored in a C++ STL (Standard Template Library) vector named `ChambList`, where the i-th component represents the i-th chamber under test. Wherever in the MDTGnam plug-in code, this vector will be called back through an ad hoc function

```
vector<Chamber> *ChambList;
ChambList=GetList();
```

and single component will be accessed in reading/writing mode through all the `Chamber` class methods (App. A.1). As an example, the name of the chamber, its CsmID, or the total number of hits occurred are stored in:

```
ChambList->at(i).name; ChambList->at(i).csm; ChambList->at(i).Hits
```

From raw data, the hit list associated with each event comes, as mentioned above, with the electronic coordinates up to the TDC channel. That's why we decided to hold all the TDC parameters into a single object, a C++ STL map named `TdcMap`. At configuration, we know where physically chambers are connected to (Sub-detectorID, MrodID and CsmID). We also know the number of TDCs and their position in the chambers. Each TDC has an identifier (TdcID) in addition, given the standard numeration of TDCs inside an ATLAS chamber
The unique key related to each TDC under test is:

```
geo_key=tdcID+CsmID*100+MrodID*10000+SubDetID*1000000;
```

As an example, with respect to the `chamberlist.txt` above, the tdc no. 2 of the BOL1A13 will be associated with the key 97090302.
Each key has been built only with configuration parameters. At this step, the raw data are still unknown. The `TdcMap` will be recalled in reading mode only at the decoding operations, through the ad hoc function

```
const map<unsigned int,Tdc> *TdcMap;
TdcMap=GetTdcMap();
```

Configuration from text file/database

The easiest and fastest way to implement all the current functionalities for the general configuration, was to work with ASCII files. Some regular structure has been defined and the minimum needed set of parameters has been chosen, in order to restrain the possibility to type wrong values. All the geometry of a chamber, consisting mostly in knowing how tubes are divided through how many TDC mezzanines, is derived from the 7 parameters of `map_file.txt`; other quantities, as for example the number of layers and the tubes per layer, are univocally related to the mezzanine type.

```
switch((ChambList->at(i)).MezzTypeML1){
  case 1:
  (ChambList->at(i)).LayersPerML=3;
  (ChambList->at(i)).TubesPerLayer=8*(ChambList->at(i)).MezzPerML;
  break;
  case 2:
  (ChambList->at(i)).LayersPerML=3;
  (ChambList->at(i)).TubesPerLayer=8*(ChambList->at(i)).MezzPerML;
  break;
  case 3:
  (ChambList->at(i)).LayersPerML=4;
  (ChambList->at(i)).TubesPerLayer=6*(ChambList->at(i)).MezzPerML;
  break;
  case 4:
  (ChambList->at(i)).LayersPerML=4;
  (ChambList->at(i)).TubesPerLayer=6*(ChambList->at(i)).MezzPerML;
  break;
}
```

Different databases have been developed for ATLAS commissioning and real data taking; geometry and calibration parameters will have to be extracted from there. But functions for accessing the databases have not been developed in the MDTGnam package yet: a joint effort from MDTGnam and database developers is currently ongoing, to optimize the relative procedures. However, the structure of the code already allows the choice of the source of information (text file or database), and once the needed parameters are read (no matter where) they are handled the same way. No duplication of the existing code is therefore needed.

4.4.2 MDTGnamDecode

The *MDTGnamDecode* library is devoted to the real decoding of the raw data, that is the extraction of geometrical information of hits occurred (chamber, multilayer, layer and tube) from pure electronics (MROD, CSM, TDC and channel). It is the crucial plug-in since no other operations, as histogramming or event display (which still can be technically implemented) make sense if the data decoding is wrong or unknown.

The *MDTGnamDecode* library is entirely based on the decoding of raw data format, which reflects the data flow structure (see Sect. 4.2).

DAQ specifications do not impose any fixed structure for the data sent out by the front-end electronics (FE); when making up a fragment, a ROD may add some detector specific meta-data to the data collected from the FE. But from the next level on the format is fixed and independent of the data source. The ROD fragments must be encapsulated between ATLAS standard header and trailer, and in turn, new headers will be added at higher levels in the data flow.

The global structure for a full ATLAS event is shown in Fig. 4.6: more details can be found in [50].

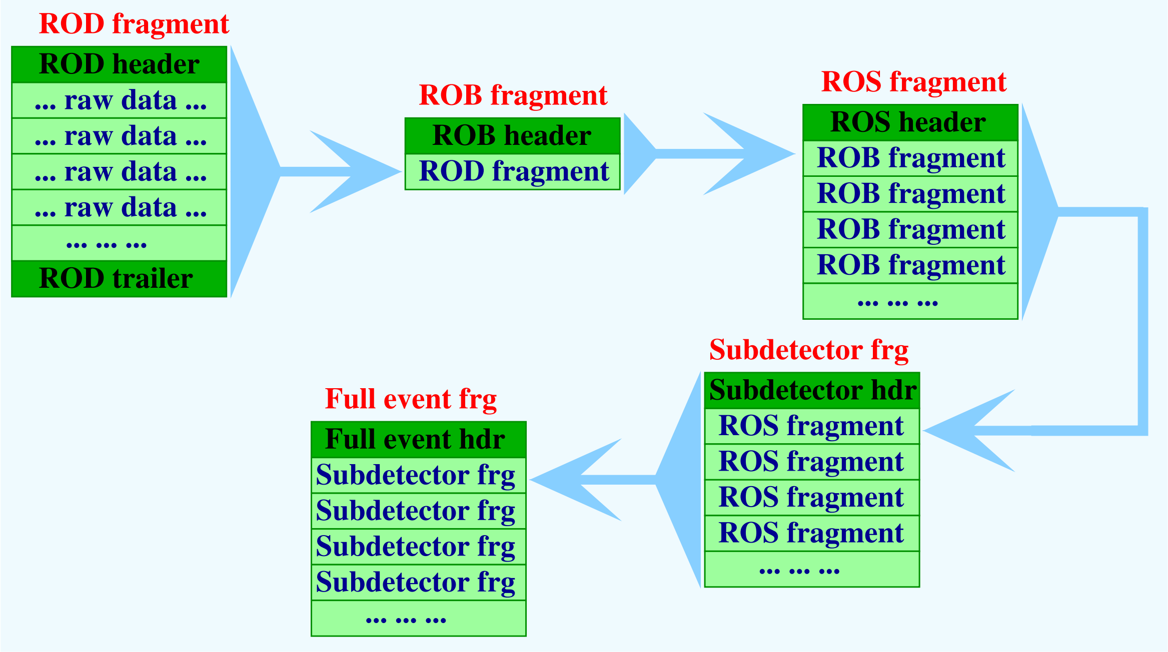

Figure 4.6: Data format in ATLAS. Raw data format is detector-dependent, but the encapsulation is defined by the ATLAS specifications.

The *decode* entry-point is called at each event (see Fig. 4.4) and each time the GNAM Core provides the full list of RODs of that event. Due to the internal structure of MDT ROD fragments (App. B.1 and [52]), the decoding function has been developed into different steps, to get different details of hit information.

1. Decoding of the ROD header: here the MDT fragments are identified and the other detector ones are rejected.
2. Decoding of the MDT data: list of hits occurred in each channel is stored with electronic coordinates (Mrod, Csm, Tdc and channel) together with physical quantities, like the drift time and the accumulated charge.
3. Hit mapping: the electronic coordinates are translated into geometrical parameters, such as the hit chamber, multilayer, layer and tube.

A simplified event structure and the related decoding steps are visible in Fig. 4.7.

The ROD header

In order to optimize the MDTGnam package performances (time and resource saving), the first thing to do is to recognize MDT fragments, among all the other subdetectors ones, through the sub-detector ID in the ROD header: from 0x61 to 0x64 for barrel and end-cap MDT chambers. If the sub-detector ID is not a MDT one, the current ROD fragment is immediately skipped until MDT data are found[4].

The MDT data

Each MDT fragment contains from 1 to 8 Csm blocks, that is, data from 8 different chambers. The beginning and the end of the Csm blocks are tagged by two dedicated words, the LWC (Link Word Count) and the TWC (Trailer Word Count). If a LWC is found, the *HandleCsmBlock* function is called, else some data integrity check (see Sect. 4.6) are performed and potential corrupted data are skipped. Inside each Csm block, a maximum of 18 TDC blocks can be foundTDC blocks start with a BOT word (Begin Of Tdc) and end with a EOT (End of Tdc). Each time a BOT is found, the *HandleTdcBlock* is responsible for extracting the complete hit information.

---

[4] It's up to the other detectors to provide their specific GNAM decoding plug-in to analyze their own ROD fragments.

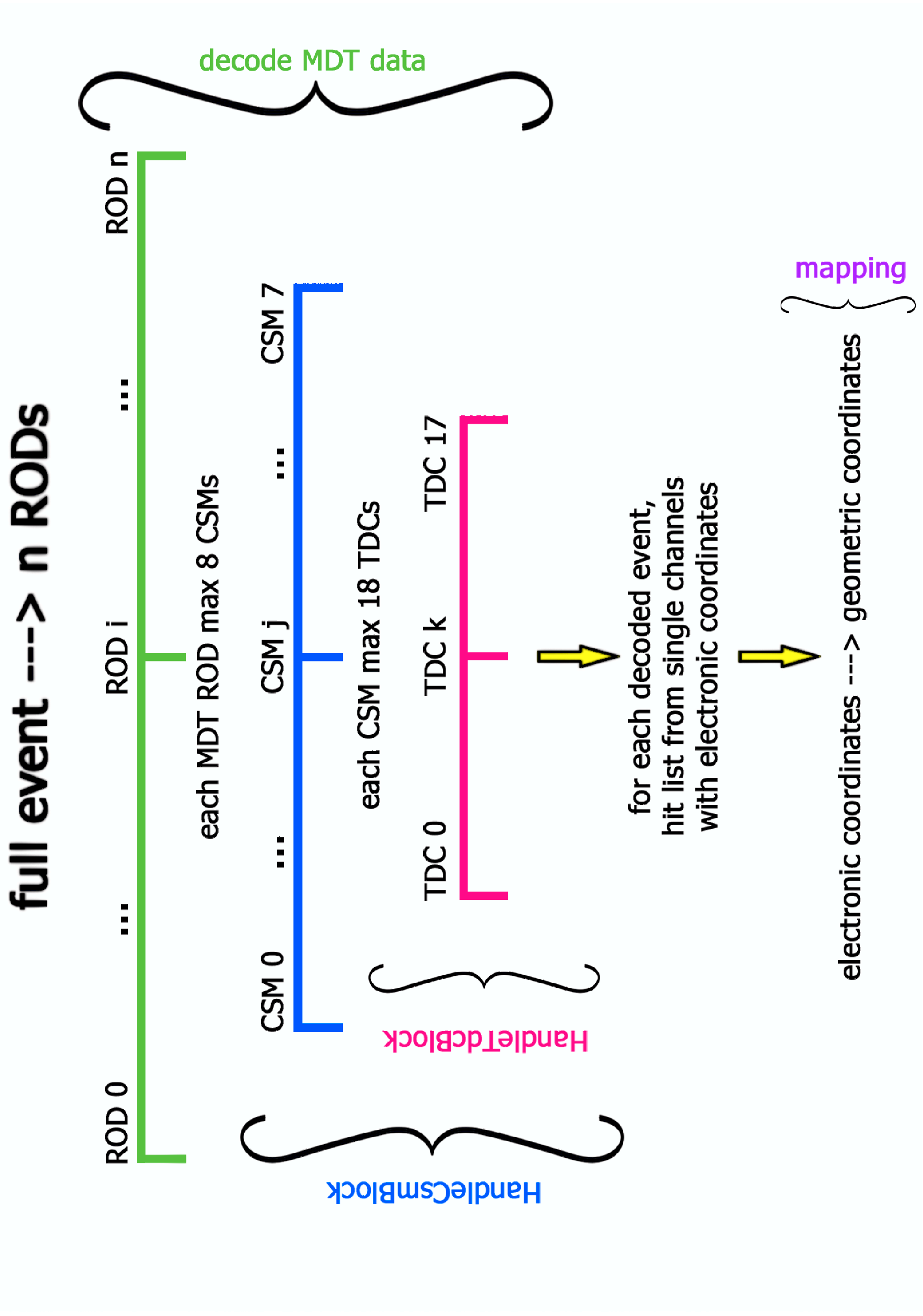

Figure 4.7: Event structure and decoding operations.

Hit mapping

Last step is to associate the collected hits to the chamber, multilayer, layer and tube where they occurred. As stated in Sect. 4.4.1, each tdc on each chamber is identified through a `geo_key` in the `TdcMap`. A similar `evt_key` is built at decoding time when a tdc has been hit, since the raw data stream provides the SubDetectorID, MrodID, CsmID and TdcID. This `evt_key` is passed to the map:

```
map<unsigned int,Tdc>::const_iterator it=TdcMap->find(evt_key);
```

The map will return the exact TDC where the hit has occurred, when the `evt_key` matches `geo_key`. In particular, taking into account the mezzanine type of that TDC (Fig. 4.5), chamber, multilayer, layer and tube will be given through ad hoc algorithms developed for this purpose.

At the end of the *decode* entry-point, the event with the full hit list is stored into the object `evt` of the class MdtEvent (App. A.2) and is accessible from all the other plug-ins.

4.4.3 MDTGnamHisto

The *MDTGnamHisto* library is the plug-in devoted to histogramming. During GNAM Core development, ROOT[53] has been chosen as histogramming package for all the detectors, since it is a powerful and well known tool for physics analysis. Histograms are actually ROOT histograms with some more option, provided by the GNAM Core for on-line purposes. Several steps are foreseen for each histograms:

Booking. At first histograms must be booked. The histogram type is selected (1D or 2D) and appropriate names are given. The booking operation is done just once a run, before the data acquisition starts.

Filling. Histograms are filled in the event loop. New entries can occur from event to event.

Publishing. At regular time intervals or each fixed number of events, histograms are published on the On-line Histogram Service (OHS) so that each application developed for histogram display purposes can access them.

Displaying. Histograms are displayed through the OHP [49].

Saving. When the run is stopped, that is, when GNAM is no longer fed with events, histograms are saved in a ROOT file. The file is then permanently stored on disk.

Booking

The histogram booking is done at the dedicated *bookHisto* entry-point. As shown in Fig. 4.4, it is called at run time, immediately before events are sampled. The choice of GNAM Core to have the *bookHisto* function at this point, is related to the runtype (cosmics or noise for MDT commissioning) choice. Different runs may need different kind of plots, since they provide different information about the health status of the chamber. The run type, in the DAQ system, is only known at the START state. The possibility to book histograms with respect to the run type prevents the software from wasting resources with useless/empty plots. In addition, different definitions for the same physical quantities can be given according to the run type. Histogram names must follow the histogram naming convention [54] imposed by the ATLAS Monitoring Working Group: histograms must be grouped according to the level of information they provide (shifter, expert or debug mode). Moreover, other subfolders have been intoduced to have histograms "logically" separated per chamber. In particular:

/SHIFT/MDT/Overview/ : containing general summary plots as the hit multiplicity, hits per chamber, average noise level.

/EXPERT/MDT/Errors/ : summary plots with errors occurred, exploiting the data integrity checks performed in the *decode* function (Sect. 4.4.2).

/SHIFT/MDT/*chamber name***/** : some relevant quantities must be monitored from chamber to chamber, as the TDC and ADC distributions.

/EXPERT/MDT/*chamber name***/** : here are other plots which an expert may want to study in detail, but which are not so clear for the shifter.

/DEBUG/MDT/*chamber name***/** : here are all the other plots, which can be studied if anomalies occur. For example, some distributions are displayed for each tube of each chamber.

Filling

The *fillHisto* entry-point is the place where the information stored in the decoded events is used to fill histograms. As shown in Fig. 4.4, the *fillHisto* is called after the *decode* in the event loop: this means that one-by-one event is analyzed and used to fill the existing booked histograms. Some histograms need to be normalized at the number of events occurred: for instance, the noise frequency is related to the ratio between the noise counts and the total number of hits. In this case, at the *fillHisto* some counters are increased each time a hit occurs on that tube/mezzanine/chamber, but histograms are filled at the *prePublish*, after some statistics has been accumulated.

Publishing

The histograms produced by GNAM are published on the OHS at regular time intervals or after a pre-fixed number of events. This allows GNAM to be an on-line tool, since the shifter can monitor the physical quantities while data are being acquired, without waiting for the end of the run (which may also take some hours). The *prePublish* entry-point is called in the event loop just before histograms are published. Here some standard ROOT operations can be done, like resetting (for example the noise frequency plots mentioned above) or fitting histograms. By default, as soon as the data acquisition is stopped, the *prePublish* function is called again, to ensure the most refreshed plots.

Displaying

The official tool for displaying MDTGnam histograms at commissioning sites is the above mentioned OHP. It allows a browser mode, as in ROOT, where the shifter can look for the required histogram once he knows the full name, or a tab mode, where only some relevant plots are shown.

With a small number of chambers (that is a limited number of histograms), the most suitable choice was to have a summary configured tab, collecting general information on the data acquisition, and a tab per chamber, where different quantities are monitored chamber by chamber (for example TDC, ADC, number of hits per tube, noise frequencies per tube) as shown in Fig. 4.8.

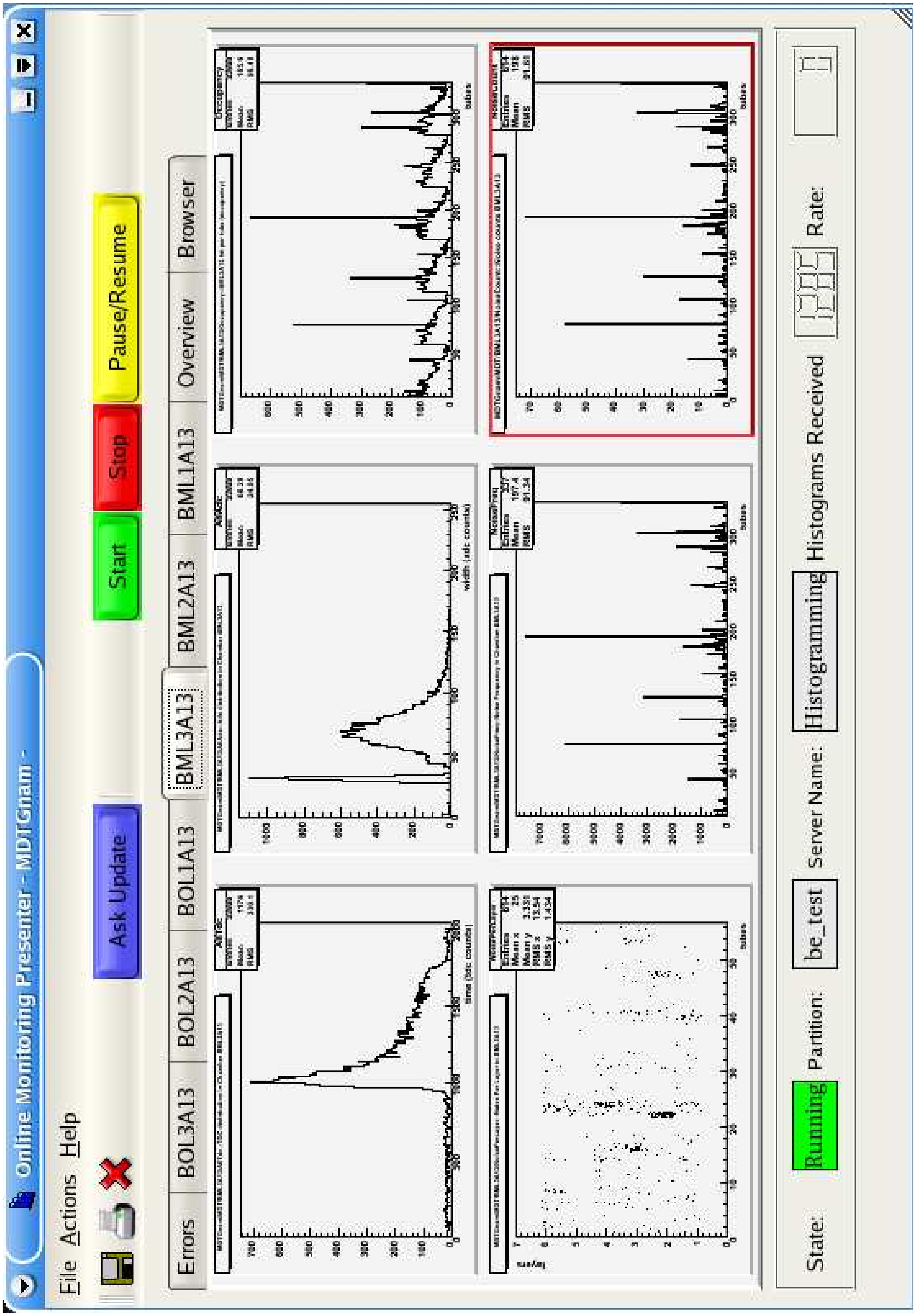

Figure 4.8: Pre-configured OHP tab for a specific chamber.

OHP requires an input file where these tabs are configured. Since a tab per chamber is needed, a dynamic text file is created/overwritten at each run at the *bookHisto*, so as to have only histograms for the specific run type (noise or cosmics) and for the chambers under test: this prevents OHP from creating empty tabs. However, with more and more chambers to test, the number of tabs cannot diverge anymore, since the relevant histograms, which give information on the general status of the detector, must in be well in evidence for the shifter. A small subset of summary plots, collecting information from different MDT chambers, must be chosen, to provide the shifters with a first and fast general look on the status of the detectors under test. Presently, these decisions are strictly related to the development of the Data Quality Monitoring Framework (DQMF) (see Sect. 4.6).

Saving

By default, at the END DAQ state all the booked (and in case filled) histograms are saved in the ROOT file, where the organized folder structure is preserved, as shown in Fig. 4.9. The ROOT file will be also available off-line to run, in case, some ROOT macros. Anyway, neither the full GNAM project, neither the MDTGnam package, have been designed for an official off-line use.

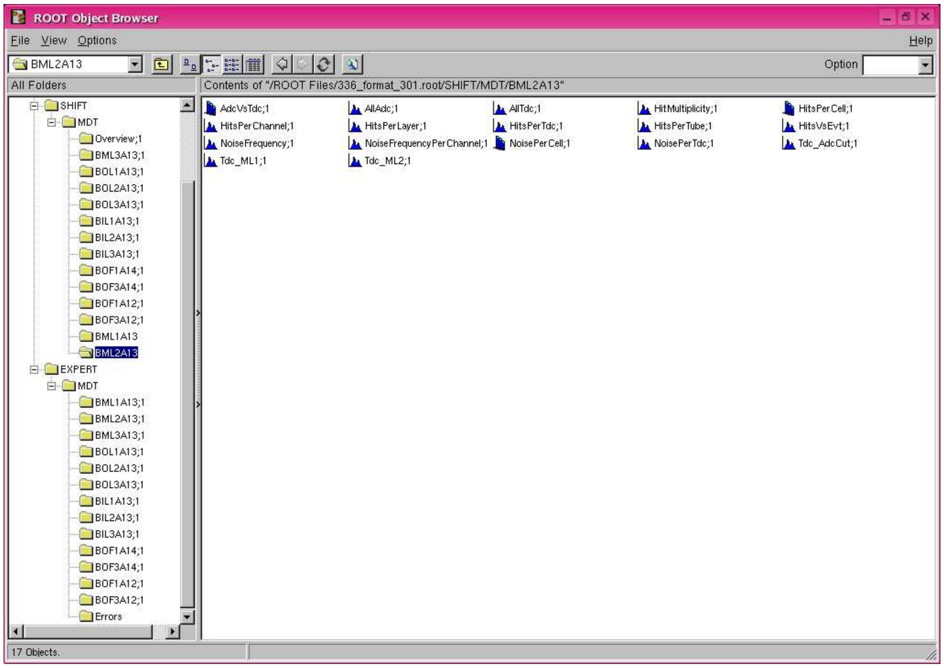

Figure 4.9: The folder structure of the ROOT output file.

4.4.4 MDTGnamEvtDisplay

The MDT community has expressed interest in having an on-line event display, which could give a fast overview on the geometrical distribution of hits through the chambers. No calibrations, nor track reconstruction were required: just a quick tool which, event by event, turns on some light on the fired tubes (see Fig. 4.10).
The GNAM Core developers never designed a specific entry-point for event display, but from the joint effort of the MDTGnam package and `PERSINT` [55] collaborations, it was possible to have this kind of tool.
In fact, `PERSINT` requires as input an ASCII file with a specific format, as the one which follows. It just contains the hit list event per event, with both geometrical information (chamber station, eta, phi, multilayer, layer and tube) and physical quantities, as TDC and ADC measured counts.

```
NEW EVT 4 0 1 1
HIT 12 0 0 0
MDT BML 3 7 1 3 20 0 0 0 696 99 0 6 0
MDT BML 3 7 1 2 19 0 0 0 620 129 0 6 1
MDT BML 3 7 1 1 20 0 0 0 372 91 0 6 2
MDT BML 3 7 2 3 18 0 0 0 435 126 0 6 3
MDT BML 3 7 2 2 17 0 0 0 918 126 0 6 4
MDT BML 3 7 2 1 18 0 0 0 359 129 0 6 5
MDT BML 3 7 2 3 54 0 0 0 2418 34 0 6 6
MDT BOL 1 7 2 2 47 0 0 0 1479 36 0 6 7
MDT BOL 2 7 1 2 48 0 0 0 530 201 0 6 8
MDT BOL 2 7 2 2 46 0 0 0 311 98 0 6 9
MDT BOL 2 7 2 1 47 0 0 0 392 109 0 6 10
MDT BOL 3 7 2 1 41 0 0 0 1938 34 0 6 11
END EVT 4
NEW EVT 5 0 1 1
HIT 18 0 0 0
MDT BML 2 7 2 1 16 0 0 0 168 34 0 6 0
...
END EVT 5
```

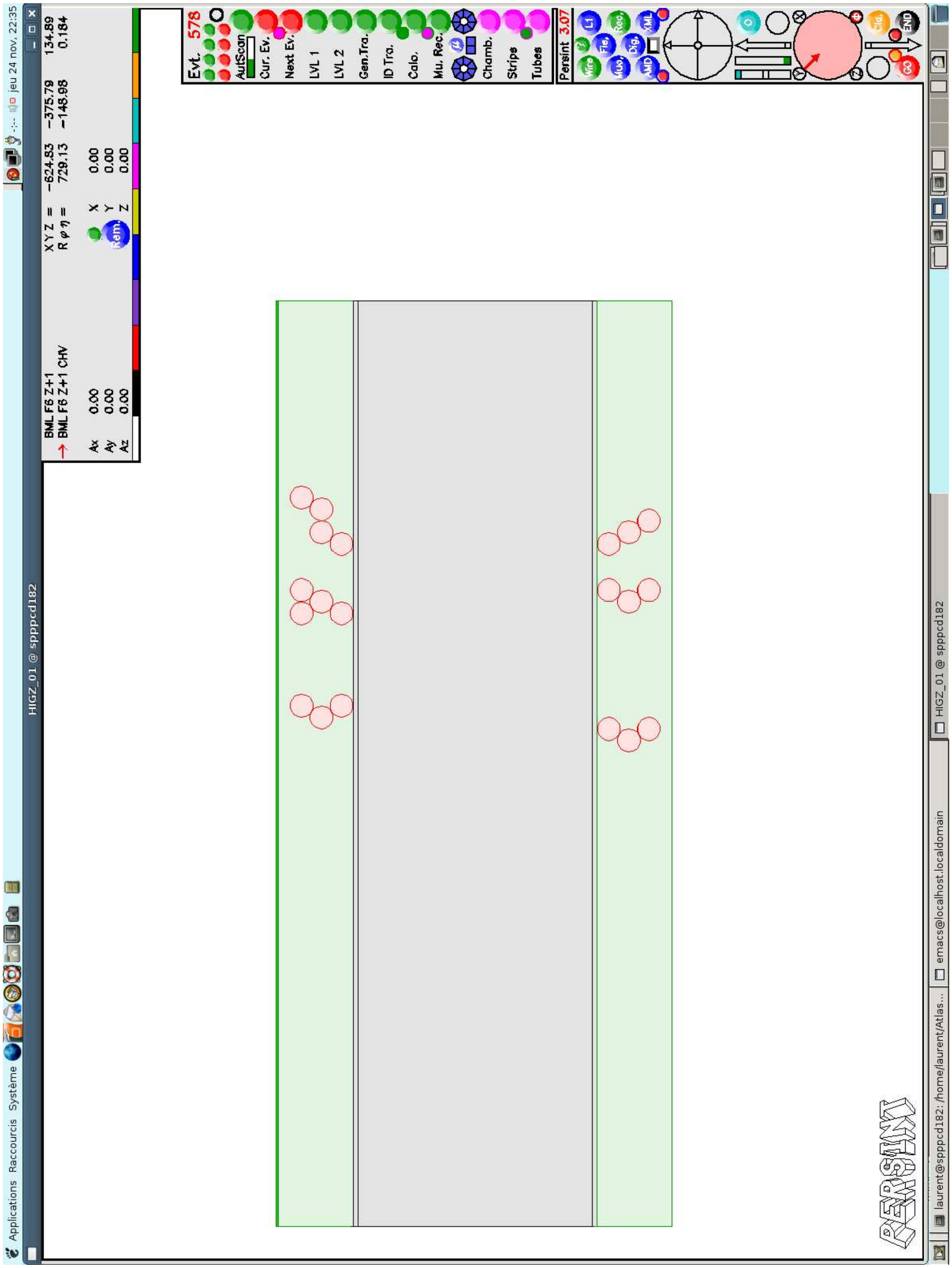

Figure 4.10: Event display with PERSINT.

All these variables are known in MDTGnam, after the event is decoded. For example, they are used in the *fillHisto* to fill histograms. And the *fillHisto* is the natural place where this information is available and can be written on the ASCII file.
To keep the histogram filling separated from the event display, since they are two logically different actions, another library has been designed. This other plug-in has been developed following the standard GNAM entry-points. In particular, the *init* and *end* function cares about opening/close both the ASCII file and the circular buffer, while the *fillHisto* actually handles the hit information and writes it on the output. This library is independent from the *MDTGnamHisto* and technically, could run stand alone. However, to have a physical meaning, of course it needs the configuration and the decode libraries (*MDTGnamBasic* and *MDTGnamDecode*).

4.5 MDT+RPC combined library

The GNAM structure allows independent libraries to be developed for different detectors and for different purposes. In parallel with MDTGnam, the RPC (Napoli) community has developed the RPCGnam package, for the on-line monitoring of their subdetectors. But in the same physical event, signals on drift tubes are directly correlated with signals on the RPC strips. That's why from the muon spectrometer collaboration, the request for combined on-line MDT+RPC histograms strongly arose.
These histograms can be created, filled and published using the detector independent skeleton of GNAM: two different decoding libraries were already developed by MDT and RPC groups, to be used in stand-alone mode in MDTGnam and RPCGnam respectively. The two libraries provide the MDT event and the RPC event, or, better, they provide the list of signals that the penetrating muon (that is the physical event) generated separately in the drift tubes and in the strips.
A new *MuonBarrelHisto* library has been developed to merge the information from both subdetectors and to produce combined histograms.
First of all it has to be checked if MDT hits are correlated with RPC hits, that is, if we are really looking at the same event from MDT side and from RPC one. This can be done by comparing the *BunchCross Identifier* which is extrapolated from the ROD header. Then, from a pure technical point of view, any MDT variable can be

displayed versus a RPC variable, to generate the desired combined histograms. At the moment the code is just starting to be written four-handed and only the time correlation plot has been added (Fig. 4.11).

Another typical plot to be introduced is the MDT hit tube versus the corresponding RPC fired strip; taking into account the toroid bending power, for each hit tube, just a few RPC strips will fire in the immediately upper/lower RPC plates. The same combined information will be used for a combined event display, which will help us to distinguish good hits from pure noise.

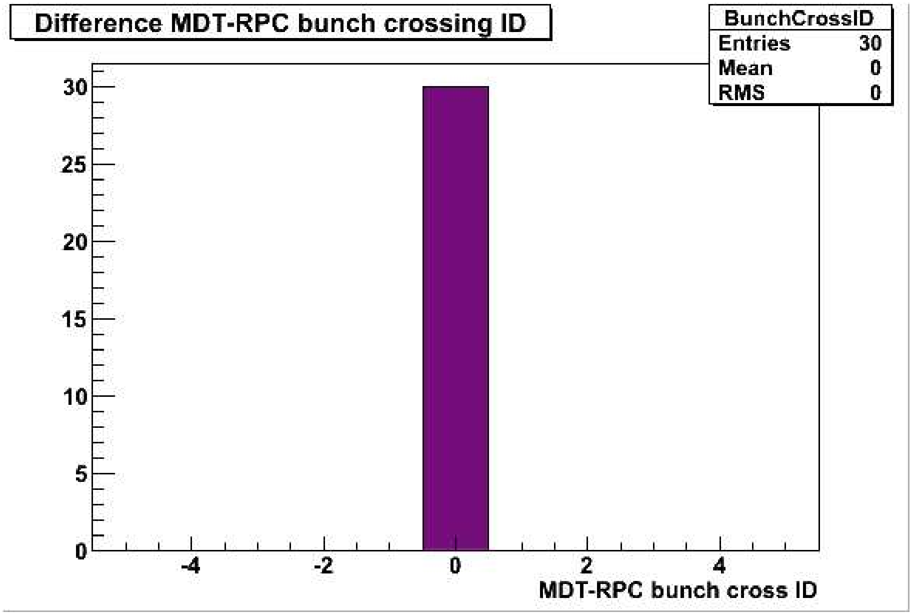

Figure 4.11: Difference between the bunch crossing IDs from MDT and RPC fragments.

4.6 Data Quality Assessment

During the last year, the ATLAS community has expressed a strong interest in Data Quality Assessment (DQA). Although trigger levels reduce the amount of data from 120 GB/s to 300 MB/s (see Fig. 4.1), it is essential to save as many disk space and resources as possible. Lot of events could contain corrupted data, above all in the initial phase when both LHC and the ATLAS sub-detectors will need a lot of tuning. The Data Quality group is defining a strategy to allow each detector expert to run algorithms (both on-line and off-line) devoted to check the integrity of the data, and to establish how good is a run for the off-line analysis. For these purposes, the *Data Quality Monitoring Framework* (DQMF) [56] is being developed independently of any specific detector technology.

MDTGnam is strongly involved in DQA activity, since on-line checks allow a very fast response. Of course, MDTGnam does not care about calibration, tracking or higher level physics studies: it's not up to GNAM to decide if a run is good or not. But before any physics study, one has to be sure that data are not corrupted and all the detectors were plugged in; details about the status of the chambers, as noisy or dead channels must be given too. These operations are already done by MDTGnam and results are saved as histograms or summary files, as the one below. For each chamber, information about dead/noisy channels are reported.

```
BOL3A13: tot. hits 107166    average noise freq. (kHz) 0.208
------------------------------------------------------------
---> 0/12 dead mezzanine(s) and 0/12 noisy mezzanine(s)
tube    AtlasId    hits    freq. (kHz)   < adc cut
  31       1131       3       0.000         0.000  <- DEAD
 182       2138    1394      11.585        11.585  <- NOISY
---> 1/288 dead tube(s) and 1/288 noisy tube(s)
multilayer    t0 (counts)    tmax (counts)   drift time (ns)
    1            247.959         1131.726           690.443
    2            245.340         1131.671           692.446


BIL1A13: tot. hits 34619     average noise freq. (kHz) 0.620
------------------------------------------------------------
mezzanine       hits     noise freq. (kHz)
    9          15782          133.869      <- NOISY
---> 0/10 dead mezzanine(s) and 1/10 noisy mezzanine(s)
tube    AtlasId    hits    freq. (kHz)   < adc cut
 239       2429   12906     132.872      132.872 <- NOISY
---> 0/240 dead tube(s) and 1/240 noisy tube(s)
multilayer    t0 (counts)    tmax (counts)   drift time (ns)
    1            127.597         1036.706           710.241
    2            129.728         1051.513           720.145
```

MDTGnam & the Data Quality Monitoring Framework

The DQMF offers a framework where both basic or detector specific algorithms (mainly ROOT macros) can run automatically on MDTGnam histograms; the result of these algorithms is a green/yellow/red light, signaling the status of the run.
Let's suppose a chamber has 2 dead tubes; this information is stored in the database. A run is being acquired and MDTGnam fills the *HitsPerTube* plot. The shifter looks at this histogram on-line on the OHP and sees there are 5 bins with no entries, actually 5 dead tubes. He should access the database to check if those 5 tubes are known to have some problems or not. In this case, since the information from histograms (5 dead tubes) doesn't match the information on the database (only 2 dead tubes), the shifter should arise a warning about the bad status of the current run.
In the DQMF, all these operations can be automatized. This reduces the number of relevant plots that the shifter must have well in evidence during the data acquisition, since the algorithms run in parallel with the histogram publishing/displaying.
Some basic controls provided by the DQMF are:

- check on empty bins (to look for dead channels or disconnected chambers);
- check on bins over threshold (to look for a too noisy tube, once a maximum value has been set);
- check on mean values.

Data integrity

As stated in Sect. 4.4.2, integrity checks on raw data are crucial, since a huge number of events must be decoded and resources must be optimized. Some software, running off-line after data have been acquired, already existed; the next step was to implement such these operations in the on-line framework, and again, the MDTGnam package was the ideal place where to integrate them.
The *MDTGnamDecode* library has to control each single word of the data flow and it naturally rejects useless fragments. Each time a word is not found where expected (according to the official raw data format described in [52]), some warning messages are arisen and the appropriate `SetError` function is called with an error code.

Since various parts of the raw data can be corrupted, a different error code is assigned to each kind of bug, so as to quickly identify the source of the problem. Actions to be taken at generated alarms can be different: some errors require the entire block to be skipped, some others, which don't affect the full subsequent chain, should only be signaled. The official data format, in fact, already foresees some dedicated bits, flagging, as an example, transmission errors from the MROD to the CSM, or from the CSM to the TDC. In any case, rather than storing the error messages on log files, histograms are filled with the error codes (one bin per error), to investigate which error occurs the most (Fig. 4.12a) and on which chamber (Fig. 4.12b). In the DQMF, for example, one should set a maximum number of allowed errors and then use this information to flag the run as good or bad.

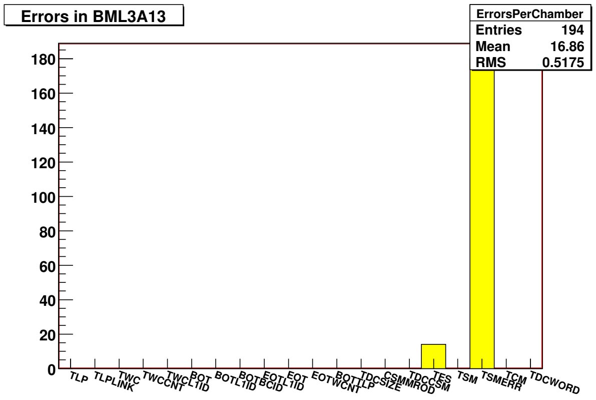

(a) error codes

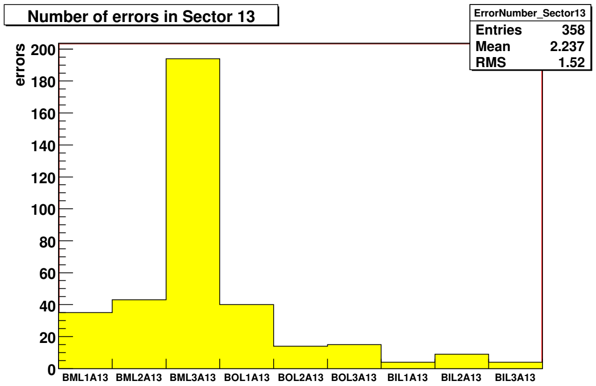

(b) chambers with errors

Figure 4.12: Error codes on a single chamber and number of errors per chamber.

Fit of the calibration constants

In Sect. 3.5.4 the importance of the drift parameters, which are derived from the TDC spectra, has been clarified. T_0 and t_{max} fits must be carefully evaluated, taking into account the accumulated statistics and the environmental parameters; drift properties, in fact, strictly depend on gas composition, temperature and pressure. These parameters are not known inside MDTGnam, since they are not extracted from the raw data stream. Nevertheless, histograms produced by MDTGnam can help in monitoring the mixture status. For instance, it is expected that maximum drift time distribution as a function of the time is flat if no sensible changes happen inside the gas.

At run time, for each event, TDC spectra are filled for both the multilayers of each chamber and for all the mezzanine cards. The Ar-CO_2 mixture, in fact, flows into the two multilayers of the same chamber through two different gas distribution lines, that's why each multilayer must be monitored separately. On the other hand, t_0 depends on electronic cabling, and tubes belonging to the same mezzanine card have quite the same t_0.

When the minimum needed statistics is accumulated, fits are performed on-line by means of the *MdtCalibT0* package: this software was already developed and used inside *Athena*, but it is also very useful for MDTGnam. Such an automatic procedure just needs histograms as input: neither fit ranges nor already set parameters are requested.

Fitted histograms cannot be displayed on-line, since the OHS doesn't support fit functions; but they are saved in the ROOT file to be viewed off-line at the end of the run. Fig. 4.13 shows both multilayers of a BML chosen as an example: both spectra are fitted with the standard functions (see Sect. 3.5.4) for t_0 and t_{max}.

Anyway, fit results can be used to feed on-line other histograms, such as t_0 and t_{max} stability as a function of time[5], as it is shown in Fig. 4.14.

---

[5] Rather than time as minutes/hours spent from the beginning of the data acquisition, this kind of histograms is produced as a function of the increasing number of decoded events, each time the *prePublish* entry-point is called.

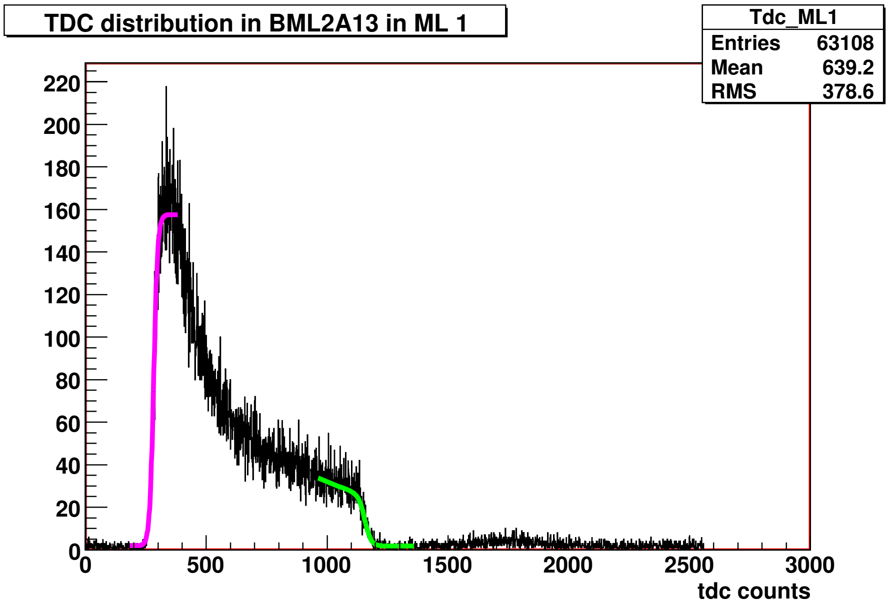

Figure 4.13: Fitted tdc spectrum for BML2A13 multilayer 1.

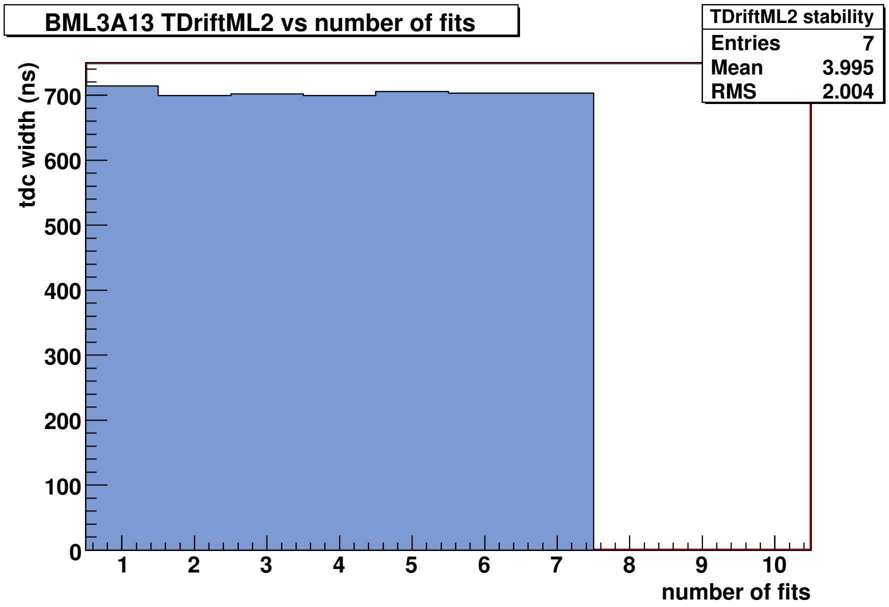

Figure 4.14: Maximum drift time at each fit operation, with increasing statistics from time to time.

4.7 Conclusions

With the 2004 CTB, where all the detectors of an entire slice of ATLAS was acquired simultaneously, monitoring tools were strongly needed. GNAM played an important role, to provide fast on-line monitoring for MDT, RPC and Tile calorimeter. For this reason, the MDTGnam package has been chosen as official tool for the MDT commissioning activities in the pit and for the real ATLAS data taking. It came out as a very robust and flexible software, providing lot of information for each chamber under test, both as histograms displayed on-line and text files summarizing the status of the run.

It is worth to stress that huge work has been carried out from the beginning of my PhD until now. Not only the code had to be maintained and optimized, but also people needs during commissioning activities have changed and have been satisfied.

Many details have been given in this chapter, since MDTGnam cannot be defined only as a histogram producer. Each time new demand was arisen, both from the muon community and from the TDAQ group, MDTGnam has always been prompt (and often the first!) in testing and implementing new features. It has been naturally involved in the Data Quality Assessment activities, providing the basis for most refined check operation to be done in the Data Quality Monitoring Framework.

Chapter 5

Analysis on barrel sector 13 data

5.1 Introduction: the barrel MDT commissioning

The ATLAS muon spectrometer has been designed to ensure a moment resolution $\Delta p_T/p_T$ of 10% for 1 TeV/c. This aim can be achieved only if the various subdetectors are reliable and efficient, to ensure good performances all over the LHC data taking. As stated in Chap. 3, Monitored Drift Tube Chambers have been designed to survive 10 years of ATLAS operation at least, and irradiation studies on a MDT-like small chamber, proved they are robust enough to face the high rate and high background environment of the ATLAS experiment.

The high reliability of the MDT chambers is assured by a series of more "elementary" but stringent tests, from the 11 production sites all over the world to their final position in the ATLAS cavern. At the production sites, each single tube is certified by means of the standard *Quality Assurance & Quality Control* (QAQC) [32] procedure, where gas tightness, dark currents, mechanical tension and wire centering are measured. Then tubes are assembled to shape a complete chamber and new tests are performed by equipping each chamber with the electronic read-out and high voltage distribution boards. The response of each single channel is checked and noise level are measured as well.

Since the mass production of final electronics has started only in 2005, a few prototypes have been temporarily used for different chambers. Once at CERN, all the chambers have been equipped with their own full read-out electronic chain, with the alignment optical system and with temperature and magnetic field sensors: middle and outer chambers have also been integrated with their own RPC plates. Once chambers were provided with their final cabling, cosmic rays have been ac-

quired to look again at the single tube response and noise level.
Then the production sites have certified the chambers as *Ready For Installation* and moved them to the SX1 experimental area, that is the surface site above the ATLAS pit. Further noise and pulse tests have been performed to ensure that chambers suffered no damage in the transport from CERN buildings to SX1.
At this point, chambers are ready to be installed on the ATLAS muon spectrometer frame. They are required to pass the final three level commissioning certification:

- Level I. Just after installation, quick integrity tests are performed, such as gas tightness. High voltage is provided to each single tube to look for dead tubes or shorts.

- Level II. Once chambers are placed on the rails, where they will slide to their final position, low voltage, front-end electronics initialization, temperature and B-field sensors are checked. Chambers such as BILs and BISes, for example, will no longer be accessible once they have been put in their very final position.

- Level III. At this level, chamber are provided with final services and connected to the gas distribution system. Final noise and cosmic ray runs can be performed.

5.2 Commissioning of sector 13

The barrel sector 13 (the lowest sector, as shown in Fig. 5.1) was used as a pilot system for the ATLAS muon spectrometer: for the first time, cosmic runs were acquired with MDT and RPC chambers as a part of the ATLAS detector. The sector 13 commissioning has started in December 2005, with 3 BMLs and 3BOLs integrated. Various noise and cosmic runs were taken: both separately on MDT and RPC chambers and combined MDT+RPC runs as well as 2 combined runs with the MDT and one Tile module. The trigger system was provided by a scintillator, used for most of the runs (rate 1 Hz); since June 2006 the RPCs of sector 13 chambers started to be used (rate 50 Hz). In this chapter I will focus on the November 2006 commissioning activities, where BILs and BOFs completed the test set-up. Noise runs were acquired as foreseen for the Level III certification and a threshold scan

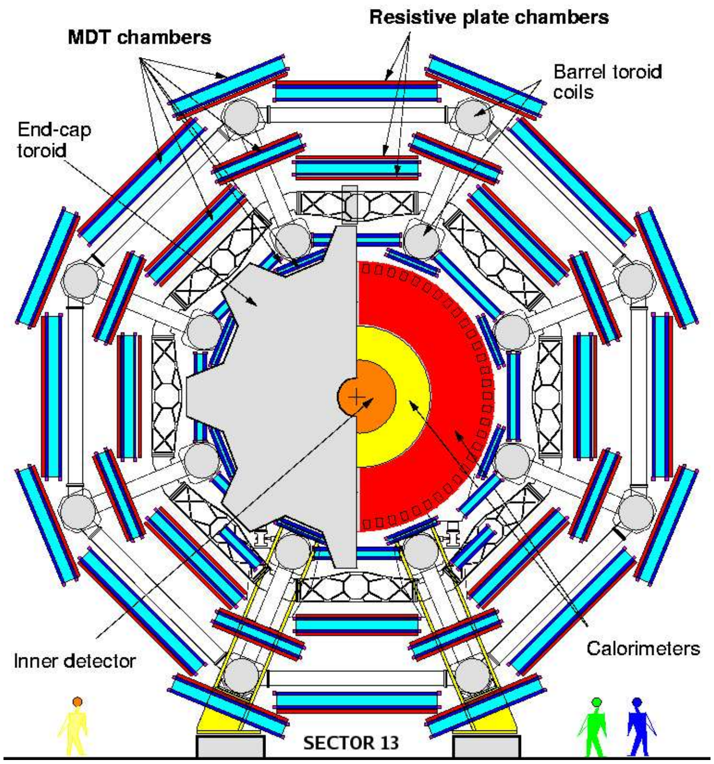

Figure 5.1: Transverse view of the spectrometer.

was performed in addition, to properly tune the discriminator threshold [21]. Cosmic data was acquired as well, experiencing, for the first time, the ATLAS barrel toroidal magnetic field. About 1 M events have been collected and analyzed, to study MDT and RPC detection performances in a more realistic environment, with respect to past cosmic ray tests with magnetic field off.

In the next sections, I will report my results from the monitoring of drift parameters and the extimation of noise levels.

5.3 Experimental set-up

For the 2006 November test, thirteen MDT chambers from sectors 12, 13 and 14 side A were connected: BIL1-2-3A13, BML1-2-3A13, BOL1-2-3A13, BOF1-3A12 and BOF1-3A14[1]. Sector 13 RPC chambers were connected as well, providing a trigger rate of ~5 Hz/m^2. Sector 12 and 14 chambers have not been analyzed, since they were not operated with their own RPC plates.

---

[1] Chambers are numbered from 1-n with increasing |z|, as shown in Fig. 5.2 and reported in Sect. 2.6.1

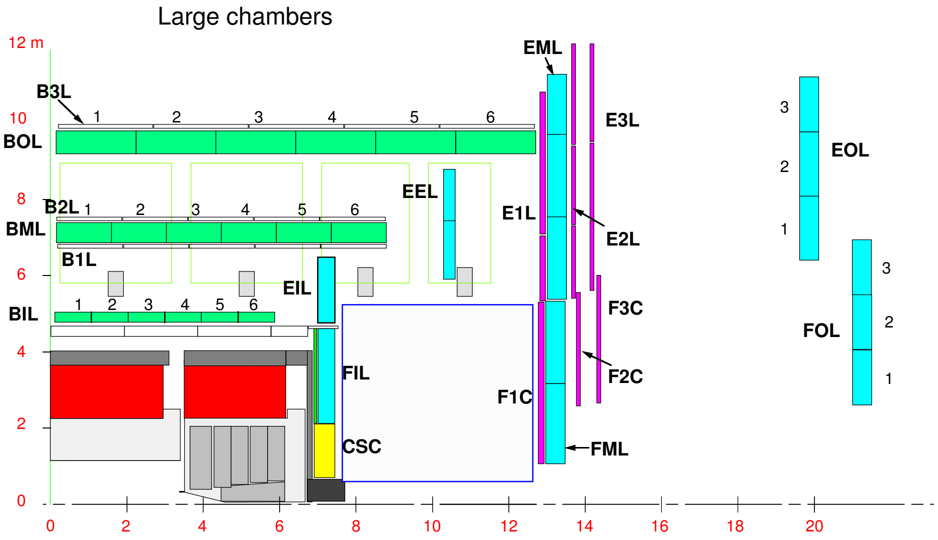

Figure 5.2: Front view of the spectrometer.

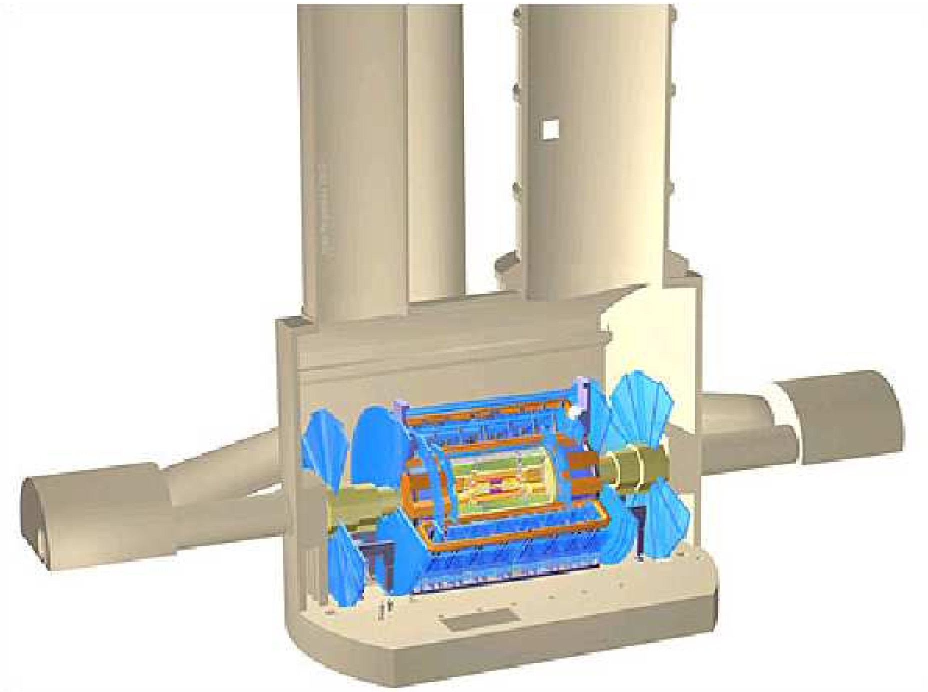

Figure 5.3: Cosmic rays penetrate the ATLAS cavern and sector 13 from the two shafts.

5.4 Evaluation of noise level

The aim of a noise test is to measure the quality of the single drift tube and the related electronics, by calculating the noise frequency of each single channel. Actually, noise frequency are calculated also in cosmic runs, even though two slightly different definition are given.

In a noise test a software random trigger is used to open the matching window, uncorrelated with cosmics crossing the tube. The TDC spectrum is therefore expected to be flat (i.e. hits occur with equiprobable drift times), as the one shown in Fig. 5.4.

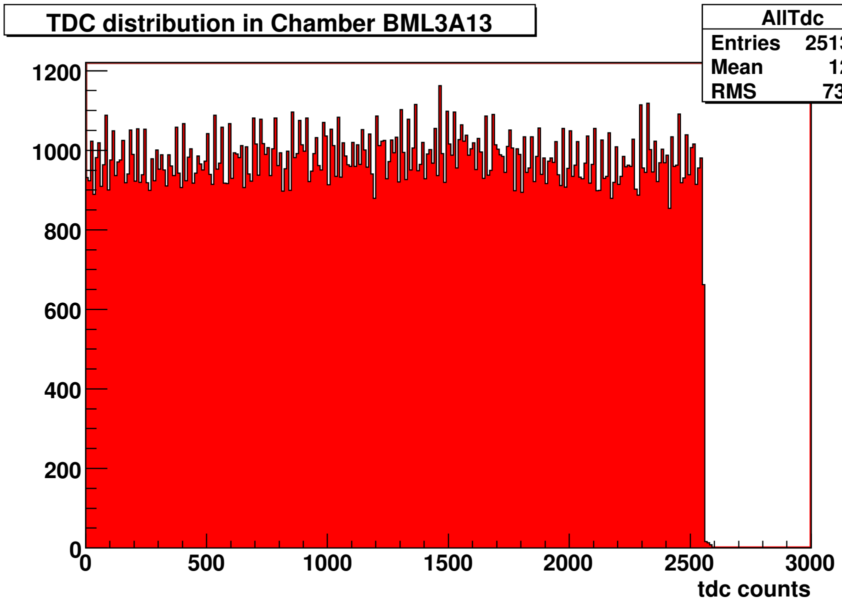

Figure 5.4: TDC flat distribution for a noise test.

The tube noise frequency is calculated by normalizing the number of entries in its own TDC spectrum (i.e. the number of hits occurred in this tube) at the total number of recorded events, according to the following (5.1):

$$freq(kHz) = \frac{entries}{events} \cdot \frac{10^6}{time\ window(ns)} \tag{5.1}$$

Since only the number of entries is dependent on the tube, while the number of events and the time window width (in this set-up 2500 TDC counts = 2500·25/32 ns) are constant, noisy tubes can be easily recognized by looking at the occupancy plots, as the one shown in Fig. 5.5.

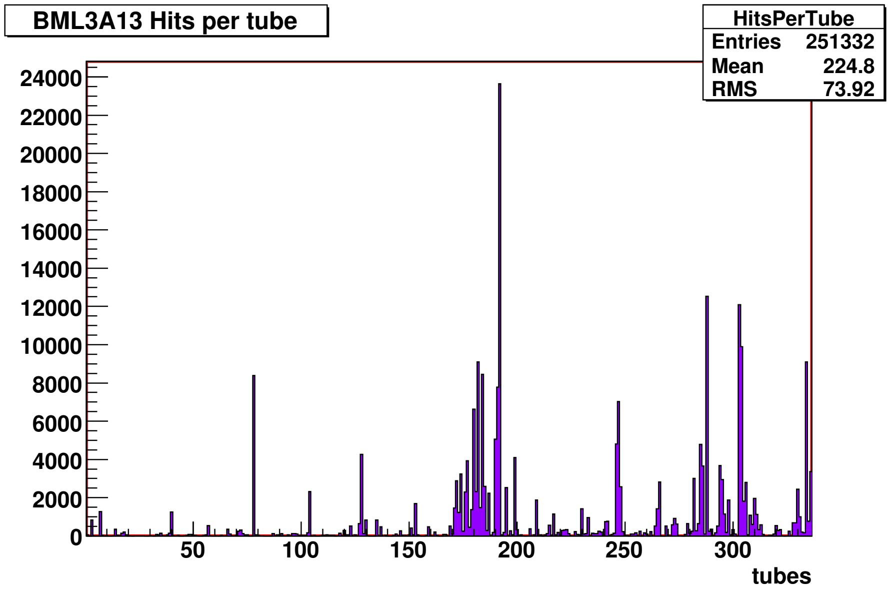

Figure 5.5: Occupancy plot (number of hits per tube) in a noise test.

In a cosmic run, the evaluation of noise level is still based on the drift time distribution, which shows the typical TDC profile for the Ar-CO_2 mixture, as shown in Fig. 5.6a. Noise hits occur at random times, since they are not correlated to a physical particle (muon) crossing the tube: that's why they are spread out all over the integration time window. In particular, since physical hits occurs in the region between t_0 and t_{max}, noise hits can be easily identified, by counting hits preceding the leading edge and following the trailing edge. Such these noise counts must be normalized to the total number of events and to the non-physical time window (hits occurring with drift times lower than t_0 and higher than t_{max}) that is, in principle, different from tube to tube. The following formula (5.2) has been used to calculate the frequency in kiloHertzs.

$$freq(kHz) = \frac{noise\ counts}{events} \cdot \frac{10^6}{non - physical\ time\ window(ns)} \tag{5.2}$$

Two different sources of noise must be taken into account. Noise can be due to some defects of the tube itself, which modify the electric field and cause spourious discharges in the gas volume, or to the ASD channel it is connected to. This can be easily identified in a cosmic run by selecting hits over a prefixed ADC threshold. A typical ADC spectrum (see Fig. 5.7a), in fact, is a two peak distribution. The former, that is the one at lowest value, is the so-called *pedestal*; hits belonging to the pedestal are noise hits, not correlated with a muon crossing the tube. The

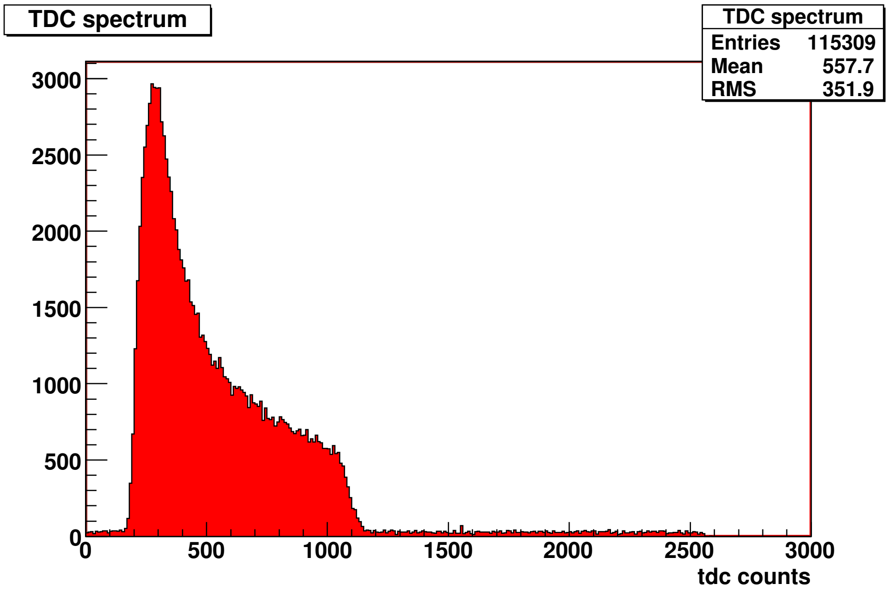

(a) good chamber

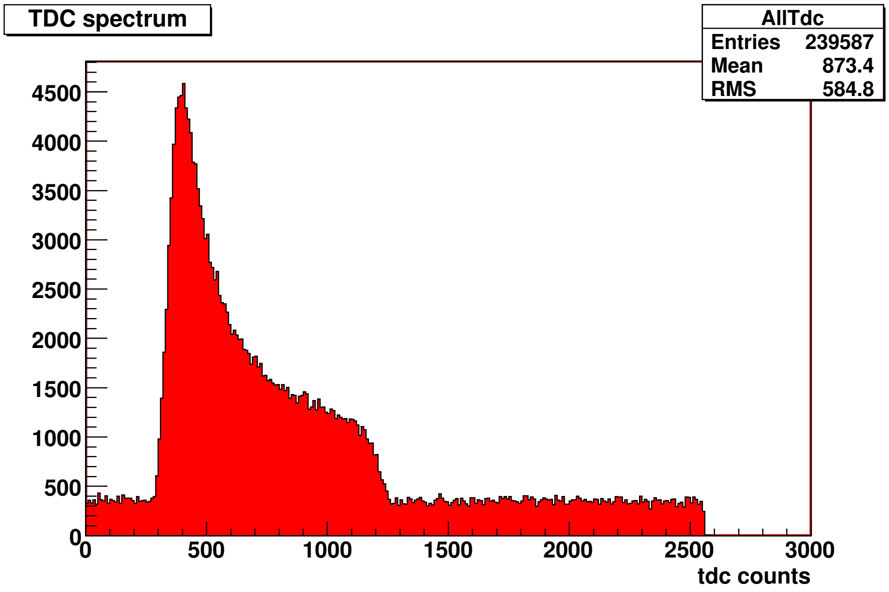

(b) noisy chamber

Figure 5.6: TDC distribution in a cosmic run for a good chamber (a) and for a very noisy one (b).

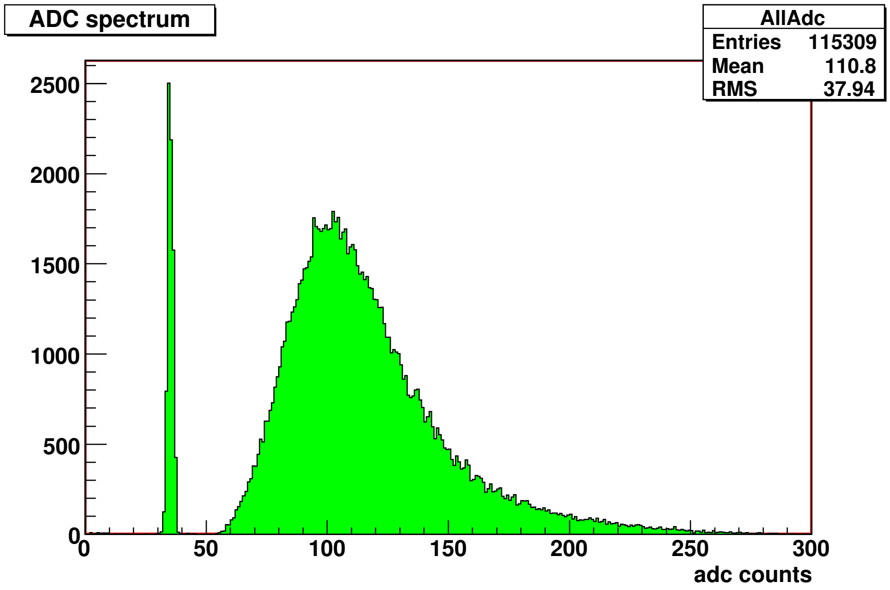

(a) ADC spectrum

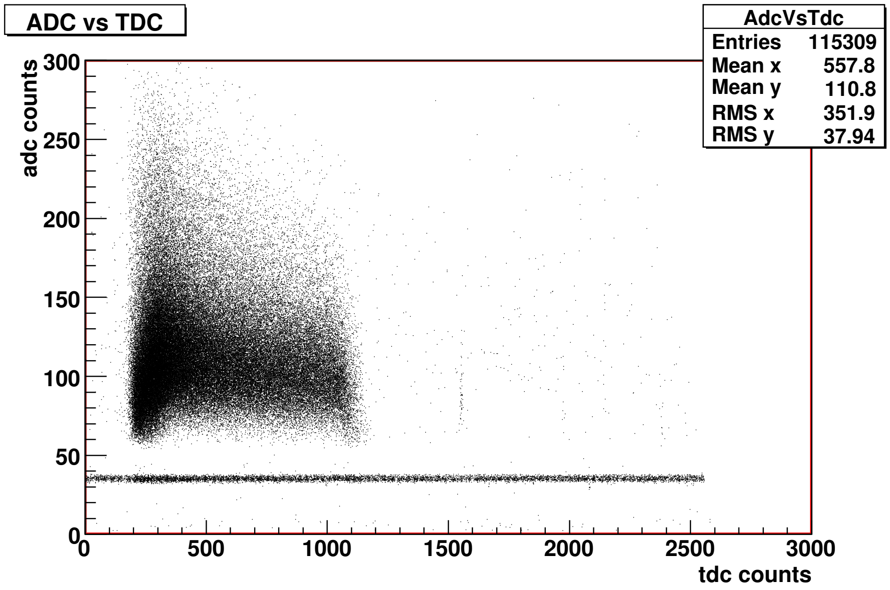

(b) ADC vs TDC distribution

Figure 5.7: Typical ADC spectrum (a) and ADC vs TDC distribution for a good chamber.

second peak is the out-and-out collected charge distribution.

The discrimination between physical and noise hits is also visible through the ADC versus TDC distribution: as shown in Fig. 5.7b, if hits with drift times lower than t_0 and higher than t_{max} are noise hits, they are associated with ADC values on the pedestal ($\sim$35 ADC counts in this example). Indeed, since there is not any time correlation, noise hits are spread out all over the time window (flat horizontal line at 35 adc counts in the picture). Hits from real tracks, instead, arrive within the physical time window, and they are associated with ADC value higher than the pedestal. The ADC spectrum for a noisy chamber and the corresponding correlation with drift time distribution are shown for comparison in Fig. 5.8.

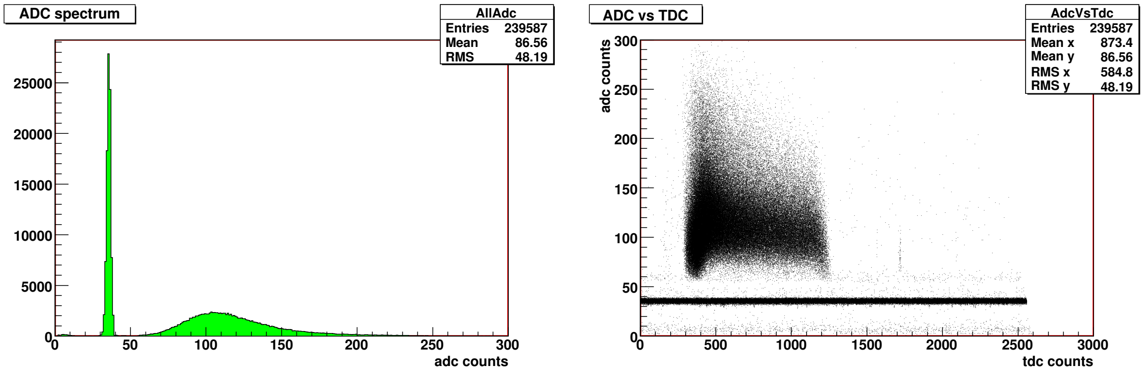

(a) ADC spectrum (b) ADC vs TDC distribution

Figure 5.8: Typical ADC spectrum (a) and ADC vs TDC distribution for a noisy chamber.

If hits with ADC value higher than the pedestal are selected, the ASD noise is removed, and spectra like the one shown in Fig. 5.6b appear now as the one in Fig. 5.9.

A single tube is flagged as “noisy” if noise level is higher than 10 kHz. This limit is fixed from the simulation of ATLAS cavern background, consisting mainly of thermalised slow neutrons, long-lived K^0s and low-energy photons escaping the calorimeters and the forward beam and shielding elements. This 10 kHz threshold also fixes the limit for a mezzanine ($\sqrt{24}\cdot$10 kHz$\simeq$50 kHz) and for a full chamber ($\sqrt{tubes}\cdot$10 kHz). In particular “hot tubes” are defined as the ones with frequency higher than 50 kHz.

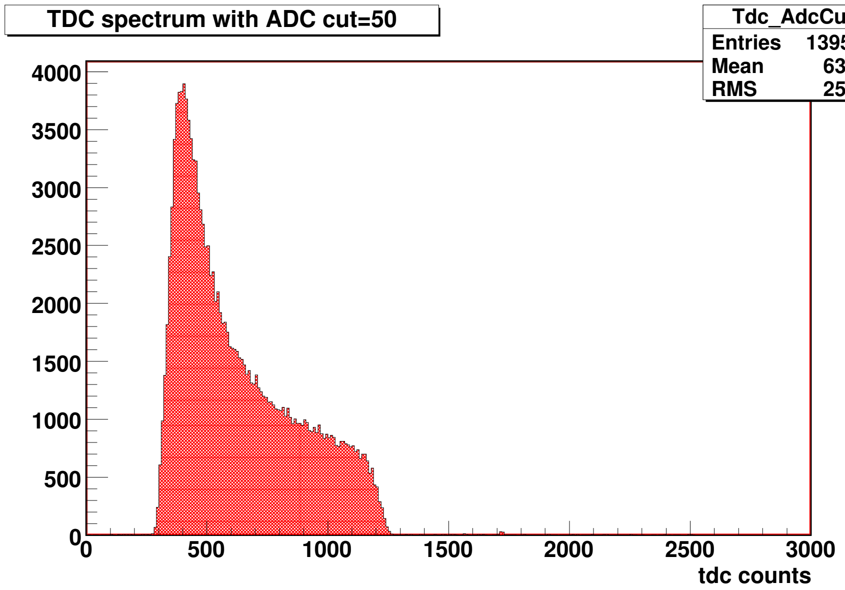

Figure 5.9: TDC distribution for the noisy chamber in Fig. 5.6(b) with ADC cut at 50 adc counts.

5.5 Noise runs: threshold scan

MDT chamber electronic tests are done both with high voltage on (HV on) at standard 3080 V, and high voltage off (HV off). When HV is off, no multiplication processes can occur in the gas volume, since no electric field can accelerate ionization electrons towards the anode wire. If hits are registered when HV is off, this means that it is only electronics to generate them.

A threshold scan was performed, to choose the settings for the ASD chain, in particular the discriminator threshold. As stated in [21], in order to operate the ASD chip at 5σ above the thermal noise level (75 Hz), the nominal threshold must be set to V_{thr}=-40 mV.

For any particular threshold settings, in fact, we expect to get random noise hits which are Poisson distributed in time and a Gaussian function of threshold:

$$R(x) = R_0 \cdot e^{-\frac{(x-V_{off})^2}{2\cdot\sigma^2}} \tag{5.3}$$

where R_0 is the maximum rate of hits, V_{off} is the measured offset voltage of the channel, σ is the Gaussian width of ASD noise distribution and x is the threshold setting. The parameters R_0, V_{off} and σ are extracted during production chip testing for each channel and placed in the production database.

Both tests at production sites and simulation studies with `GARFIELD` [57], suggest that the noise level decreases with an exponential law with the increasing threshold[2]. In particular, it is found that noise rate is reduced by a factor 1/e every 2-2.5 mV.

The threshold scan was performed starting from -34 mV up to -48 mV, in steps of 2 milliVolts, both with HV on and off. Table 5.1 shows the time-ordered list of the acquired runs.

For each run, the noise level per tube was calculated as described in (5.1). Figures 5.10a and 5.10b show the exponential trend as a function of the threshold, for a sample tube in BIL2A13. No major differences are observed between the HV on and HV off distributions. Cumulative results for the whole set of chambers analyzed are shown in Fig. 5.11.

run number	**threshold**	**HV status**
100244	-36 mV	on
100246	-34 mV	on
100249	-38 mV	on
100250	-40 mV	on
100251	-42 mV	on
100252	-44 mV	on
100253	-46 mV	on
100254	-48 mV	on
100255	-48 mV	off
100256	-46 mV	off
100257	-44 mV	off
100258	-42 mV	off
100259	-40 mV	off
100260	-38 mV	off
100262	-34 mV	off
100265	-36 mV	off

Table 5.1: List of time-ordered runs for the threshold scan at HV on and HV off.

---

[2] Actually, with the increasing absolute value, since the negative ASD threshold is related to the number of electrons collected at the anode wire.

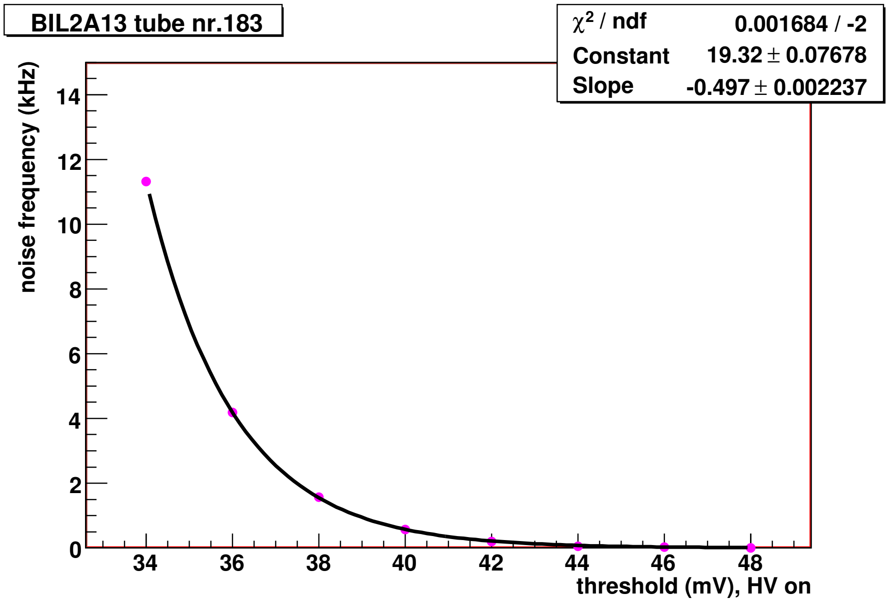

(a) HV on

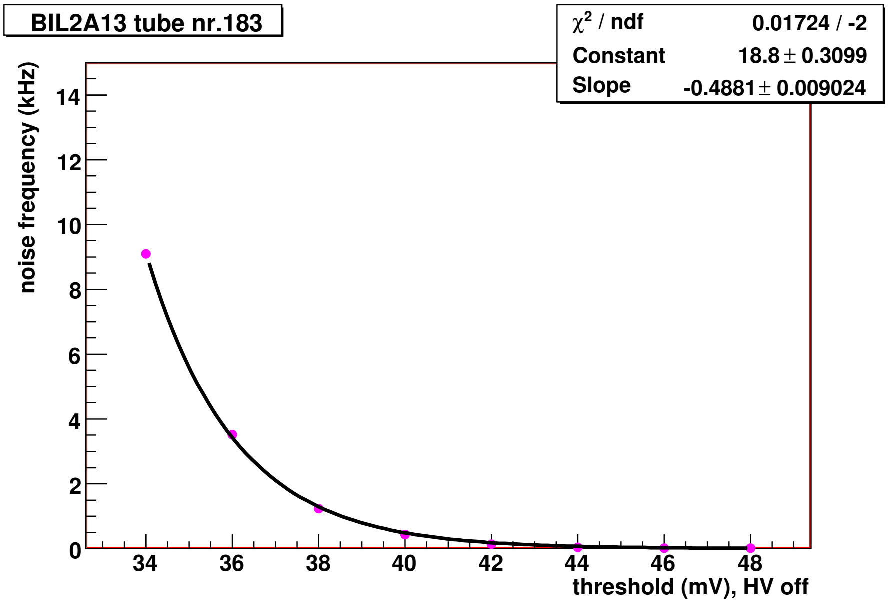

(b) HV off

Figure 5.10: BIL2A13: noise level decreases exponentially at higher threshold for the sample tube 183.

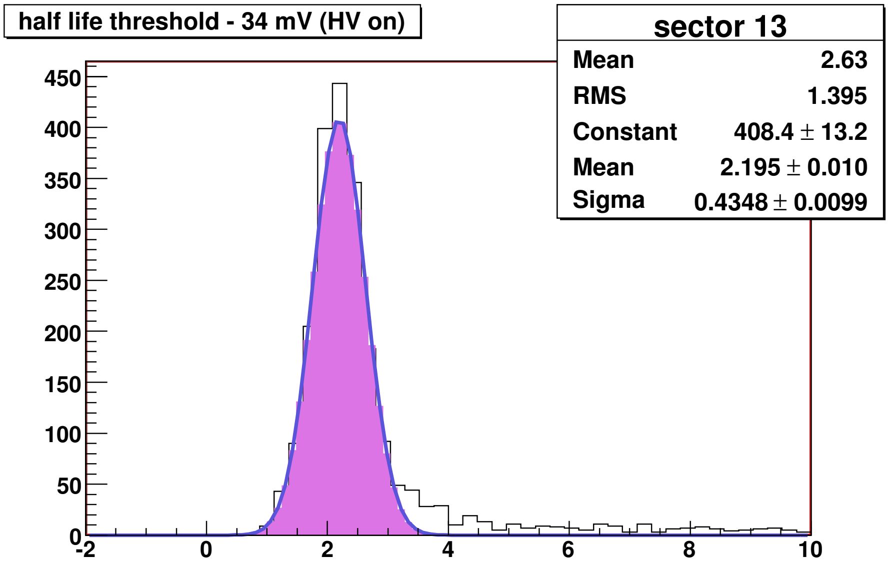

(a) HV on

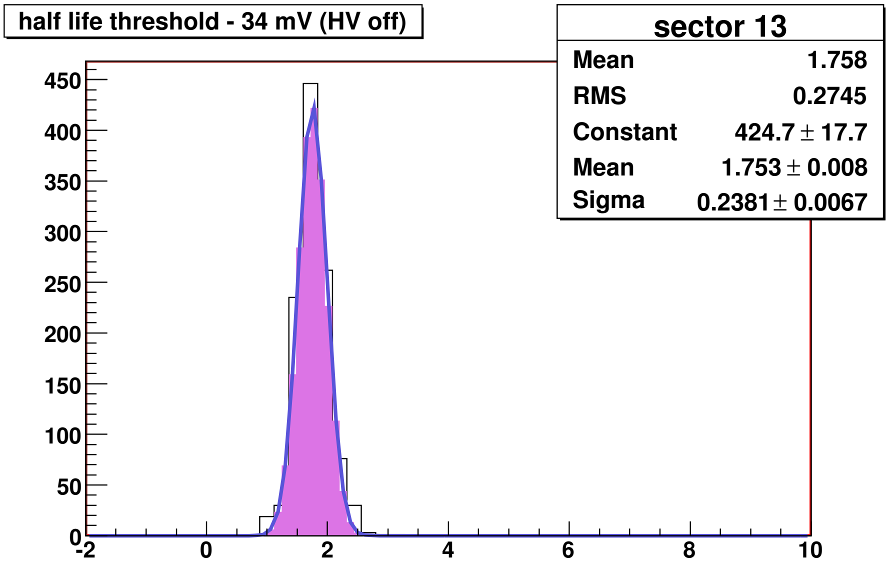

(b) HV off

Figure 5.11: Difference between the half life corresponding threshold and the initial one (34 mV) with HV on (a) and HV off (b) for all the chambers in sector 13.

5.6 Cosmic runs: the magnet test

The November 2006 commissioning activities have been really interesting for the muon spectrometer community. During the cosmic ray data taking (November 18^{th} to 20^{th}), the barrel toroid magnet system was fully operating for the very first time. All the eight coils (see Fig. 5.12) were first cooled down for about six weeks in July-August to -269 °C (4.8 K) and then powered up step-by-step in successive test sessions to 21 kA. This is 0.5 kA above the current required to produce the nominal magnetic field (3.9 T at 20.5 kA). Afterwards, the current was safely switched off and the stored magnetic energy of 1.1 GJ was dissipated in the cold mass, raising its temperature to a safe -218 °C (55 K).

Sector 13 magnet-on test was carried out during a weekend, with some few runs acquired at 18 kA and the rest at the nominal current of 20.5 kA. As it is expected, the magnetic field was not constant all over the spectrometer: Fig. 5.13 and [58] shows it is stronger very close to the coils ($\sim$1 T) and degrades with the distance from them. That's why different chambers experience different fields. Moreover, since the main component of the field is parallel to the MDT wires, the intensity of the magnetic field is lower in the mid position of the wire and higher at the tube edges. Typical values are 0.7 T for BILs, 0.6 T for BMLs and 0.4 T for BOLs.

5.6.1 Analysis results

This cosmic data set aroused curiosity in the collaboration, since for the first time the ATLAS subdetector performances have been monitored in presence of the magnetic field. For the first time, such an apparatus was tested in a totally new and challenging environment, much more complex with respect to the test beam session carried out in the past years. Different parameters should have been monitored to have a clear view of the response of the MDTs, and this was not the case for this magnet session. It was not intended as a well designed and organized test for MDTs plus the magnet system; rather we, as muon spectrometer community, took advantage from the fact that the barrel toroid was switched on, and took a look at the general behavior of the system. These results therefore, even if they are in complete agreement with other studies presented internally at the muon community, would just offer an overview of the sector 13 chamber performances.

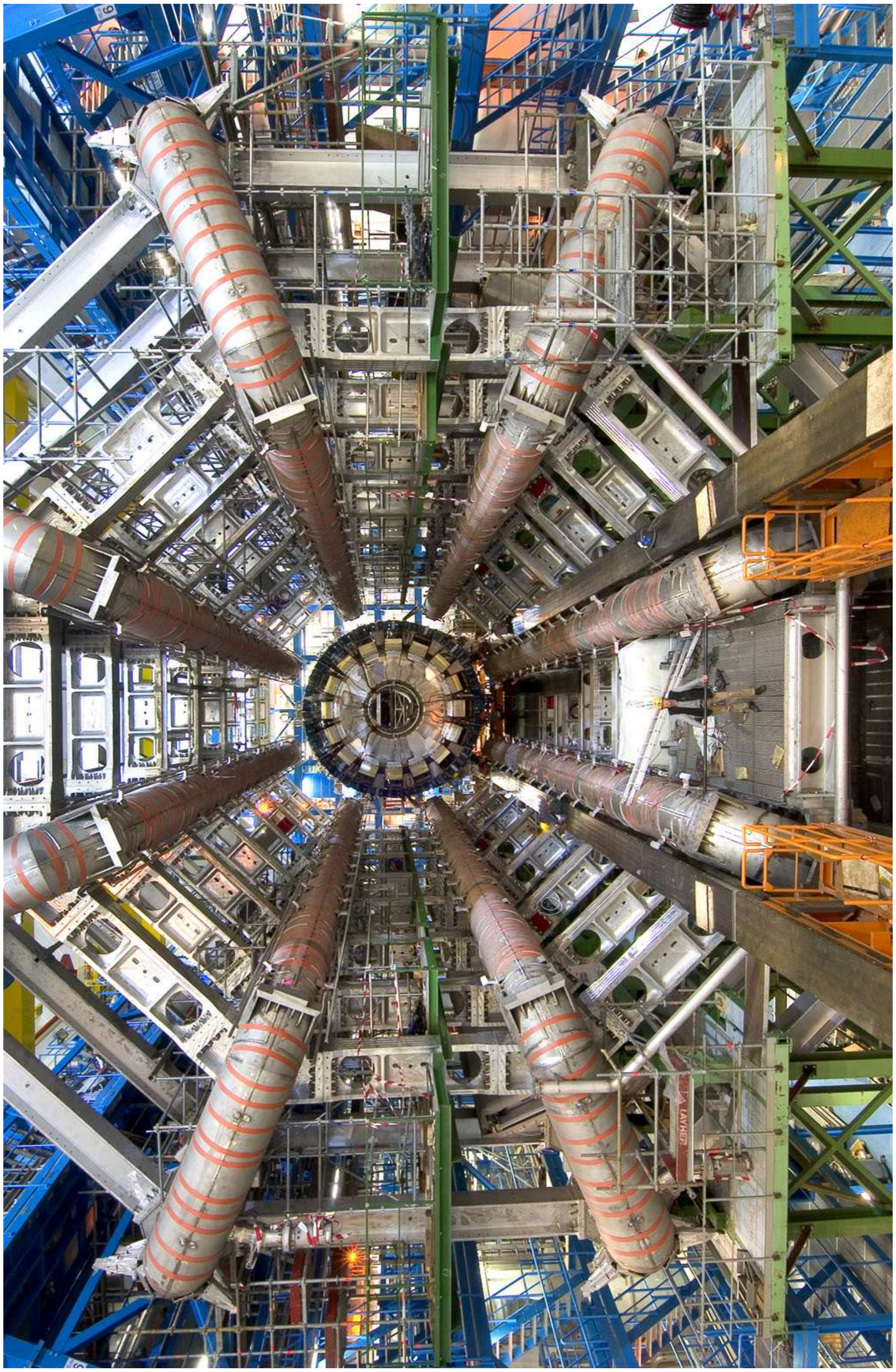

Figure 5.12: The ATLAS barrel toroid coils.

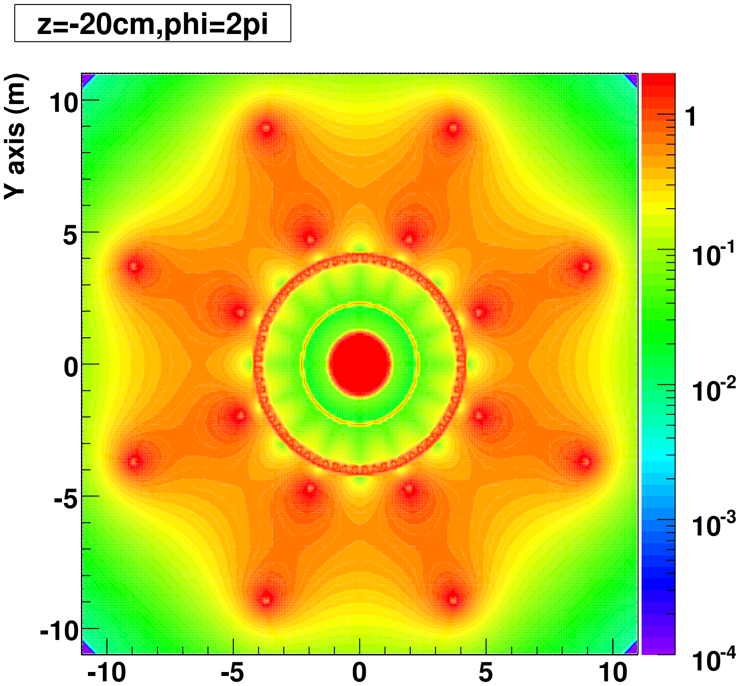

(a) full spectrometer

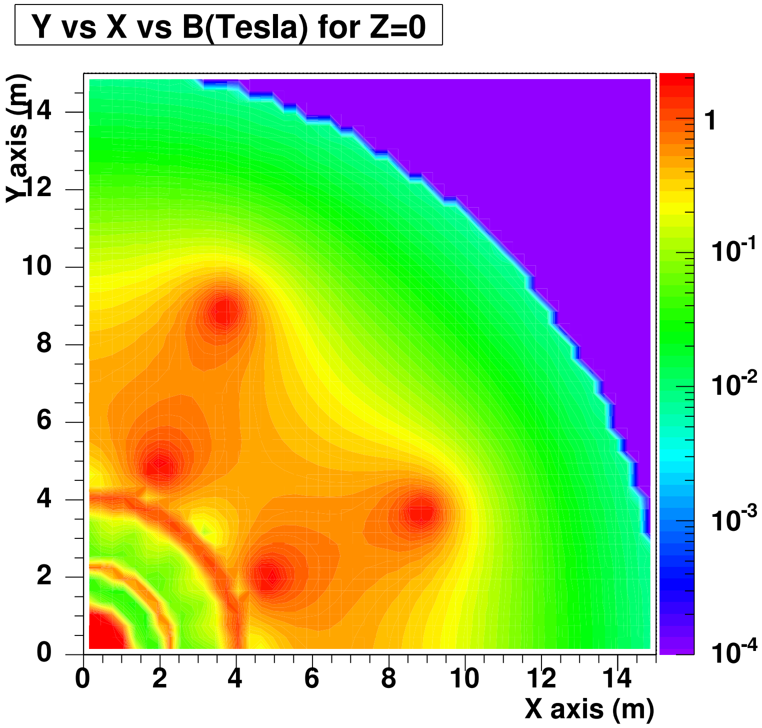

(b) a quarter of the spectrometer

Figure 5.13: Magnetic field in the ATLAS muon spectrometer.

Drift properties

Because of the Lorentz law, in presence of a magnetic field, charged particles are deviated from their trajectory and follow a curved path into the spectrometer, allowing the measurement of muon momenta. But also inside the MDTs, the drift path of the ionization electrons is bent and resulting drift times are therefore longer. In this section, some results from the monitoring of drift properties are reported, both with the magnetic field on and off.

The list of analyzed runs is reported in Tab 5.2. The first run (100335) was chosen as reference at magnet off, then other runs have been chosen with magnet on at 18 kA and 20.5 kA (nominal current). Some other measurement have been carried out when the coils were switched off again, trying to isolate magnetic field effect on the MDTs.

run number	B field status
100335	off
100336	off
100339	on at 18 kA
100340	on at 18 kA
100342	on at 18 kA
100343	on at 18 kA
100368	on at 20.5 kA
100373	on at 20.5 kA
100375	on at 20.5 kA
100377	on at 20.5 kA
100380	off
100381	off
100384	off
100390	off
100395	off
100399	off

Table 5.2: List of time-ordered runs used in the analysis.

None of this run provides the sufficient statistics to fill a good TDC spectrum per single tube; 10000 and 30000 entries at least are required for a reasonable fit of t_0 and t_{max} respectively [59]. The best information can be extracted at chamber level and, in some case, looking at the cumulative TDC spectrum per mezzanine card. The `MDTGnam` package was used to decode data and fill relevant histograms: offline ROOT [53] macros have been developed to fit both the leading and the trailing edges. The already cited functions (3.1) and (3.2) were used to retrieve t_0 and t_{max}. At first, t_0 stability all over the data taking was studied. The t_0 parameter is not expected to have any dependence on the magnetic field, since it represents the offset in drift time calculation due to electronics and cabling. If differences in t_0 are observed, they are due to some re-initialization of the chambers and of the RPC timing.

The t_0 of three sample chambers is reported in Fig. 5.14: two distributions are clearly visible, with the same spread of about 200 TDC counts for the different chambers between the last run with magnet on at 18 kA to the first run at 20.5 kA. It is worth to stress that the two runs are not immediately subsequent: more than half a day spent between them, and lot of settings could have been changed. Data taken in the meantime cannot be used, since the magnet condition was not stable. In addition, the jump cannot be ascribed to the magnetic field: the former t_0 distribution is valid both for two magnet-off runs and for magnet-on at 18.5 kA; the latter, for 20.5 kA magnet-on runs and, again, for magnet-off runs. As an example, a magnified view on BIL1A13 (Fig. 5.14a) is reported in Fig. 5.15.

The maximum drift time, instead, strictly depends on the magnetic field, which is responsible for drift electrons to bend their path in the gas volume. Maximum drift times should results longer, if environmental conditions like temperature, gas pressure and composition are monitored and kept constant. Detailed information about the environmental parameters are not available; sector 13 chambers were not provided with their own B-field probes, but values have been extrapolated from sector 6 measurements.

All the sector 13 chambers show wider drift time spectra when the field is on, even if differences between magnet-off and magnet-on values change from chamber to chamber: as already stated, different chambers experience different magnetic field, because of their position with respect to the coils. In particular, BOLs experience the lower field (∼0.4 T), resulting in a quite constant trend with respect to the other chambers (Fig. 5.16).

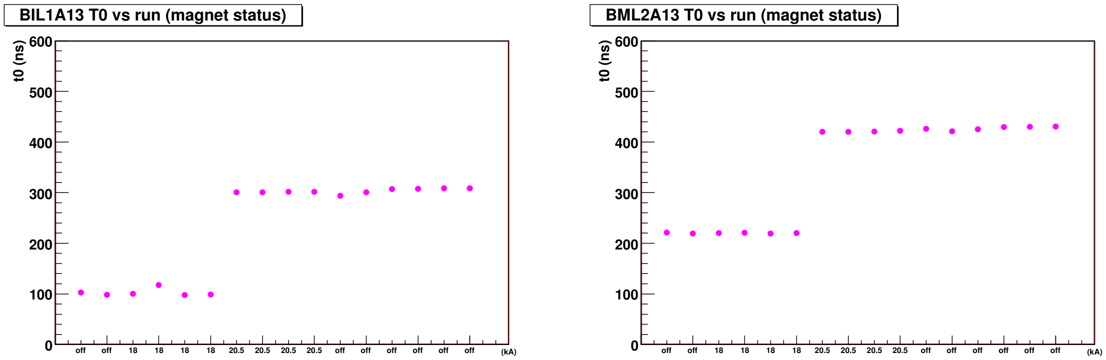

(a) BIL1

(b) BML2

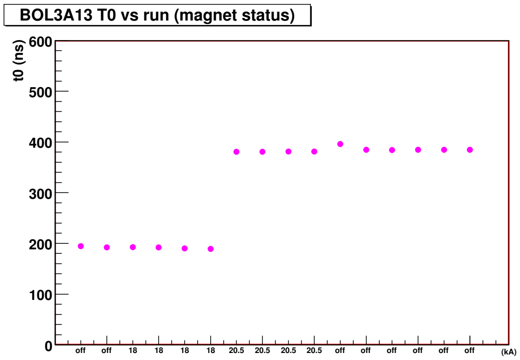

(c) BOL3

Figure 5.14: T_0 versus run for three chambers by way of example.

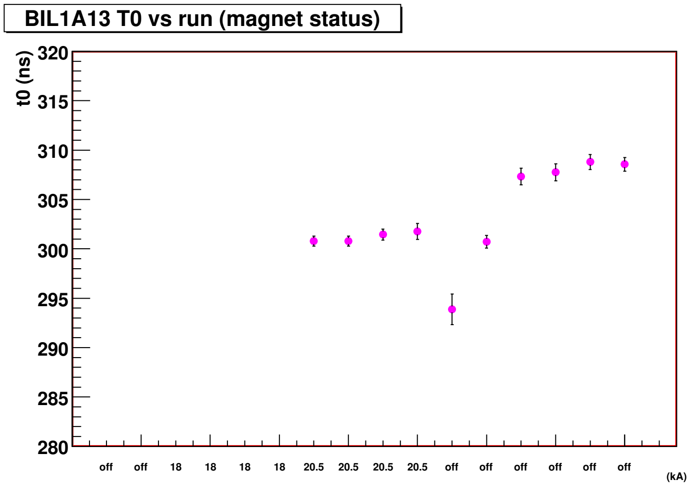

Figure 5.15: Magnified view of BIL1A13 t_0 versus run distribution.

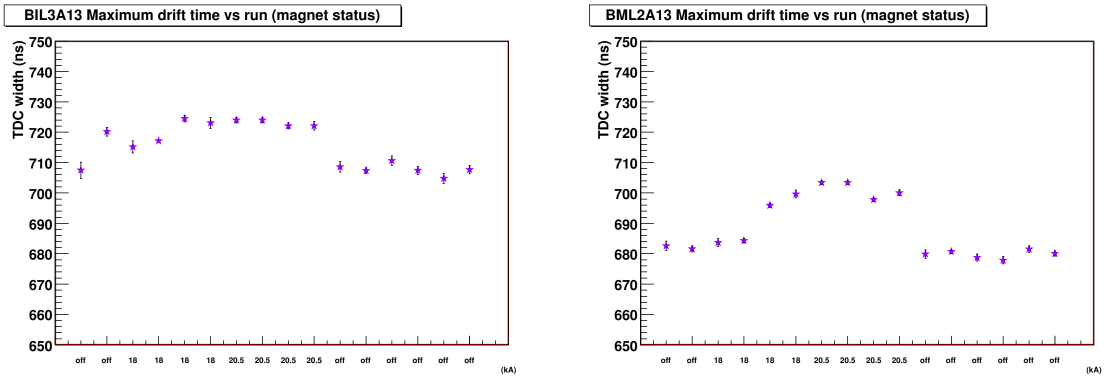

(a) BIL3

(b) BML2

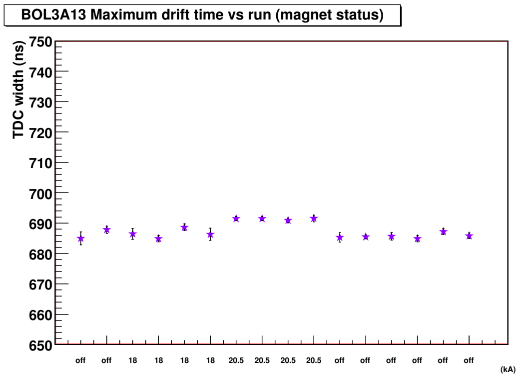

(c) BOL3

Figure 5.16: Maximum drift times as a function of time ordered runs, with magnetic field off, on at 18 kA and on at 20.5 kA for three chambers as an example.

Noise level

Noise level has been evaluated for each run, according to the definition given in Sect. 5.4. A list of dead[3] and noisy tubes per each chamber is shown in Tab. 5.3, together with the noise frequency measured at the first run.

Figure 5.17 shows noise level for some chambers chosen as example. The noise level for the worst tube and the mean value calculated on the remaining good tubes are shown for comparison. The heaviest contributes at the total noise level per chamber are given from tube n°239 in BIL1A13 (Fig. 5.17a) and from tube n°256 in BIL2A13 (Fig. 5.17b). Chamber BML3A13 mean value, instead, is only reduced by the 25% if tubes with noise frequencies higher than 15 kHz are subtracted.

---

[3] In this set-up, dead tubes are defined as tubes with zero entries.

chamber	dead tubes	worst tube	frequency (kHz)
BIL1A13	no	239	110
BIL2A13	no	256	40
BIL3A13	no	no	0
BML1A13	no	no	0
BML2A13	no	192	15
BML3A13	no	192	70
BOL1A13	1	40	30
BOL2A13	no	no	0
BOL3A13	no	no	0

Table 5.3: List of dead and noisy tubes for each chamber.

Actually, the chamber is globally noisier than all the others.

Anyway, in a cosmic test, ASD noise hits can be discriminated from noise hits induced by a bad behavior of the tube itself. As stated in Sect. 5.4, the ASD noise can be subtracted by choosing hits which exceed the ADC cut at 50 counts. The statistic can be quite reduced (see as an example Fig. 5.6b and Fig. 5.9) if the ASD noise component is relevant. Three runs have been chosen to calculate the ASD noise percentage: the magnet-off 100336, a 20.5 kA magnet-on run (100375) and the last run 100399. Table 5.4 reports these percentages for the four very noisy tubes found: it's clear that they are all ASD noisy. The ASD chip settings will therefore be tuned properly, in order to reduce the cahmber occupancy.

chamber	tube n°	freq. (kHz)	ASD percentages
BIL1A13	239	110	96.00, 93.37, 93.67
BIL2A13	256	40	99.87, 99.85, 99.98
BML3A13	192	70	99.97, 99.97, 99.97
BOL1A13	40	30	99.67, 99.72, 99.68

Table 5.4: List of the ASD noise percentages in three different runs for the four noisiest tubes of the sector 13.

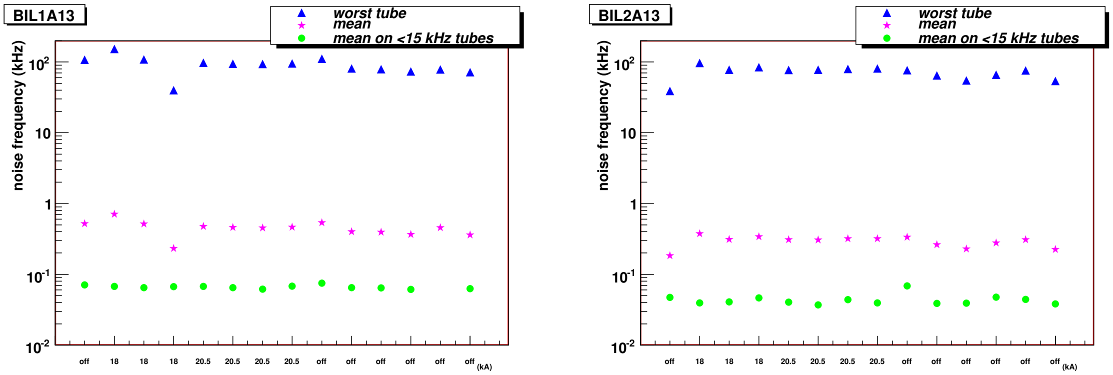

(a) BIL1

(b) BIL2

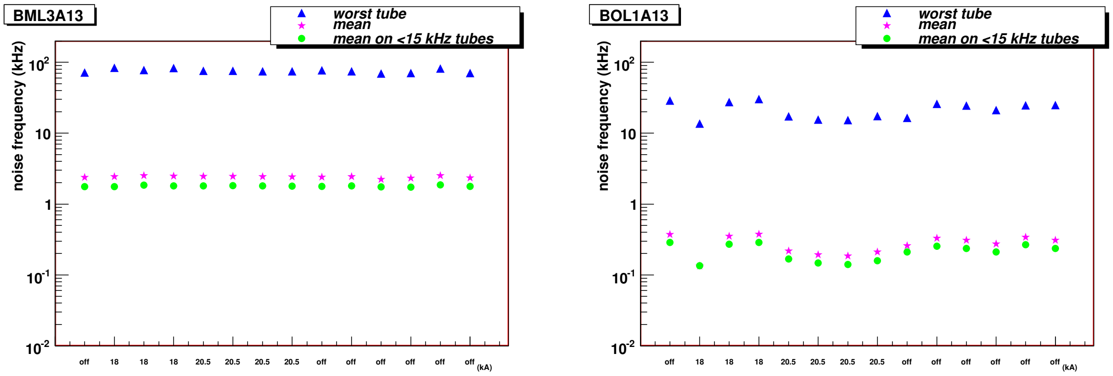

(c) BML3

(d) BOL1

Figure 5.17: Noise level for runs with magnetic field off, on at 18 kA and on at 20.5 kA. Noise levels for the overall chambers is reported together with the noise level for the noisiest tube and the mean value on the good tubes.

5.7 Summary

The ATLAS detector commissioning is going to be completed by the first half of 2008. In particular, the muon spectrometer is testing last sectors. Commissioning activities are crucial to set-up an apparatus such as ATLAS, where so many subdetectors must be integrated and cooperate at best. The MDT system must be tested from the basic element, the single drift tube assembled at the production sites, to the full chambers in their final position on the ATLAS frame. Different checks are performed to ensure the reliability of each single channel, such as noise test and cosmic data acquisition.

Among the routine activities, special attention must be paid to the sector 13 commissioning, where for the first time, 13 chambers were integrated in the DAQ chain to acquire cosmic data in the ATLAS cavern. The test was successfull and the system fully operating. Moreover, in November 2006, a barrel toroid magnet test was carried out by the magnet community. The eight barrel coils worked at their nominal current (20.5 kA), providing the 3.9 T B-field.

The muon community took advantage from this test, and special cosmic data runs have been acquired, to have a first look at MDT and RPC chamber behavior in presence of the magnetic field. Despite a lot of parameters need to be monitored with such a set-up, global aspects of both the subdetectors have been studied. As shown in this thesis, the drift parameters and the noise level of the MDT chambers have been monitored; the detectors seem to react as we expected.

Appendix A

The MDTGnam C++ classes

A.1 The Chamber class

```
#ifndef _Chamber_h
#define _Chamber_h

#include <string>
#include <vector>
#include <stdio.h>
#include <stdlib.h>
#include <fstream>
#include <iostream>

using namespace std;

class Chamber
{

public:
  string name;
  unsigned int MLayers;
  unsigned int MezzPerML;
  unsigned int MezzTypeML1;
  unsigned int MezzTypeML2;
  unsigned int ZeroMezzML;
  unsigned int mrodId;
  unsigned int csm;
  unsigned int sdid;
  unsigned int withZ;
  bool found;
  bool OnMap;
  bool Geo;
  unsigned int TubesPerLayer;
  unsigned int LayersPerML;
  unsigned int TubesPerML;
  unsigned int TotTubes;
  unsigned int TotMezz;
  unsigned int TotLayers;
  unsigned int Id;
  unsigned int AtlasId;
```

```
  unsigned int TotHits;
  vector<unsigned int> Hits;
  vector<unsigned int> NoiseCounts;
  vector<unsigned int> NoiseElxCounts;
  vector<unsigned int> NoiseAdcCut;
  vector<unsigned int> NoiseCutAdc;
  vector<unsigned int> NoiseCountsTdc;
  vector<float> NoiseFreq;
  vector<float> NoiseFreqElx;
  vector<float> NoiseFreqAdc;
  vector<float> NoiseAdcFreq;
  vector<float> NoiseFreqTdc;
  float t0[2];
  float tmax[2];
  float adc_cut;
  float norm[2];
  string StName;
  string StEta;
  unsigned int StPhi;
  unsigned int Sector;
  unsigned int IDinSector;

  void make_geo();
  void GetAthenaId();
  unsigned int CreateAtlasId(unsigned int tube);
  float make_norm(unsigned short int);

  Chamber();
  ~Chamber();
};

#endif
```

A.2 The MdtEvent class

```
#ifndef __MdtEvent__
#define __MdtEvent__
#include <TH1.h>
#include <map>

const UInt_t MAXHIT=2000;
const UInt_t MAXERROR=500;
const UInt_t MAXRODNUMBER=1500;
const UInt_t MAXRODSIZE=5000;

class MdtEvent
{
 private:
 public:

  UInt_t NRods;
```

```
  UInt_t TotalNRods;
  UInt_t NHits;
  UInt_t BunchCrossId;
  UInt_t MaskedHits;

  UInt_t *SubDetId;
  UInt_t *RodSize;
  UInt_t *BCId;

  UInt_t *HitSubDetId;
  UInt_t *MrodId;
  UInt_t *Mrod;
  UInt_t *CSM;
  UInt_t *Tdc;
  UInt_t *Channel;
  UInt_t *Time;
  UInt_t *Width;
  int *Chamber;
  UInt_t *MLayer;
  UInt_t *Layer;
  UInt_t *Tube;

  UInt_t NError;
  UInt_t *ErrCode;

  void EventReset();
  void DoMapping();

  MdtEvent();
  ~MdtEvent();
};
#endif
```

Appendix B

The MROD data format

B.1 The structure of the MROD data

In the table below words marked as follows:

H1-H9, NSE, NDE, SBP :	DAQ specific header/trailer words
`MSE1–MSEn` :	MROD specific Status words
BOB and EOB:	MROD specific header/trailer words
LWC and BOL, TLP, TWC :	CSM-Link specific header/trailer words
BOT, TD, EOT :	TDC header, data and trailer words
words labelled as **BOT, EOT :**	may be “zero-suppressed” (no TDC data).
words labelled as **EOT :**	may be “trailer-suppressed” (superfluous EOT).

<table>
<tr><td></td><td>31</td><td>30</td><td>29</td><td>28</td><td>27</td><td>26</td><td>25</td><td>24</td><td>23</td><td>22</td><td>21</td><td>20</td><td>19</td><td>18</td><td>17</td><td>16</td><td>15</td><td>14</td><td>13</td><td>12</td><td>11</td><td>10</td><td>9</td><td>8</td><td>7</td><td>6</td><td>5</td><td>4</td><td>3</td><td>2</td><td>1</td><td>0</td></tr>
<tr><td>H1</td><td>1</td><td>1</td><td>1</td><td>0</td><td>1</td><td>1</td><td>1</td><td>0</td><td colspan="24">ROD Start of Header marker (= 0xEE1234EE)</td></tr>
<tr><td>H2</td><td>0</td><td>0</td><td>0</td><td>0</td><td>0</td><td>0</td><td>0</td><td>0</td><td colspan="24">ROD Header size (= 0x00000009)</td></tr>
<tr><td>H3</td><td colspan="16">Format Version Number (Major = 0x0300)</td><td colspan="16">Format Version Number (Minor =0x0000)</td></tr>
<tr><td>H4</td><td>0</td><td>0</td><td>0</td><td>0</td><td>0</td><td>0</td><td>0</td><td>0</td><td colspan="8">Sub-detector ID</td><td colspan="16">MROD Module ID</td></tr>
<tr><td>H5</td><td colspan="8">Run Type</td><td colspan="24">Run Sequence number</td></tr>
<tr><td>H6</td><td colspan="8">ECR Identifier</td><td colspan="24">Level1 Identifier</td></tr>
<tr><td>H7</td><td>0</td><td>0</td><td>0</td><td>0</td><td>0</td><td>0</td><td>0</td><td>0</td><td>0</td><td>0</td><td>0</td><td>0</td><td>0</td><td>0</td><td>0</td><td>0</td><td>0</td><td>0</td><td>0</td><td>0</td><td colspan="12">Bunch Crossing Identifier</td></tr>
<tr><td>H8</td><td>0</td><td>0</td><td>0</td><td>0</td><td>0</td><td>0</td><td>0</td><td>0</td><td>0</td><td>0</td><td>0</td><td>0</td><td>0</td><td>0</td><td>0</td><td>0</td><td>0</td><td>0</td><td>0</td><td>0</td><td>0</td><td>0</td><td>0</td><td>0</td><td colspan="8">Trigger Type ID</td></tr>
<tr><td>H9</td><td>0</td><td>0</td><td>0</td><td>0</td><td>0</td><td>0</td><td>0</td><td>0</td><td colspan="24">Detector Event Type (= 0)</td></tr>
<tr><td colspan="33"></td></tr>
<tr><td>BOB</td><td>1</td><td>0</td><td>0</td><td>0</td><td>0</td><td>0</td><td>0</td><td>0</td><td colspan="24">L1ID</td></tr>
<tr><td colspan="33"></td></tr>
<tr><td>LWC</td><td>1</td><td>0</td><td>0</td><td>0</td><td>0</td><td>0</td><td>0</td><td>1</td><td>0</td><td>0</td><td>0</td><td>0</td><td colspan="4">ECNT</td><td colspan="16">Link Word Count</td></tr>
<tr><td>BOL</td><td>0</td><td>0</td><td>0</td><td>1</td><td>1</td><td>0</td><td>0</td><td>0</td><td colspan="8">BOL flags</td><td colspan="12">MROD number</td><td colspan="4">CSM Link 0</td></tr>
<tr><td>TLP</td><td>1</td><td>0</td><td>0</td><td>0</td><td>1</td><td>0</td><td>0</td><td>1</td><td>0</td><td>0</td><td>0</td><td>0</td><td colspan="20">TDC Link Present flags</td></tr>
<tr><td colspan="33"></td></tr>
<tr><td>BOT</td><td>1</td><td>0</td><td>1</td><td colspan="5">TDC 0</td><td colspan="12">ECNT</td><td colspan="12">BCID</td></tr>
<tr><td>TD</td><td>0</td><td>0</td><td>1</td><td>0</td><td>0</td><td>0</td><td colspan="2">JT</td><td colspan="24">Masked channels flags</td></tr>
<tr><td>TD</td><td>0</td><td>0</td><td>1</td><td>1</td><td>0</td><td>0</td><td colspan="2">JT</td><td colspan="5">Channel 0</td><td>T</td><td>E</td><td colspan="12">Coarse</td><td colspan="5">Fine</td></tr>
<tr><td>TD</td><td colspan="4">. . .</td><td>0</td><td>0</td><td colspan="2">JT</td><td colspan="24">. . . TDC data . . . (n words)</td></tr>
<tr><td>TD</td><td>0</td><td>0</td><td>1</td><td>1</td><td>0</td><td>0</td><td colspan="2">JT</td><td colspan="5">Channel 1</td><td>T</td><td>E</td><td colspan="12">Coarse</td><td colspan="5">Fine</td></tr>
<tr><td>EOT</td><td>1</td><td>1</td><td>0</td><td>0</td><td>0</td><td>0</td><td colspan="2">JT</td><td colspan="12">ECNT</td><td colspan="12">TDC WCNT (=5+n)</td></tr>
<tr><td>. . .</td><td colspan="4">. . .</td><td colspan="4">. . .</td><td colspan="24">. . . more TDC data (BOT+hits+EOT) . . .</td></tr>
<tr><td>BOT</td><td>1</td><td>0</td><td>1</td><td colspan="5">TDC 1</td><td colspan="12">ECNT</td><td colspan="12">BCID</td></tr>
<tr><td>EOT</td><td>1</td><td>1</td><td>0</td><td>0</td><td>0</td><td>0</td><td colspan="2">JT</td><td colspan="12">ECNT</td><td colspan="12">TDC WCNT (=2)</td></tr>
<tr><td>BOT</td><td>1</td><td>0</td><td>1</td><td colspan="5">TDC 2</td><td colspan="12">ECNT</td><td colspan="12">BCID</td></tr>
<tr><td>TD</td><td>0</td><td>0</td><td>1</td><td>0</td><td>0</td><td>0</td><td colspan="2">JT</td><td colspan="24">Masked channels flags</td></tr>
<tr><td>TD</td><td>0</td><td>0</td><td>1</td><td>1</td><td>0</td><td>0</td><td colspan="2">JT</td><td colspan="5">Channel 0</td><td>T</td><td>E</td><td colspan="12">Coarse</td><td colspan="5">Fine</td></tr>
<tr><td>TD</td><td>0</td><td>0</td><td>1</td><td>1</td><td>0</td><td>0</td><td colspan="2">JT</td><td colspan="5">Channel 1</td><td>T</td><td>E</td><td colspan="12">Coarse</td><td colspan="5">Fine</td></tr>
<tr><td>EOT</td><td>1</td><td>1</td><td>0</td><td>0</td><td>0</td><td>0</td><td colspan="2">JT</td><td colspan="12">ECNT</td><td colspan="12">TDC WCNT (=5)</td></tr>
<tr><td colspan="33"></td></tr>
<tr><td>TWC</td><td>1</td><td>0</td><td>0</td><td>0</td><td>1</td><td>0</td><td>1</td><td>0</td><td colspan="12">ECNT</td><td colspan="12">Trailer Word Count</td></tr>
</table>

	31	30	29	28	27	26	25	24	23	22	21	20	19	18	17	16	15	14	13	12	11	10	9	8	7	6	5	4	3	2	1	0
LWC	1	0	0	0	0	0	0	1	0	0	0	0	ECNT				Link Word Count															
BOL	0	0	0	1	1	0	0	0	0	0	0	0	0	0	0	1	MROD number												CSM Link 1			
TLP	1	0	0	0	1	0	0	1	0	0	0	0	TDC Link Present flags																			
BOT	1	0	1	TDC 3					ECNT												BCID											
TD	0	0	1	0	0	0	JT		Masked channels flags																							
TD	0	0	1	1	0	0	JT		Channel 0					T	E	Coarse												Fine				
TD	. . .				. . .				. . . more TDC data . . .																							
TD	0	0	1	1	0	0	JT		Channel 1					T	E	Coarse												Fine				
EOT	1	1	0	0	0	0	JT		ECNT												TDC WCNT											
TWC	1	0	0	0	1	0	1	0	ECNT												Trailer Word Count											

LWC	1	0	0	0	0	0	0	1	0	0	0	0	ECNT				Link Word Count															
BOL	0	0	0	1	1	0	0	0	0	0	0	0	0	0	0	1	MROD number												CSM Link 3			
TLP	1	0	0	0	1	0	0	1	0	0	0	0	TDC Link Present flags (=0)																			
TWC	1	0	0	0	1	0	1	0	ECNT												Trailer Word Count (=2)											

no TDC data at all !

	. . .				. . .				. . . more CSM data (header + TDC data + trailer) . . .																							

LWC	1	0	0	0	0	0	0	1	0	0	0	0	ECNT				Link Word Count															
BOL	0	0	0	1	1	0	0	0	0	0	0	0	0	0	1	1	MROD number												CSM Link 7			
TLP	1	0	0	0	1	0	0	1	0	0	0	0	TDC Link Present flags (=0x00080)																			
BOT	1	0	1	TDC 2					ECNT												BCID											
TD	0	0	1	1	0	0	JT		Channel 6					T	E	Coarse												Fine				
BOT	1	0	1	TDC 7					ECNT												BCID											
TD	0	0	1	1	0	0	JT		Channel 14					T	E	Coarse												Fine				
EOT	1	1	0	0	0	0	JT		ECNT												TDC WCNT (=3)											
TWC	1	0	0	0	1	0	1	0	ECNT												Trailer Word Count (=7)											

EOB	1	1	1	1	0	0	0	0	0	0	0	0	0	0	0	0	MROD Block WCNT															

`MSE1`	MROD Status word																															

NSE	Number of Status Elements (= 0x00000001)																															
NDE	Number of Data Elements (= WCNT from EOB word)																															
SBP	Status Block Position (= 0x00000001: status at end)																															

Bibliography

[1] M. Guidry, Gauge field theories: an introduction with applications, Wiley & Sons (1991).

[2] M. Spira, P. M. Zerwas, Electroweak Symmetry Breaking and Higgs Physics, hep-ph/9803257.

[3] B. W. Lee et al., Phy. Rev. Lett. 38 (1977) 833

[4] ALEPH, DELPHI, L3 and OPAL Collaboration, The Search for the Standard Model Higgs Boson at LEP, CERN-EP/2003-011 (2003)

[5] ALEPH, DELPHI, L3 and OPAL Collaboration, the LEP Electroweak Working Group and the SLD Heavy Flavour Working Group, A combination of Preliminary Electroweak Measurements and Constraints on the Standard Model, CERN-EP/2002-091 (2002)

[6] ATLAS Collaboration, ATLAS Detector And Physics Performance Technical Design Report, CERN/LHCC/99-15, ATLAS TDR 15, 1999.

[7] *PYTHIA 6.2, Physics and manual*, hep–ph/0108264, LUTP–2001–21, 2001.

[8] F. Gianotti, Collider Physics: LHC, ATL-CONF-2000-001

[9] S. Asai et al., Prospects for the Search for a Standard Model Higgs Boson in ATLAS using Vector Boson Fusion

[10] http://lhc.web.cern.ch/lhc/, Home Page

[11] ATLAS Collaboration, ATLAS Technical Proposal for a General Purpose p-p Experiment at the Large Hadron Collider at CERN, CERN/LHCC/94-43, 15-12-1994

[12] ATLAS Collaboration, Atlas Detector and Physics Performance, 25-05-1999

[13] ATLAS Collaboration, Inner Detector Technical Design Report, CERN/LHCC/96-16, 1997

[14] R. Wigmans, Advances in Hadron Calorimetry, Cern-PPE/91-39, 25-02-1991

[15] R. Wigmans, High Resolution Hadron Calorimetry, Ferbel, Singapore, World Scientific, 1991

[16] ATLAS Collaboration, Liquid Argon Calorimeter Technical Design Report, CERN/LHCC/96-41, 1996

[17] ATLAS Collaboration, ATLAS Muon Spectrometer Technical Design Report, CERN/LHCC/97-22, 05-06-1997

[18] H. Kroha et al., Quality Assurance and Control Reference Document for ATLAS MDT Chamber Construction, MDT Production Readiness Review, 16-17/6/1999

[19] C. Bacci et al., Autocalibration of high precision drift tubes, ATL-MUON-97-135 (1997).

[20] J. Chapman et al., Data flow simulations through the ATLAS Muon front-end electronics, Proceedings of the 5th Conference on Electronics for LHC Experiments, Snowmass, CO, 20-24 September 1999, p.448.

[21] J.E.Huth, J.Oliver, E.S.Hazen, C.Posch, J.T.Shank, Development of an octal CMOS ASD for the ATLAS Muon detector, Proceedings of the 5th Conference on Electronics for LHC Experiments, Snowmass, CO, 20-24 September 1999, p.436;
C.Posch, E.Hazen, and J.Oliver, MDT-ASD: CMOS front-end for ATLAS MDT chambers, ATL-MUON-2002-003
`http://weblib.cern.ch/Home/ATLAS_Collection/ATLAS_Notes/Muon/`

[22] Y.Arai, Nucl. Instr. and Meth. in Phys. Res. A453 (2000) 365;
Y.Arai, Y.Kurumisawa and T.Emura, Development and a SEU Test of a TDC LSI for the ATLAS Muon Detector, Proceedings of the 7th Workshop on Electronics for LHC Experiments, Stockholm, Sweden, 10-14 September 2001, p.185.

[23] ATLAS Collaboration, Trigger, DAQ and Computing Technical Design Report

[24] ATLAS Collaboration, Trigger Performance Requirements and constraints, 25-08-1998

[25] S. Baranov et al., Estimation of Radiation Background, Impact on Detectors, Activation and Shielding Optimization in ATLAS, CERN-ATL-GEN-2005-001 (2005).

[26] G. Darbo et al., Outline of R&D activities for ATLAS at an upgraded LHC, CERN-ATL-COM-GEN-2005-002, 2005

[27] G. Avolio et al., Monitored Drift Tubes aging under intensive gamma irradiation, Nuclear Instruments and Methods in Physics Research A568, pp. 624-633, 2006

[28] P. Branchini et al., Neutron irradiation test on ATLAS MDT chambers, Nuclear Instruments and Methods in Physics Research A574, pp. 57-64, 2007

[29] E. Meoni et al., Gamma and neutron massive irradiation tests of the ATLAS MDT chambers, Nuclear Instruments and Methods in Physics Research A572, pp. 187-188, 2007

[30] D. Salvatore et al., Neutron irradiation test on ATLAS MDT chambers, Nuclear Physics B (Proceedings Supplements), 72C, pp. 183-186, 2007

[31] F. Petrucci et al., Intensive irradiation study on Monitored Drift Tubes chambers, IEEE Transactions on Nuclear Science, Vol. 54,Â Issue 3, pp. 648-653, 2007

[32] A. Aprile et al., Production and test of monitored drift tubes for the muon spectrometer of the ATLAS experiment, IEEE Transaction on Nuclear Science, 49-3 (2002) 1077

[33] S.Baccaro et al., Gamma and neutron irradiation facility at ENEA-Casaccia Center, Report CERN-CMS/TN, 95-192 (RADH) 1995.
A.Tata et al., Radiation technology facilities operating at the Italian ENEA-Casaccia research center, ENEA RT/INN/98/1, CERN libraries, Geneva SCAN-9809001.

[34] G.Scherberger et al, High rate performance of drift tubes, Nucl. Instr. and Meth. in Phys. Research A 424 (1999) 495-511.

[35] P.Bagnaia et al., `CALIB`: a Package for MDT Calibration Studies, ATL-COM-MUON-2002-004, 28.1.2002,
`http://weblib.cern.ch/Home/ATLAS_Collection/ATLAS_Notes/Muon/`

[36] A.Baroncelli et al., Nucl. Instr. and Meth. in Phys. Res. A557 (2006) 421-435

[37] A.Policicchio, Study of rare beauty decays with ATLAS detector at LHC and MDT chamber performances, CERN-THESIS-2006-073

[38] A.Aleksa, W.Riegler, Non-linear MDT drift gases like Ar-CO_2, ATL-MUON-98-268, 14.12.1998,
`http://weblib.cern.ch/Home/ATLAS_Collection/ATLAS_Notes/Muon/`.

[39] S. Baccaro et al., Gamma and neutron irradiation facility at ENEA-Casaccia Center, Report CERN-CMS/TN, 95-192 (RADH) 1995.
A. Tata et al., Radiation technology facilities operating at the Italian ENEA-Casaccia research center, ENEA RT/INN/98/1, CERN libraries, Geneva SCAN-9809001.

[40] K.W. Burn et al., Characterisation of the Tapiro BNCT epithermal facility, Radiation Protection Dosimetry (2004), Vol. 110, Nos 1-4, 645-649

[41] F. Lacava et al., Non invasive technique to replace anode wire into the MDT chambers of the ATLAS muon spectrometer,ATL-COM-MUON-2005-021, 2005

[42] S. Kirche et al., Parameter of MDT Ageing and Reanimation, ATL-MUON-2001-012,
`http://weblib.cern.ch/Home/ATLAS_Collection/ATLAS_Notes/Muon/`.

[43] S. Zimmerman et al., MDT ageing studies - Results of the studies conducted at the Gamma Irradiation Facility GIF between autumn 2001 and summer 2003, ATL-MUON-2004-019,
`http://weblib.cern.ch/Home/ATLAS_Collection/ATLAS_Notes/Muon/`.

[44] C. Adorisio et al., Results from the 2004 ATLAS MDT ageing test in X5/GIF (Gamma Irradiation Facility) area, ATL-COM-MUON-2005-016,
http://weblib.cern.ch/Home/ATLAS_Collection/ATLAS_Notes/Muon/.

[45] C.Posch, E.Hazen, Total ionizing dose radiation hardness of the ATLAS MDT ASD and the HP-Agilent 0.5 micron CMOS process, ATL-ELEC-2002-001,
http://weblib.cern.ch/Home/ATLAS_Collection/ATLAS_Notes/Muon/.

[46] Y.Arai, M.Fukuda, T.Emura, Performance and irradiation tests of the 0.3 μm CMOS TDC for the ATLAS MDT, CERN-OPEN-2000-102,
http://weblib.cern.ch/Home/ATLAS_Collection/ATLAS_Notes/Muon/.

[47] P. Adragna et al., GNAM: A Low-Level Monitoring Program for the ATLAS Experiment, IEEE Transaction on Nuclear Science, vol.53-3, 1317-1322
P. Adragna et al., GNAM and OHP : Monitoring Tools for ATLAS experiment at LHC, ATL-COM-DAQ-2007-013 (2007)
D. Salvatore et al., The GNAM system in the ATLAS online monitoring framework, Nuclear Physics B (Proceedings Supplements), Vol. 172, pp. 317-320 (2007)

[48] https://twiki.cern.ch/twiki/bin/view/Atlas/AthenaMonFramework

[49] A. Dotti et al., OHP: An Online Histogram Presenter for the ATLAS experiment, ATL-DAQ-CONF-2006-006 (2006)

[50] C. Bee et al., The raw event format in the ATLAS Trigger & DAQ, ATL-DAQ-98-129

[51] P. Fleischmann and D. Salvatore, Description of the Tube Mapping for the ATLAS Barrel MDT Chambers, ATL-COM-MUON-2005-023 (2005)

[52] T.A.M. Wijnen, The MROD data format and the tower partitioning of the MDT chambers, ATL-DAQ-2003-023

[53] R. Brun, F. Rademakers (1997), *ROOT An Object Oriented Data Analysis Framework*, Nucl. Instr. & Meth. in Phys. Res. A 389, pp. 81-86.

[54] T. Bold et al., Histograms Naming Convention, ATL-DQ-ON-0015 (2006)
https://edms.cern.ch/document/710911/1

[55] M. Virchaux et al., The PERSINT manual, ATL-SOFT-2001-003 (2001)
`http://cdsweb.cern.ch/record/684168`

[56] M. Hauschild et al., Data Quality Monitoring Architectural Design, ATL-DQ-ON-0024, 2006
`https://twiki.cern.ch/twiki/bin/view/Atlas/DataQuality`

[57] R. Veenhof, GARFIELD: a drift chamber simulation program, CERN program library W5050

[58] `http://atlas-magnet.web.cern.ch/atlas-magnet/`

[59] M. Cirilli et al., Results from the 2003 beam test of a MDT BIL chamber: systematic uncertainties on the TDC spectrum parameters and on the space-time relation, CERN-ATL-COM-MUON-2004-009 (2004)

Grazie a...

... al “Grande Capo” Prof. Giancarlo Susinno (INFN Cosenza), per la stima e la fiducia incondizionata dimostratami in questi anni di dottorato, per avermi dato la possibilità di muovermi autonomamente fra le attività dell’esperimento e per aver sempre approvato le mie scelte.

... alla Dott.ssa Gabriella Gaudio (INFN Pavia), squisita compagna d’“avventure di programmazione” nel bene e nel male :-) Grazie per la disponibilità e l’amicizia dimostratemi dall’inizio della nostra collaborazione fino alla stesura di questa tesi. Sono in debitissimo con te!

... alla Dott.ssa Manuela Cirilli (University of Michigan), che dalla tesi di laurea mi segue e mi consiglia con grande affetto. Grazie per aver sempre trovato del tempo per me, anche quando tutte e 25 le ore della tua giornata erano piene. Spero di poterti restituire altrettanto.

... ai miei, che pensano faccia un lavoro “extra-ordinario” (soprattutto papà)

... a Fanny, Leuccio e Liù, per essersi sempre comodamente accucciati su libri, appunti e quant’altro :-)

... ad Andrea, Raffaella e al “Ciotone”, per le innumerevoli “sportellate” (♥, ♦, ♣, ♠).

...e soprattutto a Mario, per aver sopportato con infinita pazienza e amore, nei nostri 7 anni insieme, tutti i miei “ora non posso”!